PREDIS

Deliverable 7.5
Report on the Digital Twin of a cemented wase package, geochemical evolution and mechanical integrity modelling

27.02.2024 Version 1.2 Final

Dissemination level: Public

George Dan Miron

Paul Scherrer Institut, Laboratory for Waste Management
Forschungsstrasse 111
5232 Villigen PSI
Switzerland

dan.miron@psi.ch

This project has received funding from the Euratom research and training programme 2019-2020 under grant agreement No 945098.

Project acronym PREDIS	Project title PRE-DISposal management of radioactive waste		Grant agreement No. 945098
Deliverable No. D7.5	Deliverable title Digital Twin of a cemented wase package, geochemical evolution and mechanical integrity modelling		Version 1.2
Type Report	Dissemination level Public		Due date M42
Lead beneficiary PSI			WP No. 7.4
Main author George-Dan Miron (PSI)	Reviewed by Ernst Niederleithinger (BAM), WP7 Lead	Accepted by Maria Oksa (VTT), Coordinator	
Contributing author(s) Seetharam Suresh (SCK CEN), Phung Quoc Tri (SCK CEN), Eric Laloy (SCK CEN), Gert Dekkers (MAGICS), Jafari Abbas (BAM), Unger, Jörg F. (BAM), Andrés Idiart (Amphos21), Meeussen, J.C.L. (NRG), Hu Guang (PSI), Pfingsten Wilfried (PSI), Dähn Rainer (PSI)			Pages 66

Abstract

The concept of Digital Twins (DT) has gained prominence over the past two decades, revolutionizing decision-making processes across diverse industries. The development is driven by data models, physics-based simulations, or hybrid approaches, and enhance decision-making processes. Building a digital twin involves challenges like long-term process monitoring, scaling models from lab to waste package, parameterizing models, quantifying uncertainties, and integrating feedback between complex processes. This report presents the efforts of WP 7.4 consortium towards developing a proof of concept of certain aspects of digital twin technology for the predisposal management of radioactive waste, especially for low and intermediate level waste packages.

Firstly, the report addresses the development of a prototype "digital twin" toolkit that can accommodate different physical and chemical models representing the mechanisms affecting waste packages. With this, the user should be able to compute the chemical and physical behavior of cemented waste packages during interim storage for given waste package properties (input) to retrieve parameters (output) relevant for its integrity evolution as a function of time. Implementation of two key processes viz., modeled with GEMS and ORCHESTRA, cement hydration and carbonation of cemented waste packages have been successfully demonstrated via a DT dashboard. In particular, the idea of *waste integrity parameter* as a measure has been proposed, which can be extended to other processes.

The prediction of waste package evolution is complex as it involves different processes that happen on different temporal and spatial scales. Therefore, recourse to meta models become inevitable from DT perspective. The use of neural network-based machine learning surrogate models is demonstrated, which shows a significant gain in computational efficiency when carrying out sensitivity analysis on the rate of waste material degradation.

Central to the DT framework is the development or implementation of appropriate (multi)physics-based models. However, the physics-based models are typically phenomenological models and may involve many primary variables such as temperature, pressure, displacements etc. to capture the relevant thermo-hydro-chemo-mechanical processes of the waste package. This leads to a significant number of material parameters that have to be estimated based on laboratory or *in situ* experiments. This report describes Bayesian inference methods as a way forward for handling not only parameter estimation problems but also as a basis for the development of future metamodels.

Whilst the above efforts addressed various components of a DT framework, a key contribution of task 7.4 is in the implementation of a real-life case study of alkali silica reaction (ASR) pathology

at the drum scale. Such a pathology is a possibility if the right combination of alkali content, reactive silica and water occurs in the waste packages. A comprehensive experimental-numerical programme is presented that covers laboratory experiments such as isothermal calorimetric tests, autogenous shrinkage tests, ASR expansion tests, mechanical tests, and finally culminating in drum scale tests under natural and accelerated conditions. As part of DT, two approaches are taken: (i) a thermo-hydro-mechanical model to simulate ASR process is implemented based on existing knowledge, and (ii) two existing geochemical models, viz., ORCHESTRA and PHREEQC are applied based on the current conceptual understanding of the complex ASR process. While the objective of the first approach is to be able to predict strain evolution at the drum scale, the objective of the second approach is to be able to perform screening analysis to identify if ASR product is formed given the cement recipe.

Implementation of digital twin is by no means trivial and fraught with many challenges. The experience of the consortium partners in this respect is also captured in this report, with a view to preparing for future research in DT technologies.

This report is a result of the collaboration between SCK CEN, Magics, BAM, Amphos 21, NRG, and PSI.

Keywords

digital twin; digital toolkit; waste package degradation; chemical evolution; surrogate models; machine learning; alkali silica reaction; Bayesian method

Coordinator contact
Maria Oksa
VTT Technical Research Centre of Finland Ltd
Kivimiehentie 3, Espoo / P.O. Box 1000, 02044 VTT, Finland
E-mail: maria.oksa.@vtt.fi
Tel: +358 50 5365 844

Acknowledgement
This project has received funding from the Euratom research and training programme 2019-2020 under grant agreement No 945098.

HISTORY OF CHANGES

Date	Version	Author	Comments
12.02.2024	1.0	SCK CEN, Magics, BAM, NRG, Amphos21, PSI	Draft for internal review
19.02.2024	1.1	BAM	Review by WP lead
27.02.2024	1.2	SCK CEN, Magics, BAM, NRG, Amphos21, PSI	Final version

TABLE OF CONTENTS

1 DEFINITION DIGITAL TWIN AND INTRODUCTION 8
1.1 Overview 8
1.2 Pipelines 9
2 DIGITAL TWIN TOOLKIT 10
2.1 Dashboard 10
3 MODELS 15
3.1 Macroscale 15
3.2 Cement chemistry, geochemical models 15
4 METAMODELS 16
4.1 Neural Networks 16
5 MODEL PARAMETER UPDATING 25
5.1 Theoretical background 25
5.2 MCMC simulation of the posterior parameter pdf 26
5.3 Variational Bayesian inference 27
6 USE CASE ON ASR 28
6.1 Introduction 28
6.2 Methodology 28
6.3 Mixture design 29
6.4 Data pipeline 29
6.5 Experimental setup 30
6.5.1 Laboratory scale 30
6.5.2 Drum scale 31
6.6 Results 33
6.6.1 Laboratory scale 33
6.6.2 Drum scale 34
6.7 Thermo- hydro-mechanical model for ASR 36
6.7.1 Domain, initial and boundary conditions 44
6.7.2 Parameter estimation 45
6.7.3 Summary of material parameters 51

6.7.4 Modelling results 53
6.8 Geochemical model for ASR 56
7 SUMMARY AND CHALLENGES 62
7.1 Contributions 62
7.2 Challenges 63

1 Definition Digital twin and introduction

1.1 Overview

The concept of Digital twins (DT) emerged around two decades ago and since then has become a top trend in various industries. The building and maintenance of increasingly complex systems in the real world requires digital counterparts for decision making with the ability to track all information related to a physical asset over the complete lifecycle. The general interpretation of what exactly a DT is varies between different consortia and areas of applications and thus using the term usually requires a more detailed description.

In general, a DT represents a product (or structure) over the complete four phases of the lifecycle (Create, Build, Operate, Dispose) but products are often integrated into other systems resulting in a hierarchy of DTs e.g., radioactive waste is disposed and thus in the final phase, but requires facilities to handle that which are still in the first phases of their lifecycle. A digital twin requires a dual representation in the real world, though it is not mandatory that they coexist at the same time. In particular, an intelligent digital twin can provide information about the real assets from the past, identify the current state and even predict future performance. These predictions can be based either on pure data models (AI), physics-based simulation models or combinations thereof. This includes setups where data is used to update the models or where data is used to compensate for model deficiencies (the inability of the model to represent reality). Although a digital twin requires a repository that allows access to all the information from the real asset (design drawings, reports, sensor (meta) data), its intelligence stems from the ability to provide information that is not directly measurable. This intelligence is realized by jointly analyzing and augmenting the information from the real asset with additional functionality. This includes the ability to install virtual sensors in simulation models to predict quantities of interest that are not measured (e.g. at positions that are not accessible or quantities that are difficult to measure at all), plan maintenance and support decision making with the ability to investigate case studies and quantify the impact of potential decisions on the future performance or identify in real-time critical scenarios with an automated process control and a feedback to the real system to mitigate the severity – potentially even without the need of human interaction or as a tool to compress the complex data stream from the real asset to support the decision making by a human.

The principal objective of PREDIS task 7.4 is to develop a proof of concept of certain aspects of digital twin technology for the predisposal management of radioactive waste, especially for low and intermediate level waste packages. Thus, Chapter 2 presents the development of a prototype "digital twin" toolkit that can accommodate different physical and chemical models representing the mechanisms affecting waste packages. The user should be able to compute the chemical and physical behavior of cemented waste packages during interim storage for given waste package properties (input) to retrieve parameters (output) relevant for its integrity evolution as a function of time. Central to the DT framework is the development or implementation of appropriate (multi)physics-based models. A broad overview of some modelling aspects is presented in Chapter 3 as a more detailed state of the art in modelling is addressed in deliverable 7.1 *State of the Art in packaging, storage, and monitoring of cemented wastes [1]*. Chapter 4 presents the outcomes of a study on the development of metamodels, in particular, neural network based surrogate models to circumvent high computational demand imposed by geochemical models such as GEM-SELEKTOR for complex geochemical systems. The physics-based models are typically phenomenological models and may involve many primary variables such as temperature, pressure, displacements etc. to capture the relevant thermo-hydro-chemo-mechanical processes of the waste package. This leads to a significant number of material parameters that have to be estimated based on laboratory or *in situ* experiments. Thus, Chapter 5 describes Bayesian inference methods that are deemed suitable for the present application. Chapter 6 presents by far the most comprehensive study of some of the components of DT using a case study of alkali silica reaction (ASR) pathology that may occur in waste packages. This chapter covers deployment of laboratory experiments, drum scale experiments, associated sensor architecture, theoretical models for thermo-hydro-mechanical behavior as well geochemical behavior for ASR, parameter estimation and numerical analysis.

Implementation of digital twin is by no means trivial and fraught with challenges. Thus Chapter 7 aims to cover major issues faced by the consortium partners in this respect.

1.2 Pipelines

The Digital Twin comprises both the data (for past, current or even the future conditions - e.g. the expected loads or environmental conditions) and at the same time the models to analyze that data. A challenge when integrating Digital Twins is the complex interaction of different experts, subsystems, software tools, or sensors in a joint platform (e.g., chapter 6.4). To handle these challenges appropriately, automated pipelines with well-defined interfaces between the different subsystems must be developed such that individual subsystems can be developed while relying on the functionality of the complete Digital Twin. This includes the structuring and uploading of (meta)data to the database with agreed standardized formats (e.g. using schemas, ontologies, etc.), interfaces to query and visualize the data (both with an interactive GUI for humans as well as an interface for machines) and the automated (based on user-defined triggers) processing of the data. This processing of data can have multiple layers of complexity potentially being executed subsequently in a pipeline defined by a direct acyclic graph. This can range from filtering of the data and feature extraction for ML models over simple regression models up to machine learning models or complex physics models with computer intensive model evaluations (e.g. using FEM). In particular in the context of Digital twins, it is very common that these models are hierarchical. For example, there is a model updating module that takes as input the filtered data and a model and provides an update of the parameters, which are then used to make predictions of the future performance.

With an increasing complexity of the data processing in each sub-module of the data processing pipeline, there is a need to standardize these modules such that the execution is reproducible, i.e. the interfaces of the module (input and output) as well as the compute environment (e.g. using containers or conda). In order to test these pipelines, it is often advantageous to set up a continuous integration workflow with a set of representative minimal number of working examples that allow to identify inconsistencies in the Digital Twin.

2 Digital Twin toolkit

As the evolution of waste packages is most likely governed by a combination of chemical and physical-mechanical processes, it follows that the Digital Twin has to contain a combination of chemical interaction and chemo-mechanical process models. There are different ways to approach this and technical methods to implement and integrate. One approach would be to model a complete single waste package using a detailed reactive transport model discretized at mm scale, that is combined with a mechanical module to describe physical behaviour based on local chemical conditions. The drawbacks of this approach would be that not only calculations would take a very long time, but also that a large set of input data would be required that is currently not available in practice for any waste package. The other end of the scale of complexity would be to treat the complete waste package as a homogeneous well-mixed cell, in which the main degradation processes are represented with a set of processes that are generally responsible for most changes related to the evolution of mineralogical and mechanical properties (Figure 2-1). The advantage of this approach would be that calculations are much faster and that much fewer input data would be required. A problem would be that this method would probably not be able to capture the main driving mechanisms for chemical evolution in heterogeneous systems as these are determined by local chemical conditions.

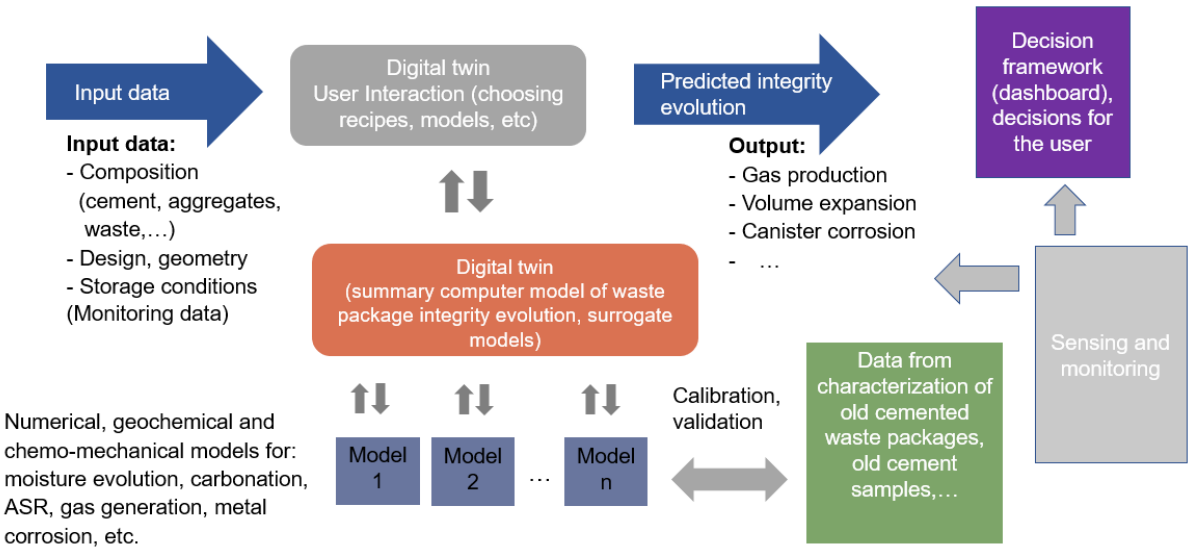

Figure 2-1 A schematic overview of the processes in a digital twin

2.1 Dashboard

In the context of the PREDIS project a dashboard was developed as a proof of concept where users can interact with different models related to waste package degradation. Such a dashboard can contain different physical and chemical models representing the mechanisms affecting waste packages. This serves as a way for the user to interact with the models and to produce data for different scenarios that could be then used in a decision framework on the suitability of the waste package.

The models can be run for different given waste package properties (input) to retrieve parameters (output) relevant for waste package integrity evolution as a function of time (Figure 2-2). This allows us to produce datasets of waste package evolution scenarios, which combined with experimental observations can be used to train surrogate models. Such models can be used to efficiently test

different compositions for potential problems of existing and future waste packages and do uncertainty propagation and sensitivity analysis.

The results of one process could be used as input for another and all output results can finally be used to train surrogate models. This is similar to choosing models for the most significant processes that control waste degradation and build a metamodel (see chapter 4). Based on the input values (dimension, physical properties and chemical composition of the materials) and the appropriate evolution submodel(s) parameters that indicate integrity evolution of the waste package as a function of time (e.g. pressure and or volume changes) may be defined and calculated.

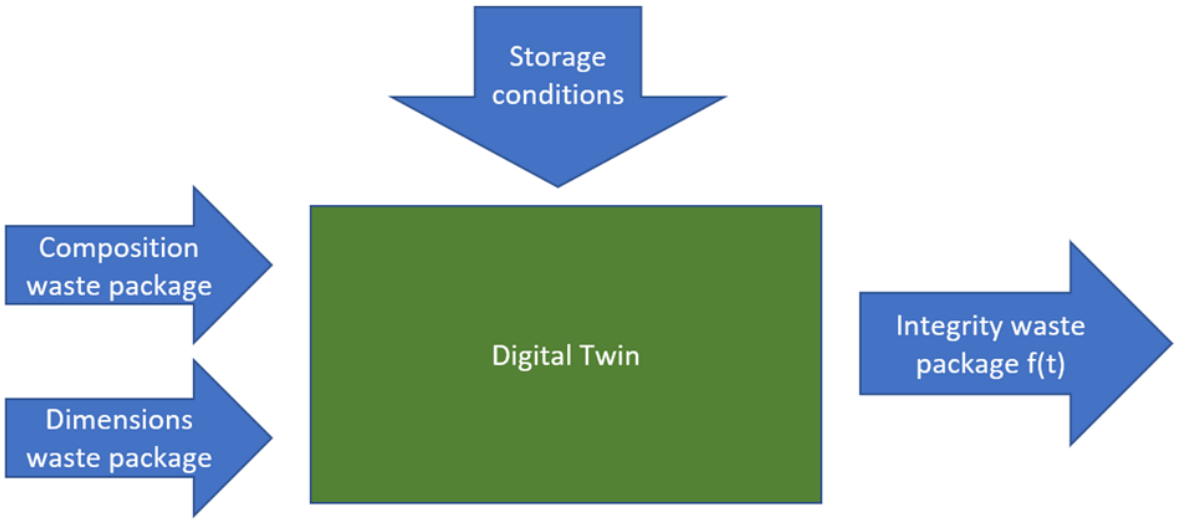

Figure 2-2 Digital Twin concept used to develop the dashboard prototype

A demo prototype of the Digital Twin dashboard is running on the geoml platform (https://digitaltwin.geoml.eu/). Two examples have been implemented demonstrating the potential of having a platform where users can interact with models related to cementitious waste package evolution. These models have been implemented using different geochemical modelling codes and show the potential of having several tools running on the same platform that can be used to model different aspects.

The prototype dashboard was implemented in the Jupyter notebook environment using the python code. This is a web-based, collaborative interactive development environment that works in the browser. One can easily create simple demonstrative web apps that can be shared between developers and users with no or minimum requirements for installing dependencies and can take advantage of the different python libraries for adding data processing, statistical analysis, visualization, and machine learning functionalities.

The actual code that runs the model is in the form of python scripts that collects the input parameters and that calls the respective geochemical modelling code or mathematical formulations to model the respective process (e.g., cement hydration, carbonation).

As a first example, the user can select and run a “Cement Hydration” process and test the volume evolution of a waste package cement recipe during hydration based on the cement recipe (Figure 2-2).

(a)

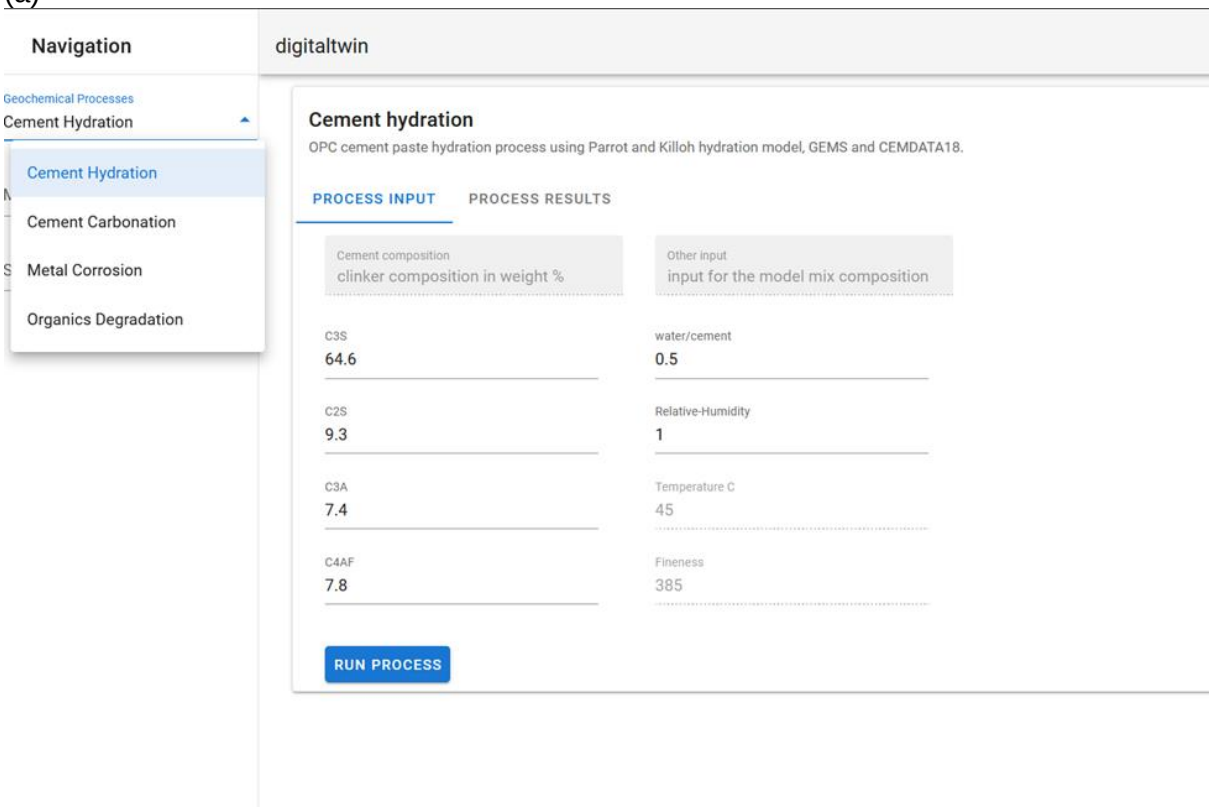

(b)

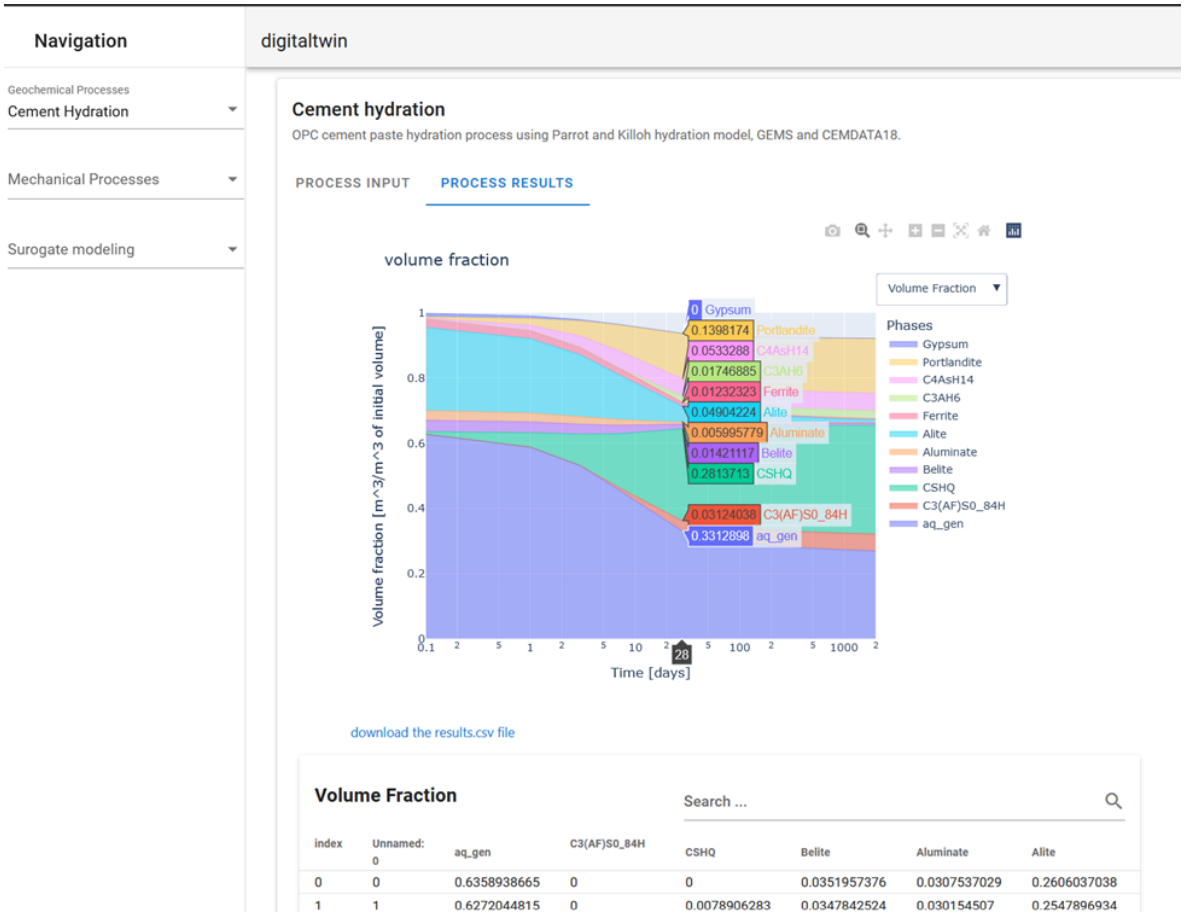

Figure 2-3 Cement hydration model in the dashboard prototype, (a) process input, (b) results.

The input parameters are the weight percent of clinker phases (defining the clinker composition), water to cement ratio and relative humidity, and the output data are the volumes or masses clinker and cement hydrate phases at different time of cement hydration. In the background a python script runs that implements a kinetic model for the hydration of the clinker phases, the so-called Parrot Killoh model [2] while the geochemical equilibrium calculation is done using the xgems python interface of GEMS code [3].

A second example is running a 2D cement carbonation scenario (Figure 2-4) and calculates the evolution as a function of time of a waste package integrity parameter. As input the user can change several chemical and physical parameters of the domain, such as the composition of the cement, the composition of incoming carbonate rich fluid, and porosity. The final integrity parameter calculated as: Integrity = 1 - (12-pH)/7 is an example of how a certain property of the system can be used to assess its integrity. In this case the integrity is given by the fraction of material having pH values between 5 and 12, with integrity 1 when all material has pH 12 and 0 when the pH is 5 in all the domain signifying that all the cement was carbonated (pH of the carbonate rich solution). The actual calculations are done by calling Orchestra [4] code with the given input.

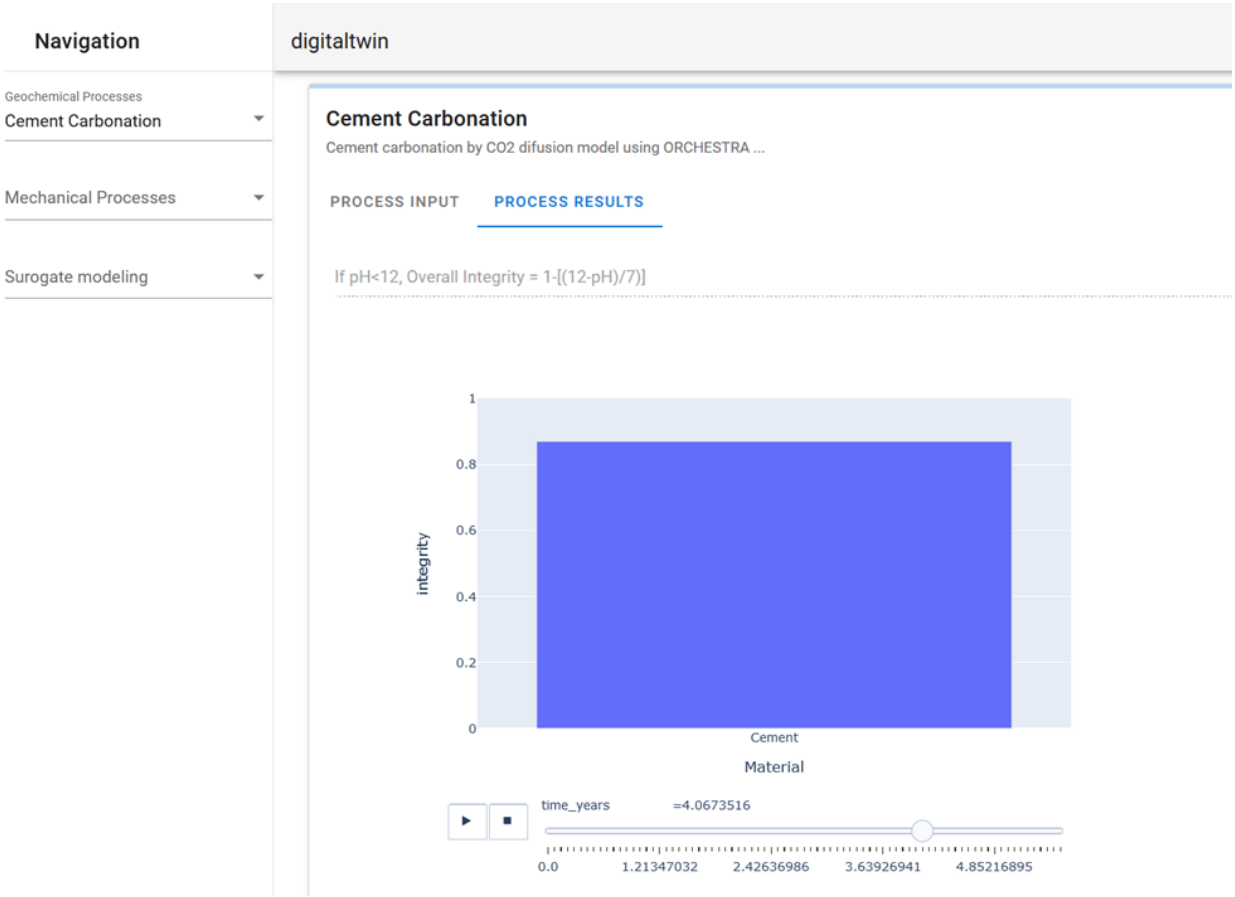

Figure 2-4 Cement carbonation dashboard example.

In a similar way to the above examples, other models of waste degradation can be implemented and exposed to the user for interaction in the dashboard. As the evolution of waste packages is most likely governed by a combination of chemical and physical-mechanical processes, it is logical that the Digital Twin has to contain a combination of chemical interaction and chemo-mechanical process models. Examples of chemical processes are cement hydration, carbonation, moisture evolution, alkali silica reactions (ASR), sulphate attack, gas generation, metal corrosion, etc.

Based on available data on waste packages (composition and properties) a set of reference waste types, predefined compositions, and materials can be made available for the users to create their desired waste package “recipe” (matrix, waste type, material amount and volume) and run the available evolution models for a given time interval. This will allow to test different compositions for potential problems of upcoming/future waste packages (e.g., suitable aggregates, new phosphate rich cements). But also, to test different “what if scenarios” on legacy waste packages for which limited data is available. For example, to replace missing waste package data with predefined data provided in the Digital Twin, combine it with the available information and see if there could be any waste package “recipe” that would result in exceeded waste acceptance parameters (e.g., use of different aggregates that could promote chemical reactions leading to a large volume change).

By running the models on different input parameters (based on waste packages composition data) a dataset of waste package evolution scenarios can be generated. These datasets could be used to train surrogate models such as artificial neural networks for fast and efficient prediction of the evolution of future wastes without the need to run the full, time consuming, degradation models. In addition, having the possibility to efficiently run degradation models thousands of times allows for the use of different statistical models such as Monte-Carlo (MC) based uncertainty propagation (UP), and Global Sensitivity Analysis (GSA) [5]. These methods provide information on the probability that output properties exceed a threshold based on sampling the input parameter distribution (MC-UP) and rank input parameters based on their influence on the model output (GSA).

3 Models

3.1 Macroscale

The choice of the macroscale model depends on the type of degradation mechanisms to be addressed. In particular, for the cemented waste forms based on ordinary Portland cement, one should expect processes such as delayed ettringite formation, alkali silica reaction (ASR), and gas pressure originating from corrosion of metals. These may result in an unstable waste form, which can be due to cracking, volumetric expansion, and/or production of unstable products. From the perspective of a Digital Twin, it is always recommended to work with simplified models requiring minimal material parameters, while capturing main features of the degradation mechanism. However, often coupled models are also necessary to correctly capture the degradation behavior. For example, degradation processes such as ASR depend on temperature and moisture fields coupled with mechanics warranting use of coupled models. A common choice of coupled models is described in SOTA [1].

3.2 Cement chemistry, geochemical models

One way to predict the chemical evolution of cemented waste packages is to use a thermodynamic modelling approach. Thermodynamic modelling applied to cement science has significantly increased confidence in the prediction of chemical processes during cement hydration and in durability-related problems. Geochemical simulators, such as GEMS, ORCHESTRA, or PHREEQC can be used together with cement-specific thermodynamic data to predict changes in chemical composition upon a perturbation. Reviews of advances in this field can be found elsewhere [6-9]. For instance, Lothenbach et al. [9] studied the influence of temperature on cement hydration using thermodynamic modelling, showing a very good agreement with experimental data of hydration experiments in terms of pore solution composition and solid phase assemblage. This approach aims to compose complex interaction models from existing literature data, in the form of thermodynamic databases containing sets of reactions and constants. Using total composition of a (e.g. cemented waste) system as input, such models can then predict the distribution of elements over different chemical forms in an equilibrium condition. An advantage of thermodynamic models is that building a model can make use of large datasets of existing information and does not need to be developed completely from scratch. Furthermore, the model allows blind predictions of systems for conditions for which no measurement data is (yet) available (e.g. over longer time scales).

When coupled with transport of solutes across the porous structure of cementitious materials, thermodynamic models are also used for the prediction of time-dependent phenomena such as calcium leaching, internal/external sulfate attack, or chloride ingress in concrete structures [10, 11]. However, such coupled reactive models may not include specific new interactions, or reaction kinetics. Note that even the thermodynamic models need to be evaluated for their predictive capabilities under new conditions. These thermodynamic models require a large set of input parameters, and also produce a large set of output parameters. This automatically implies that it is very difficult to “improve” such complex models by measuring empirically only a limited number of output parameters for a certain system with short term experiments. Geochemical modelling approaches are discussed in SOTA [1].

4 Metamodels

Metamodels and surrogates can be used to approximate complex systems where obtaining an analytical solution may be either difficult or impossible, to provide computational efficiency, and to act as interfaces between different temporal and spatial scales. Metamodels are built for simplifying the investigated system using formulations of models for the main processes that define its evolution (see chapter 6.7).

Surrogate models are a specific type of metamodel commonly associated with approximating complex simulations. Surrogate models are built for using interpolation and regression methods to represent the relationships within the data. The process of developing surrogate models involves data collection from experiments or simulations, model construction using different mathematical methods, and model optimization and validation. The model construction can be done using various techniques such as Bayesian approaches (see chapter 6.7.4.3), and machine learning algorithms such as neural networks (see chapter 4.1) that should capture the input-output relations.

4.1 Neural Networks

The prediction of waste package evolution is complex as it involves different processes that happen on different temporal and spatial scales. Modelling of such systems can become computationally expensive and the coupling between different processes difficult to implement. Machine learning methods such as neural networks (NN) can be used in such cases to address issues of coupling different processes and time-consuming calculations [12]. Neural networks can provide a statistical emulation method for the degradation process. These NN need to be trained using datasets generated by running the actual models using different input parameters in order to capture the relations between the input and output parameters.

The different materials conditioned in a cementitious matrix will be subject to different degradation processes and to the interaction with the main degradation products. With respect to the interim storage many of the geochemical processes happen on much larger time scales. For example, the degradation of organic matter (10^{-3}-10^{-5} mol/a), corrosion of metals (10^{-5}-10^{-8}mol/a for aluminum and steel), mineral dissolution/precipitation (10^{-14}-10^{-16} (mol/m^2 s), quartz dissolution; 10^{-7}-10^{-11} (mol/m^2 s), calcite precipitation), and ion diffusion in cement (10^{-12} m^2/s; gas diffusion 10^{-7} m^2/s) take several years to proceed in a significant amount [13]. The evolution of these degradation processes can be highly uncertain due to unknown reaction kinetic rates, complex surface characteristics, and material heterogeneities.

An example of using a NN surrogate model to assess the deterioration mechanisms of various materials like iron, aluminum, zinc, and brass, in cementitious waste packages is presented [14]. The degradation time of these materials while slow can be relevant to interim storage time scales of several tens of years. The NN is trained to predict the material degradation process by geochemical interactions within a cemented waste package over a span of up to 100 years. The sensitivity of the highly uncertain reaction rates (input parameters) of various materials is parametrized and used to assess their influence on the temporal evolution of gas amounts, masses of materials, ion concentrations and pH values (output parameters) which affect the bulk porosity and, consequently, on the integrity of waste containment. For this sensitivity analysis, 1 million cases are generated by the neural network-based surrogate model.

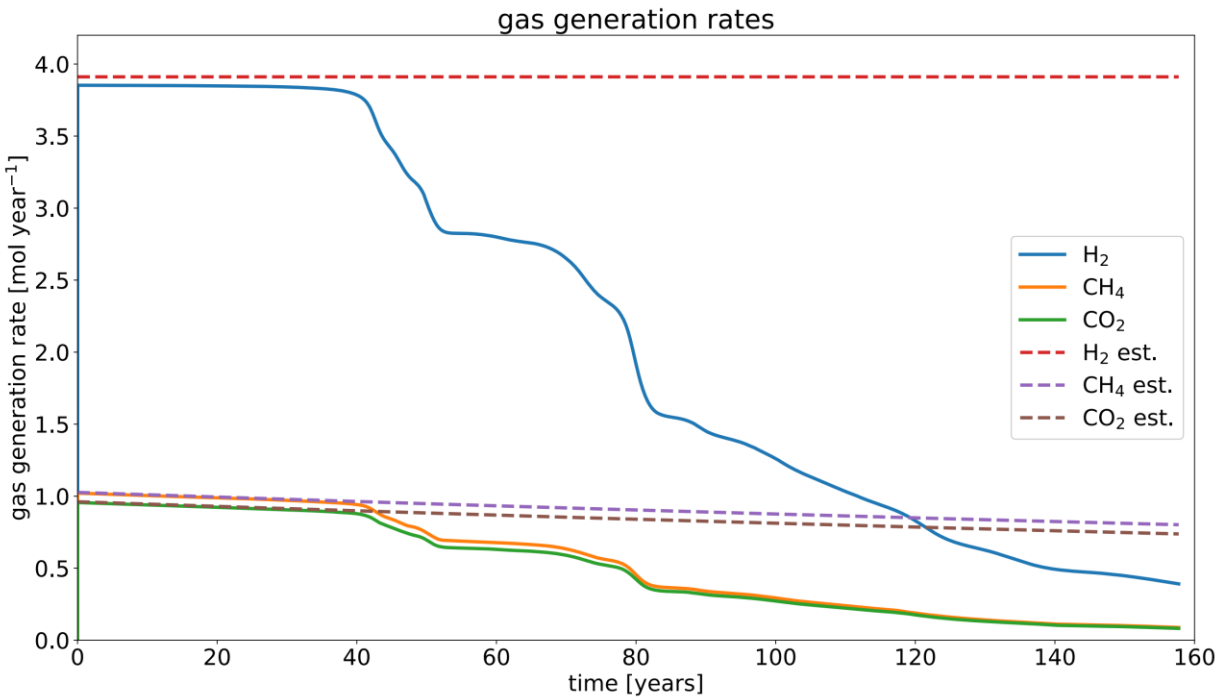

Figure 4-1 Gas generation in a cemented waste package from [15]. Solid lines modelled using a 2D reactive transport and dashed lines using the mixing tank approach [13, 16]

The degradation processes in a waste package are connected to the type of materials (their composition and physical properties) and their distribution. Evolution is influenced by complex chemical, transport and mechanical effects that would necessitate a very complicated modelling setup. In many cases some critical processes and effects can be qualitatively if not quantitatively studied by simplified models. A 2D reactive transport model [15] that coupled transport and chemical degradation kinetic processes via a look-up table approach was proposed. The reactive transport model did not include mechanical effects and showed similar gas generation rates up to 40 years when compared to the mixing tank modeling approach (Figure 4-1). Gas production was limited by water availability (dry out of the waste drum) at later evolution times.

A mixing tank model approach is used here for generating the training datasets, as a simplification of the unknown material heterogeneity in the cemented waste package [13]. The processes are modelled using geochemical calculations assuming complete mixing of the materials where all amounts of materials involved are available for reaction deepening on their reaction rate. This method allows to assess the relative contribution of different input parameters but does not account for detailed centimeter scale resolved evolution. Mechanic effects and transport processes are not considered although they might strongly influence the waste package evolution.

In the present example we focus on the organic materials degradation and metal corrosion rates. The organic degradation is assumed for readily degrading organic compounds (LWM), such as cellulose, and for PVC to follow the chemical reactions [13]:

LWM organics: $C_2H_4O_2 \rightarrow CO_{2(g)} + CH_{4(g)}$ (4-1)

PWC: $4\ C_2H_3Cl + 6\ H_2O \rightarrow CO_{2(g)} + CH_{4(g)} + HCl_{(aq)}$ (4-2)

The amount (m) of organics degraded as a function of time (t) is represented by:

$m(t)_{organics} = m(0)_{organics} * e^{-k*t}$ (4-3)

where, $m(0)_{organics}$ is initial inventory of organic matter (mol), k is the rate constant (a^{-1}).

The oxidation state of carbon is determined by the above reactions corresponding to the reduction capacity of organic matter [13] which fixes the ratio of CH_4 to CO_2 produced during decomposition. The produces gases are not allowed to further react. The metal corrosion processes are described by the following chemical reactions [13]:

Aluminium: $Al(s) + 3\ H_2O(l) \rightarrow Al(OH)_{3(s)} + 3/2\ H_{2(g)}$ (4-4)

Brass: $CuZn(s) + 4\ H2O(l) \rightarrow Zn(OH)_{2(s)} + Cu(OH)2(s) + 2\ H_{2(g)}$ (4-5)

Iron/steel: $3\ Fe(s) + 4\ H_2O(l) \rightarrow Fe_3O_{4(s)} + 4\ H_{2(g)}$ (4-6)

Zinc: $Zn(s) + 2\ H_2O(l) \rightarrow Zn(OH)_{2(s)} + H_{2(g)}$ (4-7)

The time dependent metal corrosion is represented by:

$m(t)_{Metal} = m(0)_{Metal} - k*t,$ (4-8)

rate constant $k = \frac{R*A*\rho}{M}$, (4-9)

where $m(0)_{Metal}$ is the initial inventory of metal (mol), R the Steady-state corrosion rate of metal ($m*a^{-1}$), A the Surface area of metal in the waste form (m^2), ρ the Density of metal ($kg*m^{-3}$), and M is the Molar mass of metal ($kg*mol^{-1}$)

The $H_{2(g)}$ that is produced during decomposition is considered inert during the evolution and is not allowed to further react with the other components. The chemical system was setup in GEM-Selektor geochemical code [3] and exported for the use in Python jupyter notebook scripts through the xGEMS C++/Python interface. Detailed description of the model setup and initial conditions are given in Wieland et al. (2020) [13]. Based on the initial composition of the cementitious material used for conditioning and the waste material, the geochemical evolution in the waste package was modeled as a function of time (up to 100 years) accounting for the effect of the degradation of organic waste materials and metal corrosion assuming unlimited water availability. Based on their reaction rate at different time steps a certain amount of these materials are allowed to react and are given to GEMS to the chemical composition of the system, stable phases (aqueous, gaseous, solids), their amounts and composition (Figure 4-2). Over the time span of 100 years the brass is predicted to corrode in the first 2.5 years, while the aluminum waste is completely corroded in about 50 years. The LWM are also predicted to degrade in about 100 years. This calculation was based on the reference rates provided in Wieland et al. [13] and does not account for possible change due to passivation or acceleration. In the sensitivity study it is assumed that the spread of rates can be of one order of magnitude lower or higher than the reference values.

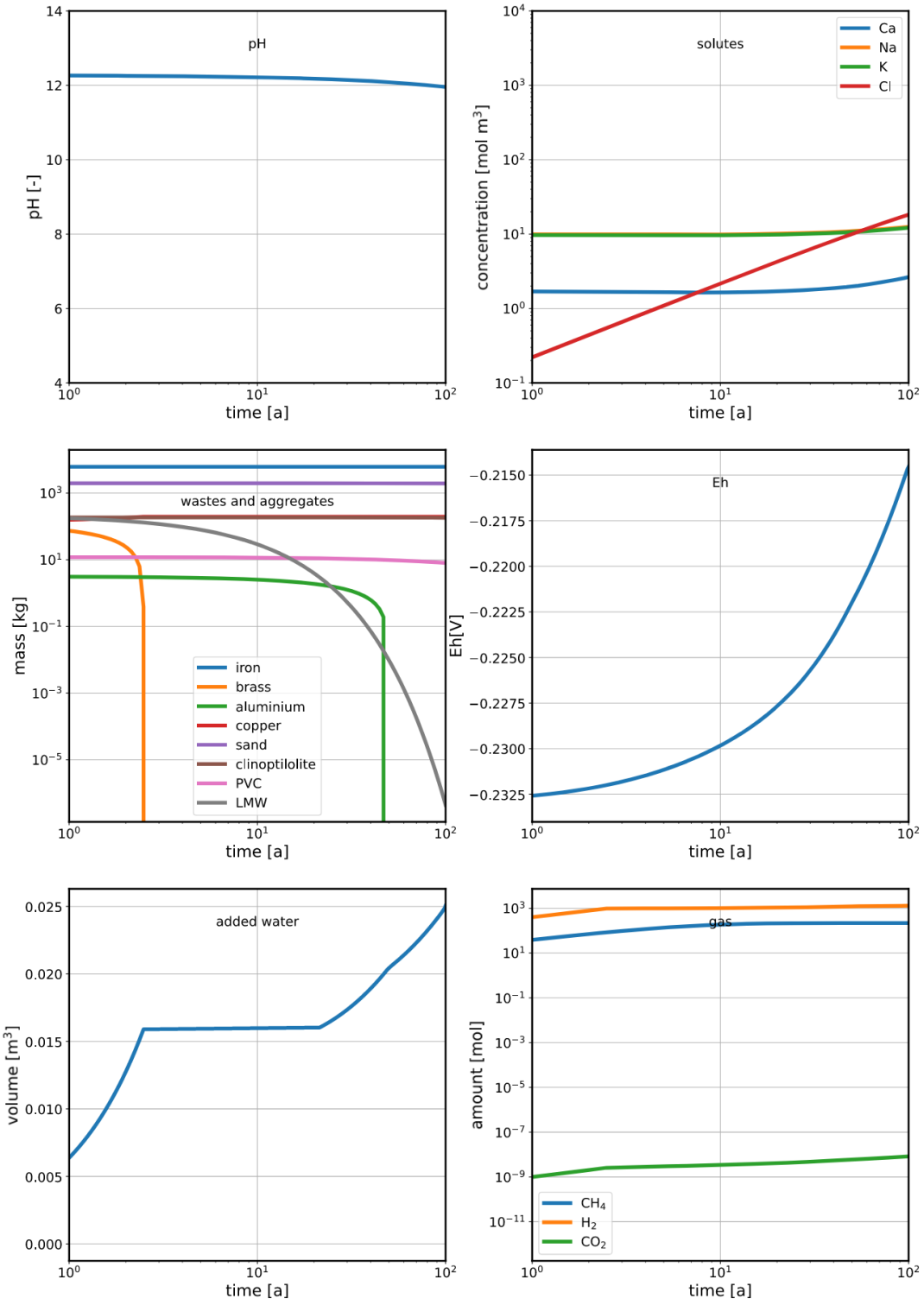

Figure 4-2 Chemical evolution of a cemented waste package over 100 years with modeled waste degradation processes (organics degradation and metal corrosion)

A NN surrogate model is trained on such different waste package evolution calculations for different reaction rates. Figure 4-3 depicts the neural network structure comprising an input layer, hidden layers, and an output layer. This structure features six inputs and fourteen outputs. The 6 inputs include time, organic degradation rate, and corrosion rates for Fe, Al, Zn, and brass ('time', 'organicaDegradation_rate', 'corrosionFe_rate', 'corrosionAl_rate', 'corrosionZn_rate', 'corrosionBrass_rate'). The 14 outputs are categorized into three groups: gas information (CO_2(g),

$H_2(g)$, $CH_4(g)$), mass of various materials (clinoptilolite (CLI(ca)_mass), sand (SiO2(cr)_mass), copper (Cu(cr)_mass), aluminum (Aluminium_mass), brass (brass_mass), iron (Fe(alpha)_mass)), aqueous phase concentrations (Cl (Cl_total_aq_phase), K (K_total_aq_phase), Na (Na_total_aq_phase), Ca (Ca_total_aq_phase)), along with the pH value.

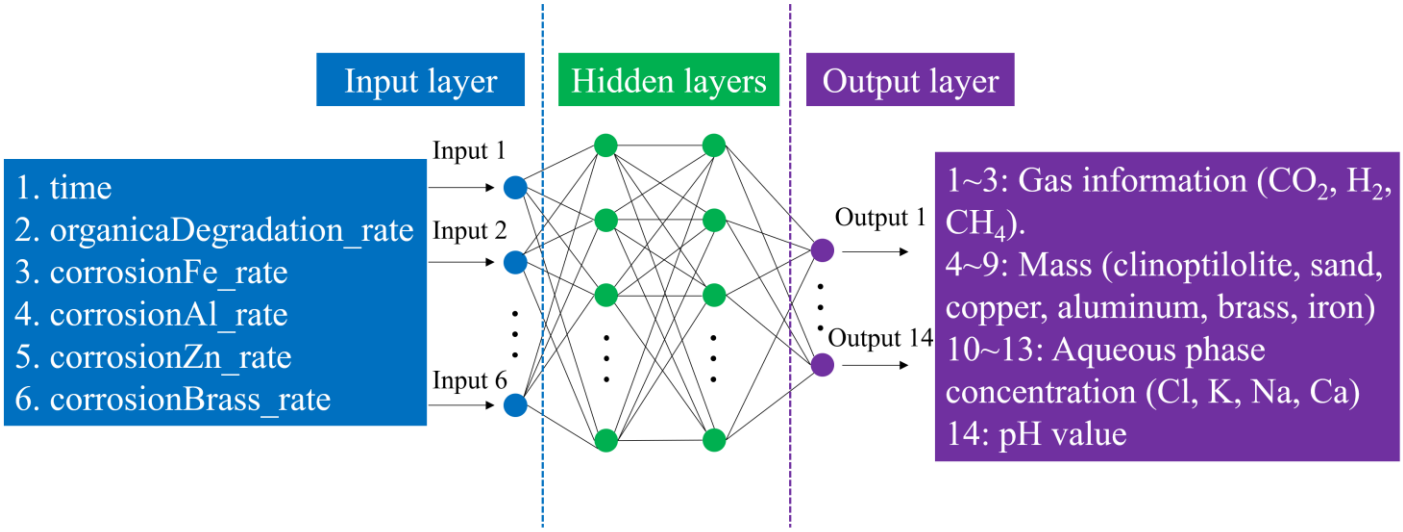

Figure 4-3 Schematic illustration of 6 inputs and 14 outputs of the NN surrogate model, from Hu et al. (2024) [14].

To generate the training datasets a range of reaction rate values was derived (Table 4-1). This range assumes an uncertainty of one order of magnitude in the reaction rate values. Utilizing an orthogonal sampling method, 25 distinct calculations are performed, each based on the values of the respective variables. The first step involves training of the NN. In the second step a sensitivity study is done on 1 million cases generated for many combinations of the input parameters using the computationally efficient NN surrogate model.

Table 4-1 Input reaction rate constant (k in a^{-1}) for organics, and reaction steady state rate (R in mol a^{-1}) of different materials with ranges assumed for the sensitivity studies. Values for generating the training datasets were derived from orthogonal sampling. One common factor (F) is used as input for the two different organic materials that is in each case multiplied with the reference rate constants, k_PVC 3.9e-5 and k_LWM 2.1e-3 [14]

Variables	Min~Max	Values
organicaDegradation_rate multiplication factor	10~1000	10, 257.5, 505, 752.5, 1000
corrosionFe_rate	2e-8~2e-6	2e-8, 5e-7, 9e-7, 1.3e-6, 1.7e-6, 2e-6
corrosionAl_rate	1e-5~1e-3	1e-5, 2.5e-4, 4.5e-4, 6.5e-4, 8.5e-4, 1e-3
corrosionZn_rate	1e-4~1e-2	1e-4, 2.475e-3, 4.45e-3, 6.425e-3, 8.4e-3, 1e-2
corrosionBrass_rate	1e-5~ 1e-3	1e-5, 2.5e-4, 4.5e-4, 6.5e-4, 8.5e-4, 1e-3

The NN used in this study includes an input layer, two hidden layers, and an output layer. The optimal number of neurons for each hidden layer was determined to be 96 (Figure 4-4), based on the

denormalized test loss as a function of neuron count and the denormalized loss across epochs for a neural network configuration with 96 neurons in each hidden layer. Using this configuration, the training time of the NN model was 51.1 seconds.

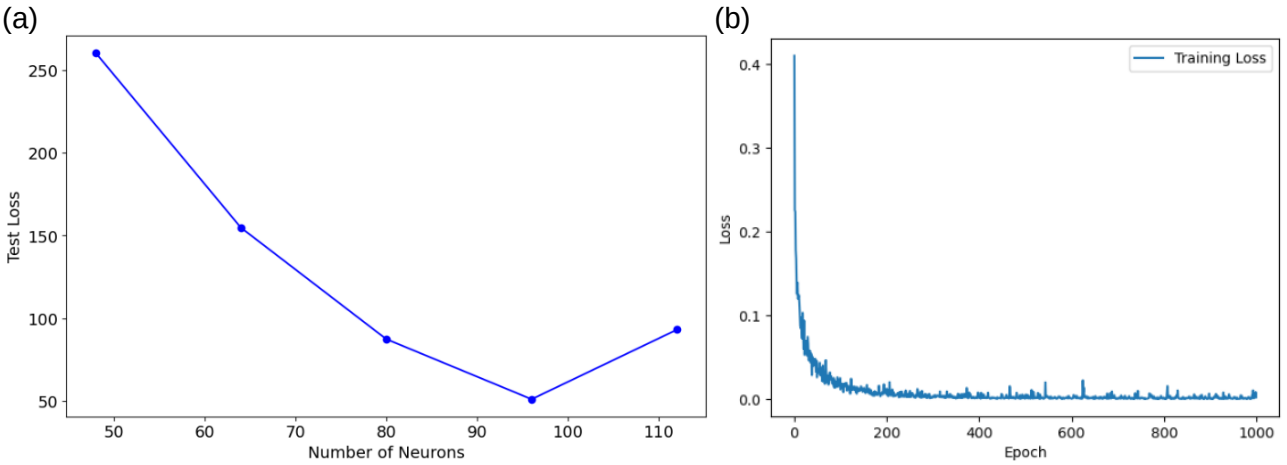

Figure 4-4 NN optimal number of neurons determination: (a) test loss vs number of neurons in each hidden layer; (b) loss vs epochs, when using 96 neurons, from Hu et al. (2024) [14].

For assessing the sensitivity of the reaction rate constants 1 million cases of degradation calculations were generated using the NN surrogate model, taking combinations of 10 different values across 6 different inputs (Table 4-2). Generating this large number of cases required merely 1.97 seconds, whereas performing the same task with the full geochemical calculation tool GEMS Python scripts would take approximately 78.9 days. This stark contrast highlights the remarkable time efficiency (~128,500 times faster) of the neural network-based surrogate model compared with a “simple” mixing tank geochemical model. This computational time difference only increases if the model is more complex, e.g., accounting for transport, mechanics feedback.

Table 4-2 Values of variables for 1 million cases with neural network-based surrogate model.

Variables	**Values**
time	0, 11.11, 22.22, 33.33, 44.44, 55.55, 66.66, 77.77, 88.88, 100.
organicaDegradation_rate multiplication factor (F)	10, 120, 230, 340, 450, 560, 670, 780, 890, 1000.
corrosionFe_rate	2.0e-08, 2.4e-07, 4.6e-07, 6.8e-07, 9.0e-07, 1.12e-06, 1.34e-06, 1.56e-06, 1.78e-06, 2.00e-06.
corrosionAl_rate	1.0e-05, 1.2e-04, 2.3e-04, 3.4e-04, 4.5e-04, 5.6e-04, 6.7e-04, 7.8e-04, 8.9e-04, 1.0e-03
corrosionZn_rate	1e-4, 1.2e-3, 2.3e-3, 3.4e-3, 4.5e-3, 5.6e-3, 6.7e-3, 7.8e-3, 8.9e-3, 1.0e-2.
corrosionBrass_rate	1.0e-05, 1.2e-04, 2.3e-04, 3.4e-04, 4.5e-04, 5.6e-04, 6.7e-04, 7.8e-04, 8.9e-04, 1.0e-03

The results of the sensitivity analysis are reported using range and variance analysis of the output properties. The range represents the difference between the maximum and minimum values, while

the variance is employed as a statistical measure to assess the spread of the data in the 1 million cases calculations. Note that the range of minimum and maximum values is calculated based on results from 0 to 100 years in each case using different rates for one input variable while keeping the other input variables constant.

(a)

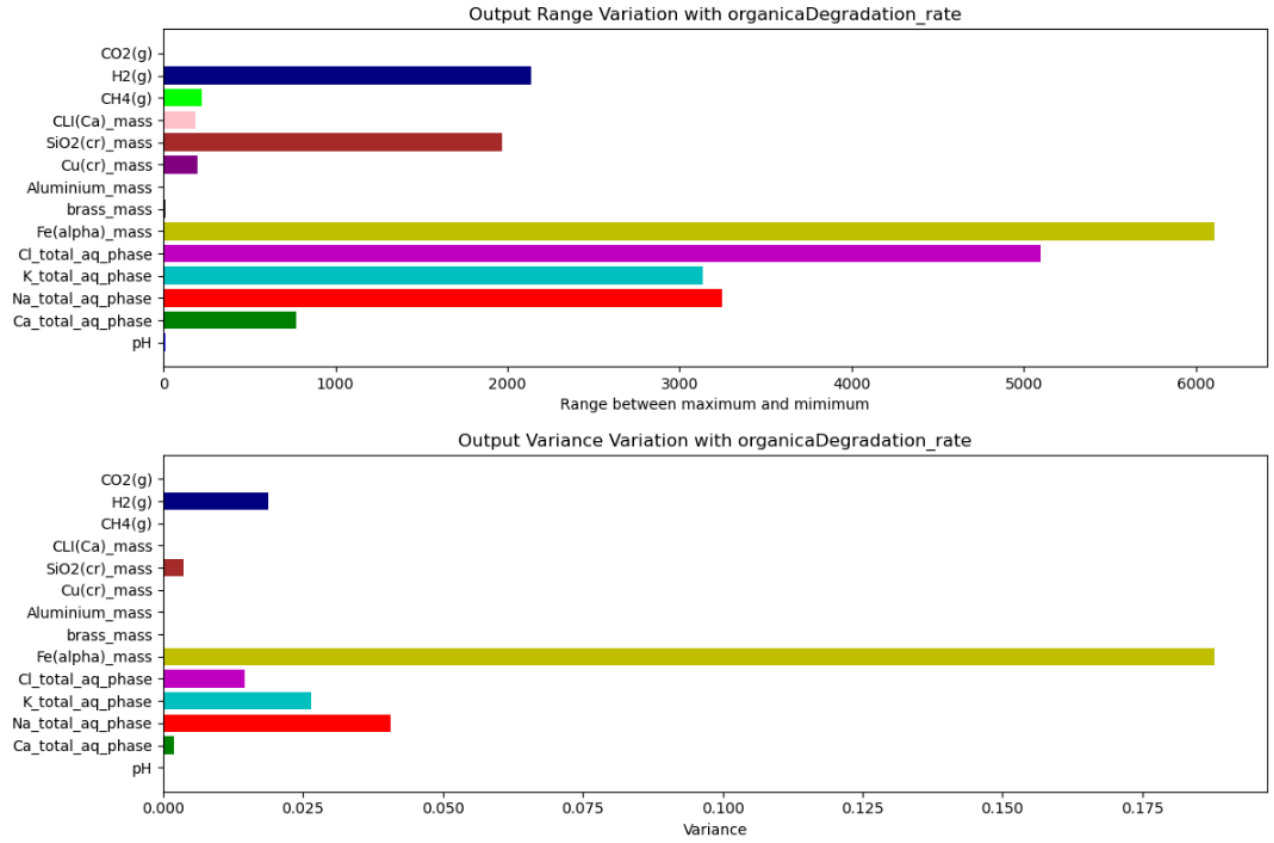

(b)

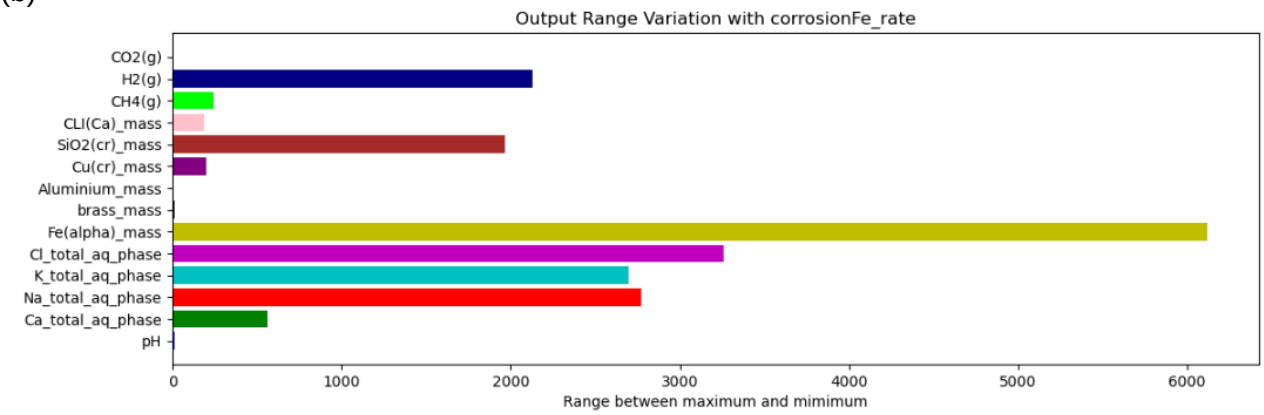

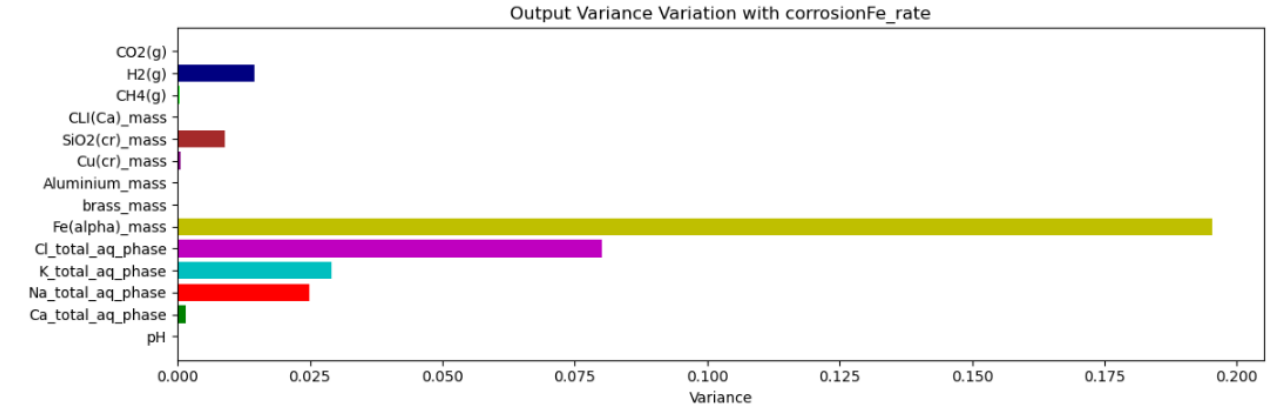
Output Variance Variation with corrosionFe_rate
CO2(g)
H2(g)
CH4(g)
CLI(Ca)_mass
SiO2(cr)_mass
Cu(cr)_mass
Aluminium_mass
brass_mass
Fe(alpha)_mass
Cl_total_aq_phase
K_total_aq_phase
Na_total_aq_phase
Ca_total_aq_phase
pH
0.000
0.025
0.050
0.075
0.100
0.125
0.150
0.175
0.200
Variance

(c)

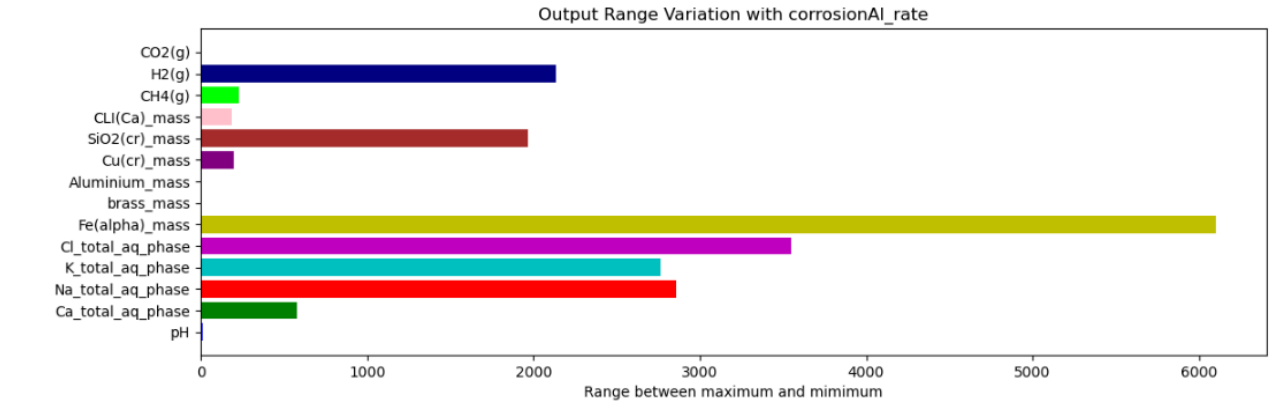
Output Range Variation with corrosionAl_rate
CO2(g)
H2(g)
CH4(g)
CLI(Ca)_mass
SiO2(cr)_mass
Cu(cr)_mass
Aluminium_mass
brass_mass
Fe(alpha)_mass
Cl_total_aq_phase
K_total_aq_phase
Na_total_aq_phase
Ca_total_aq_phase
pH
0
1000
2000
3000
4000
5000
6000
Range between maximum and mimimum

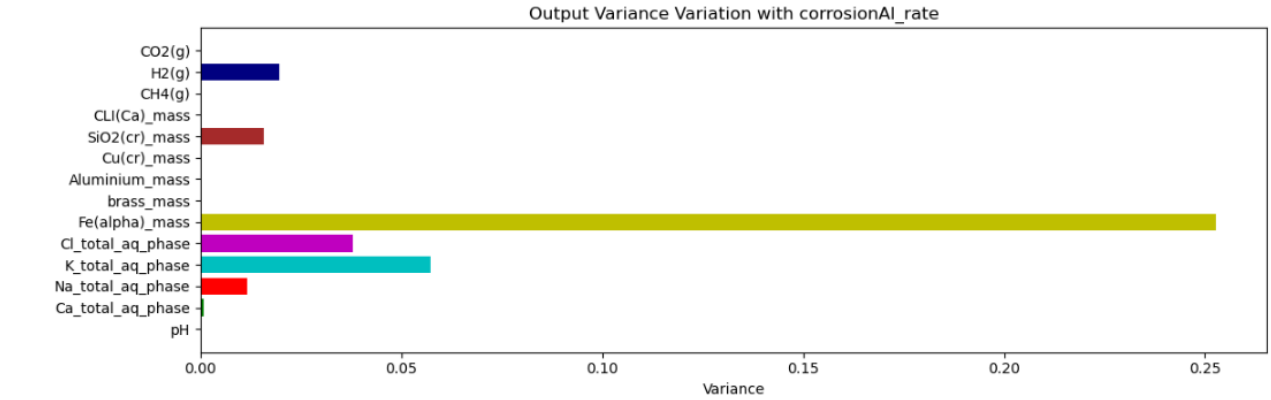
Output Variance Variation with corrosionAl_rate
CO2(g)
H2(g)
CH4(g)
CLI(Ca)_mass
SiO2(cr)_mass
Cu(cr)_mass
Aluminium_mass
brass_mass
Fe(alpha)_mass
Cl_total_aq_phase
K_total_aq_phase
Na_total_aq_phase
Ca_total_aq_phase
pH
0.00
0.05
0.10
0.15
0.20
0.25
Variance

(d)

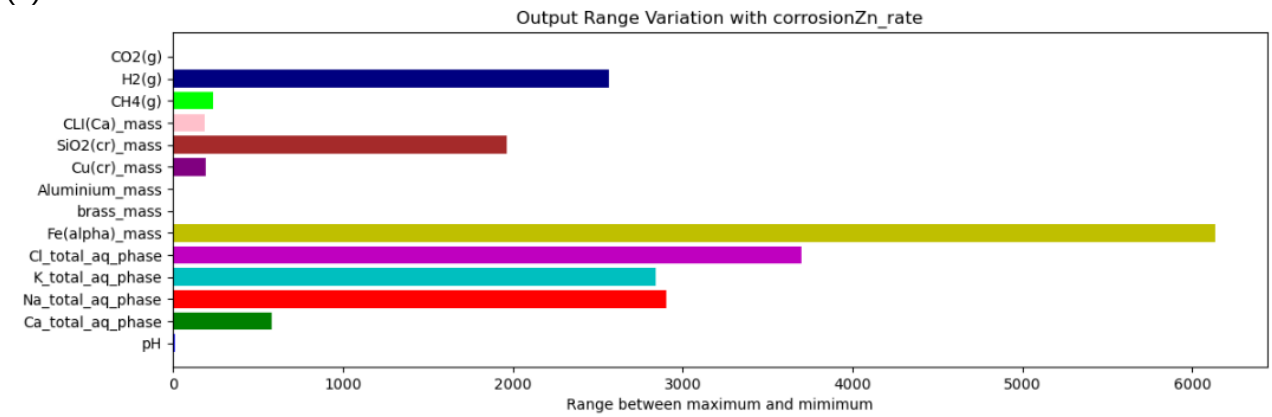
Output Range Variation with corrosionZn_rate
CO2(g)
H2(g)
CH4(g)
CLI(Ca)_mass
SiO2(cr)_mass
Cu(cr)_mass
Aluminium_mass
brass_mass
Fe(alpha)_mass
Cl_total_aq_phase
K_total_aq_phase
Na_total_aq_phase
Ca_total_aq_phase
pH
0
1000
2000
3000
4000
5000
6000
Range between maximum and mimimum

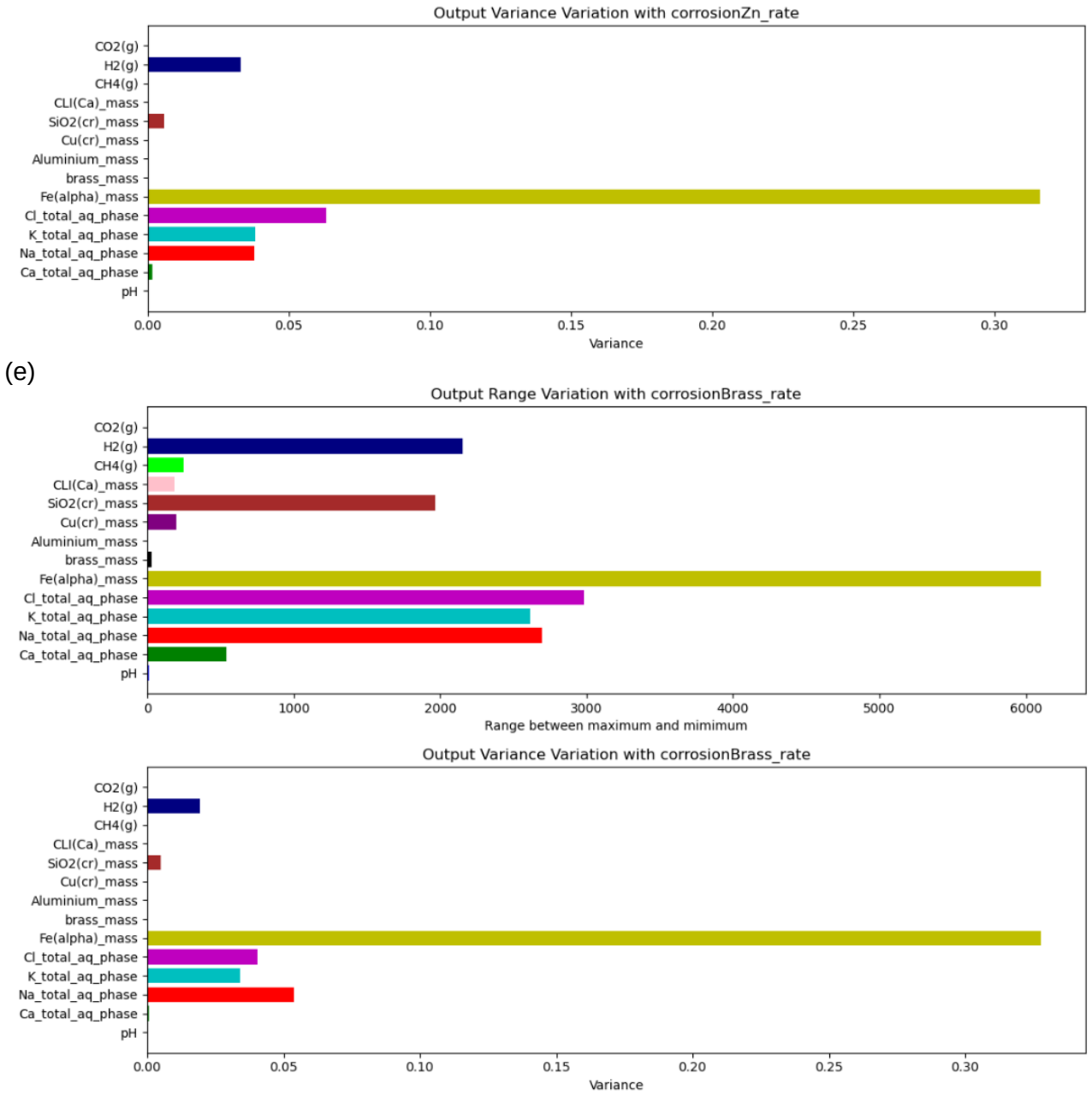

Figure 4-5 Range and variance of output parameters with values of input parameters from Hu et al. (2024) [14]: (a) organics degradation rate; (b) iron corrosion; (c) aluminium corrosion; (d) zinc corrosion; (e) brass corrosion; Output gases in mol, mass in kg, elements in aq phase in mmol/m^3.

Figure 4-5 displays the ranges and variances for the output parameters in relation to each input variable with 1 million cases.

The Digital Twin and surrogate model for the geochemical evolution of cementitious waste packages demonstrates the efficiency of neural network-based surrogate models in significantly enhancing computational efficiency, reducing the generation time of 1 million cases from nearly 79 days to under 2 seconds.

5 Model parameter updating

A significant challenge in reliably utilizing developed physics-based models lies in the uncertainties associated with them, primarily categorized into "aleatoric" and "epistemic". Aleatoric uncertainties mainly involve inaccuracies in measurements collected from experiments, while epistemic uncertainties stem from insufficient physics assumptions and uncertain model parameters. This chapter focuses on addressing the epistemic uncertainties of previously introduced models through parameter identification aligned with experimental data. This task is typically framed as an inverse problem, and its solution yields a set of more reliable model parameters, ultimately enhancing the overall reliability of the model. Solving such an inverse problem often translates to an optimization problem, where a well-defined objective function must be optimized. Optimization problems generally fall into two categories: “constrained” and “unconstrained” [17]. A widely used unconstrained optimization method is the nonlinear least-squares approach (NLLS). The primary challenges in solving optimization problems related to inverse problems are “ill-posedness” and “ill-conditioning” (see [18] for a review). Ill-posedness arises in situations with multiple or non-unique extrema of the objective function, often due to a non-continuous dependency between parameters and model response. Regularization techniques are commonly employed to address ill-posedness, with the singular value decomposition (SVD) being a notable example. SVD particularly deals with an ill-posed linear system of equations by truncating lower singular values more affected by noisy data. Alternatively, regularization can be achieved by imposing extra conditions on the parameters, such as minimum norm parameter values (Tikhonov regularization). An optimization problem can also become ill-conditioned when its solution is too sensitive to small amounts of noise in the data, making it more challenging to identify parameters accurately. This justifies the increasing trend toward utilizing stochastic approaches rather than deterministic ones in the context of model updating. Therefore, in the following subchapter, our focus narrows to Bayesian approaches for model parameter identification.

5.1 Theoretical background

Acknowledging that measurement error and model inadequacy are inevitable, a common stochastic representation of the inverse problem is

$$F(\mathbf{x}) = \mathbf{d} + \mathbf{e} \tag{5-1}$$

where $F(\cdot)$ is a deterministic, error-free forward model that expresses the relation between the unknown or uncertain model parameters $\mathbf{x}$ and the N_d-dimensional measurement data vector $\mathbf{d}$, and the noise vector term $\mathbf{e}$ lumps measurement and model errors. In this work, it is assumed that $\mathbf{e}$ follows a zero- mean multivariate Gaussian distribution, i.e., $\mathbf{e} \propto N(0, \boldsymbol{\Sigma}_e)$ with $\boldsymbol{\Sigma}_e$ a diagonal covariance matrix. If it is further assumed that the residual errors in $\mathbf{e}$ have constant variance, σ_e^2, then we have $\boldsymbol{\Sigma}_e = \sigma_e^2 \mathbf{I}$ with $\mathbf{I}$ the identity matrix.In the Bayesian paradigm, the inferred model parameters $\mathbf{x}$ are viewed as random variables with posterior pdf, $p(\mathbf{x}|\mathbf{d})$, given by

$$\mathrm{p}(\mathbf{x}|\mathbf{d}) = \frac{\mathrm{p}(\mathbf{d}|\mathbf{x})\mathrm{p}(\mathbf{x})}{\mathrm{p}(\mathbf{d})} \tag{5-2}$$

where $p(\mathbf{d}|\mathbf{x})$ signifies the likelihood function of $\mathbf{x}$ and $p(\mathbf{x})$ denotes the prior distribution of $\mathbf{x}$. Broadly speaking, $p(\mathbf{d}|\mathbf{x})$ encapsulates the misfit between measured and simulated data while $p(\mathbf{x})$ encodes the information available about $\mathbf{x}$ before collecting $\mathbf{d}$. The normalization factor, $p(\mathbf{d})$, is to be obtained from numerical integration over the parameter space so that $p(\mathbf{x}|\mathbf{d})$ is a proper probability density distribution and integrates to unity. The $p(\mathbf{d})$ quantity is generally difficult to estimate in practice but is not required for parameter inference if the dimensionality of $\mathbf{x}$ is fixed. In the remainder of this report, we will focus on the unnormalized posterior $p(\mathbf{x}|\mathbf{d}) \propto p(\mathbf{d}|\mathbf{x})p(\mathbf{x})$. Based on the Gaussian assumption for $\mathbf{e}$ in equation (5-1), $\mathbf{e} \propto N(0, \boldsymbol{\Sigma}_e)$, the likelihood function $p(\mathbf{d}|\mathbf{x})$ can be written as

$$p(\mathbf{d}|\mathbf{x}) = N(\mathbf{d}|F(\mathbf{x}), \boldsymbol{\Sigma}_e) = \frac{1}{(2\pi)^{N_d/2}} \frac{1}{\sqrt{|\boldsymbol{\Sigma}_e|}} \exp\left[-\frac{1}{2}\big(\mathbf{d} - F(\mathbf{x})\big)^{\mathrm{T}} \boldsymbol{\Sigma}_e{}^{-1} \big(\mathbf{d} - F(\mathbf{x})\big)\right] \quad (5\text{-}3)$$

As mentioned above, $\mathbf{e}$ is the sum of the measurement and model errors. The former ones are typically known but the later ones are not. How to deal with these unknown model errors within a Bayesian inversion has been the subject of much research (at least in the field of hydrologic modelling) and still remains an open issue. There are basically three possible options. First, one might just ignore them. This amounts to set the $i = 1, \dots, N_d$ diagonal elements of $\boldsymbol{\Sigma}_e$, $\sigma_{e,i}^2$, to $\sigma_{meas,i}^2$, that is, $\sigma_{e,i} = \sigma_{meas,i}$, with $\sigma_{meas,i}$ the standard deviation the i^{th} measurement error (under the constant variance assumption we thus have that all $\sigma_{e,i}$ are equal). Doing so will however lead to an underestimation of the posterior parameter uncertainty if model errors are present. Basically, the larger the model errors the more severe the uncertainty underestimation. Second, one can jointly infer the model errors, $\sigma_{model,i}$, together with the model parameters $\mathbf{x}$ (thus now inferring $p(\mathbf{z}|\mathbf{d})$ with $\mathbf{z} = [\mathbf{x}, \boldsymbol{\sigma}_{model}]$ and $\boldsymbol{\sigma}_{model} = [\sigma_{model,1}, \dots, \sigma_{model,N_d}]$) and then set $\sigma_{e,i} = \sigma_{meas,i} + \sigma_{model,i}$ in $\boldsymbol{\Sigma}_e$. This is equivalent to jointly infer $\mathbf{x}$ and $\boldsymbol{\sigma}_e$ directly, with a lower bound of $\sigma_{meas,i}$ set to the prior $\sigma_{e,i}$ distributions. This strategy is common in the hydrology and geophysics fields (e.g., [19]). However, to the best of our knowledge there is no consensus in the literature as whether jointly inferring $\mathbf{x}$ with $\boldsymbol{\sigma}_e$ will produce consistent uncertainty estimates. Lastly, one can take the arguably subjective approach of fixing the $\sigma_{e,i}$ elements to values that are deemed to "appropriately" encompass the sum of measurement and model errors.

5.2 MCMC simulation of the posterior parameter pdf

An exact analytical solution of $p(\mathbf{x}|\mathbf{d})$ is not available in many practical cases, and we therefore resort to Markov chain Monte Carlo (MCMC) simulation to generate samples from the posterior distribution. The basis of this technique is a Markov chain that generates a random walk through the search space and iteratively finds parameter sets with stable frequencies stemming from the parameter posterior pdf. Designing accurate and efficient MCMC algorithm is a field of research in itself and we refer to the textbook of Gelman et al. (2013) [20] for more details. In this study we used both the NUTS algorithm by Hoffman and Gelman (2014) [21], as implemented in the Pyro probabilistic modelling library [22], and our own Python-based version of the DREAMzs algorithm [23, 24]. NUTS is a state-of-start variant of Hamiltonian monte Carlo (HMC), which is quite efficient but requires that an accurate estimation of the gradient of the (log-)posterior density is available at low computational cost (e.g., through autodifferentiation). DREAMzs is a general-purpose MCMC algorithm that has proved to work well for many complicated inverse problems in hydrology (e.g., [24-26]) and geophysics (e.g., [27-29]), amongst other fields. For the rather simple inverse problems considered herein, we expectedly found that both NUTS and DREAMzs derive the same posterior pdf at negligible computational cost.

It is important to note that MCMC is considered as the most statistically sound method for solving inverse problems in a Bayesian way (see, e.g., [30]) but can be prohibitively slow for computationally demanding models. That is why faster alternatives that rely on different levels of approximation have been proposed. Such alternatives will be used to invert the measured drum-scale strain data, for, which the associated forward model developed by SCK CEN (which involves numerically solving the relevant PDEs with the COMSOL software) can take 10 to 15 minutes per run. Faster (but more restrictive) alternatives to MCMC to derive the posterior parameter distribution can broadly be categorized in two groups:

- The first group resorts to simplification of the forward model, e.g., by using metamodels or lower-fidelity models, to speedup evaluation of the likelihood. This acceleration comes however at the cost of introducing additional errors or bias to the inference, since the considered metamodel never approximates the physics-based model perfectly. If the metamodel is sufficiently accurate, however, then this bias can be controlled. This strategy will be investigated by SCK CEN, using either Gaussian processes (GPs) or artificial neural networks (NNs) metamodels.

- The second group includes methods that rely on simplifying assumptions about the shape of the posterior parameter pdf, e.g., Laplace approximation (INLA, [31]) or variational inference (VI, e.g.,[32]). These methods still use the original physics-based model but require far less runs than MCMC. The VB approach described in Chapter 5.3 is a VI method and assumes that the posterior parameter pdf is Gaussian.

The two inverse problems considered in this report, that is, autogenous shrinkage (AS) and ASR expansion model parameter inference based on sample-scale data, make use of simple analytical models that are computationally very cheap. Therefore, performing MCMC sampling here is straightforward.

5.3 Variational Bayesian inference

As previously mentioned, we aim at Bayesian approaches to identify unreliable/unknown parameters of the models introduced earlier. These techniques, which primarily rely on Bayes's theorem, not only handle noisy data but also address epistemic uncertainties arising from assumptions and simplifications within the model. Moreover, these methods are able to quantify the accuracy of the calibrated model in approximating reality. This is achieved through the probabilistic quantification of unknown parameters, represented as probability distribution functions (in continuous cases), as opposed to deterministic evaluations [33]. In the following, we specifically employ a variational Bayesian scheme - as an approximate formulation of the theorem - for identifying the parameters of the ASR model.

We utilize the variational Bayesian (VB) approach proposed in Chappell (2009) [34] for the estimation of model parameters, which is briefly outlined in the following. The VB method is based on an additive noise model $y = g(\theta) + e$, where y is the measurements/observations (in our case: measured strain), and e is an (additive) model error that corrects the response/output of the (forward) model g at specific positions/sensors corresponding to the observations. The function g depends on a set of unknown parameters denoted by the vector θ. In our case, g is the model given above, and θ contains the inferred material parameters. Each of the three terms y, g, and e is a vector of the same length, i.e. the number of observations. The noise e - which is the discrepancy between the model response and the measured data - is assumed to follow a zero-mean multivariate normal (MVN) distribution: $e \sim MVN(0, \Phi^{-1} I)$. Here I is an identity matrix of a respective size, and Φ is the noise-precision that describes the level of the discrepancy between the model response and the data (a higher precision, a lower discrepancy). As will be seen in the results, the VB method can estimate the noise parameter Φ along with the inference of the model parameters. For the inference, the prior/posterior of the model parameters are assumed to follow MVN distributions; i.e. $\theta \sim MVN(m, \Lambda^{-1})$, with m and Λ respectively being the mean value and the precision matrix (inverse of covariance matrix). Additionally, the prior/posterior of the noise precision Φ are assumed to follow Gamma distributions; i.e. $\Phi \sim \Gamma(c, s)$, with the two parameters (c, s) = (shape, scale). Starting from certain priors for all parameters through some deterministic values for $(m_0, \Lambda_0, c_0, s_0)$, the VB method will compute their respective posteriors (m,Λ,c,s). This is performed by minimizing the so-called Kullback–Leibler divergence that measures the distance between the true and approximated posteriors of the model parameters. Also, one requirement for using the specific VB method is being able to compute the derivative of the model response with respect to the latent parameters. For the present algebraic model, such derivatives can be obtained analytically.

6 Use case on ASR

6.1 Introduction

Predisposal waste management is to produce waste packages suitable for storage, transportation and final disposal. For decades, the nuclear industry has used cement-based materials (CBM) to immobilize low- and intermediate-level short-lived and long-lived radioactive waste. Compared to other solidification techniques, cementation is relatively simple and inexpensive. Moreover, CBM shows many advantages including a good self-shielding, and a high alkalinity allowing them to precipitate many radionuclides. One could expect that this practice would result in a stable waste form and being well compatible with the final disposal site. There are, however, many examples that show that this is not always the case. Specific issues have been addressed, such as the gel-formation attributed to ASR in the concrete operational waste of the nuclear power plant of Doel, Belgium. The cement–waste interaction disturbs the equilibrium between the pore solution of the cementitious materials and the solid phases of the cement matrix, which results in dissolution and/or precipitation of minerals. The degradation is a function of many factors including the constituent materials, its location (e.g. coastal, inland or underground for waste disposal), climatic conditions (e.g. temperature and moisture), and the presence of external agents (e.g. sulfates and chemicals). The most common chemical degradation processes include chloride ingress, sulphate attack, alkali-silica reactions, carbonation and Ca-leaching.

ASR is a deleterious reaction between the silica (from aggregates) and alkalis in pore solution or portlandite (CH) (solid phase) in the presence of water to form ASR gel (e.g., calcium potassium silicate hydrate, calcium sodium silicate hydrate). The amount of ASR gel varies depending on the reaction temperature, type and proportions of the reacting materials, gel composition, gradation of aggregates, and other factors, among them silica content and the internal structure of aggregate are the most important. Swelling of this gel leads to stress development and potentially, cracking of concrete. It has long been known that irradiation affects concrete properties. Nuclear irradiation can significantly increase the reactivity of silica-rich aggregates.

The application of some aspects of the digital twin concept to the problem of ASR of cementitious materials is presented in this chapter as a use case. First of all, an integrated approach to address the ASR of cementitious materials used for waste encapsulation is proposed. This approach includes a comprehensive laboratory and drum scale experiments, which assesses the ASR at various accelerated levels. Further, a simplified modelling framework to simulate ASR process is proposed, which is then used as the digital twin to predict the drum scale behavior. The main strategy with respect to modelling is that necessary parameters are obtained either based on literature or via calibration of material parameters with the above referenced laboratory experiments. As for the simulation of the drum scale, the goal is merely to predict and not to calibrate, at least in the first attempt. A purely geochemical approach has also been attempted. The objective is to explore semi-quantitatively the ASR potential purely on the basis of the mixture composition.

6.2 Methodology

The diagram presented in Figure 6-1 shows an integrated approach including both experimental and modelling work to assess the ASR from lab to drum scale. The new approach is proposed in order to obtain a successful digital twin validation. This approach allows to provide sufficient inputs for modelling and digital twin. Lab scale experiment is for calibration of the model, while drum scale experiment is for blind prediction.

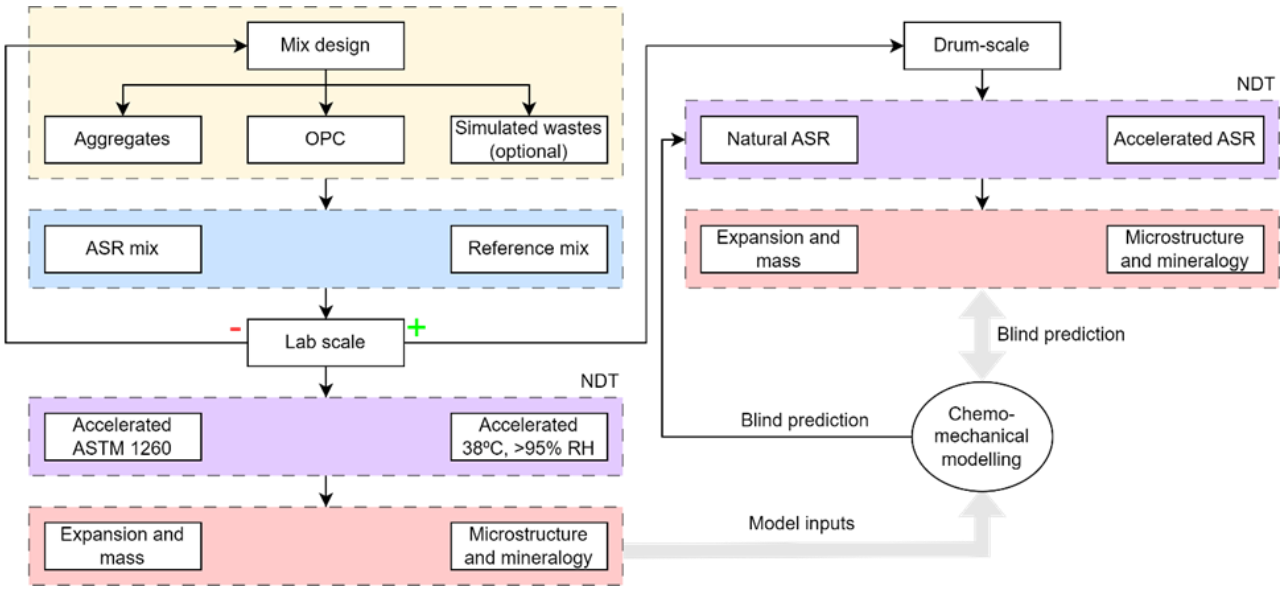

Figure 6-1 An integrated approach to assess ASR from lab to drum-scale.

6.3 Mixture design

In order to keep the system simple but still realistic, we propose to perform the experiments on mortar without the waste in this project. In this way, we will reduce the complexity of the modelling work. The combination of ASR and cement-waste interaction would introduce a new challenge for the proposed model in which we intend to use the existing chemo-mechanical constitutive laws for ASR without much change. Table 6-1 shows the compositions of 3 recipes, which are expected to give different expansion degrees due to ASR. These recipes are proposed but with slightly modified compositions suggested in ASTM standard 1260 [35] (due to the finer sand used). The recipe SIB used Sibelco M32 sand, which has been tested at Belgoprocess and classified as non-reactive sand. The recipe RCA used recycled concrete aggregates, which is expected to be more reactive. Furthermore, the recipe LI used 50% RCA and 50% Sibelco sand, but with the addition of $LiNO_3$ to mitigate the ASR. The molar ratio of Li to cement alkalis (Na + K) is 0.74 [36, 37].

Table 6-1 Mix compositions for ASR tests

Mix	Cement, kg/m^3	Water, kg/m^3	M32 sand, kg/m^3	RCA, kg/m^3	LiNO-$_3$, kg/m^3	Note
SIB	635.5	298.7	1270.9	-	-	Non-reactive (lab + drum tests)
RCA	604.6	284.2	604.6	604.6	-	Reactive (lab + drum tests)
LI	604.6	284.2	604.6	604.6	5.3	Mitigation (lab tests only)

6.4 Data pipeline

For both the lab- and drum-scale campaigns a variety of sensors were used, and interfaced through different data acquisition systems to a local server that, depending on the experiment, communicated

the data to the cloud for the purpose of data storage, data analysis, dashboard and automated alerting (Figure 6-2).

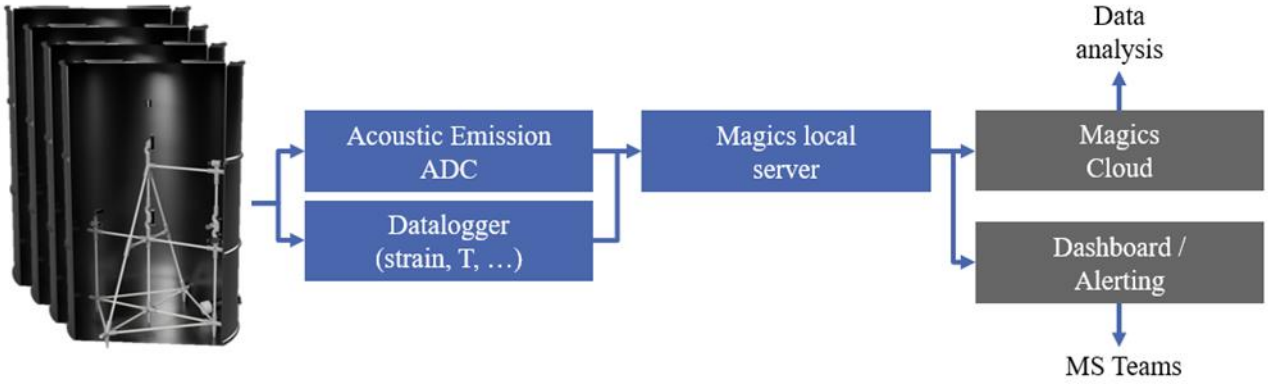

Figure 6-2 Logging architecture.

6.5 Experimental setup

6.5.1 Laboratory scale

ASR tests are performed under moderate test conditions close to realistic service conditions are also applied. The test conditions are modified from ASTM standard 1293, which is used to evaluate the potential expansion due to any form of alkali-silica reactivity [38]. After 28 days curing at 20ºC, the samples are placed inside a reactor at 38°C and relative humidity higher than 95% for 1 year as shown in Figure 6-3. Note that in this case, NaOH is added to the mix to obtain a Na_2O equivalence of 1.25% by mass of the cement. Length and weight measurements are measured monthly on all samples, including the reference sample. After 360 days, the mechanical strengths of all samples are determined. Furthermore, manual length and weight measurements were also performed.

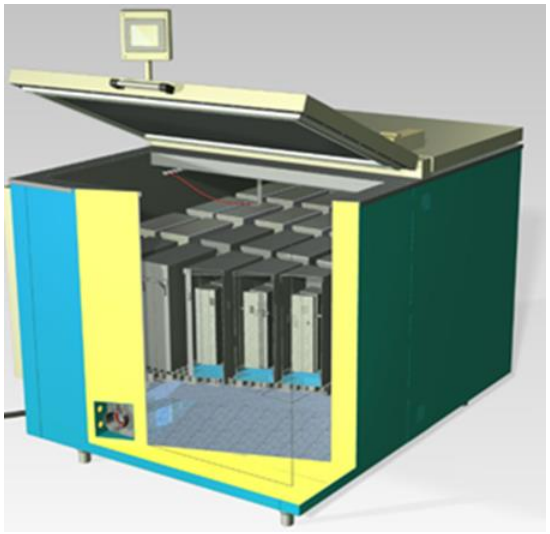

Figure 6-3 Mortar bar placement in a controlled temperature chamber, at 38 ^{o}C, for a duration of one year.

Furthermore, autogenous shrinkage experiments were conducted on two mixtures, SIB and RCA, as presented in Table 6-1. The first mixture consisted solely of raw fine aggregate (Sibelco sand), while the other included 50% recycled fine aggregate. Both mixtures were prepared with a water-cement ratio of 0.47 and an aggregate-cement ratio of 2.0. Each mortar composition was cast to undergo exposure to two different temperatures, 23 and 38 ^{o}C. For each of the four cases, two replicates were prepared to measure autogenous shrinkage. In order to replicate the moisture conditions of the recycled concrete aggregate (which is known to have intensive water absorption properties of up to 12%) as observed in drum scale experiments, the aggregate was conditioned beforehand. This conditioning process involved drying the recycled concrete aggregate and Sibelco sand in an oven at 110 ± 5 ^{o}C for one day. Subsequently, water was added to an air-tight bucket containing the aggregate to achieve an equilibrium moisture content of 6%, which was similar to the conditions in the drum scale experiments. The aggregate was conditioned under sealed conditions for one day. The mortar was then mixed according to the recommendations provided by ASTM C305-09. Afterward, the autogenous shrinkage was measured for each mortar recipe based on the guidelines provided by ASTM C1698-09.

6.5.2 Drum scale

The recipes RCA and Sib (Table 6-1) were used to cast 4 drums on the same day as shown by Figure 6-4, of which 2 drums were placed in a temperature-controlled chamber set at 38 ^{o}C to accelerate the ASR. The other 2 drums were tested under ambient temperature. Each drum was filled up to 80% of the volume to leave space for technical installation and mimic the real situation in which a gap is created to accommodate the possible gas generation. To continuously monitor, each drum was equipped with 8 vibrating strain gauges and 8 temperature sensors in the concrete. Additionally, a temperature and humidity sensor were installed at the lid of the barrel on the inside of the drum along with an ambient temperature on the outside of the drum. These sensors were read out continuously by a data acquisition unit.

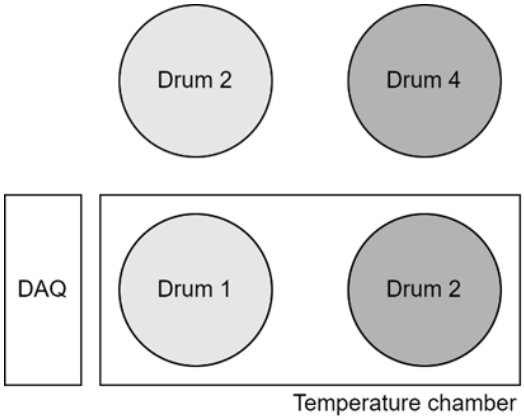

Figure 6-4 Overview of the experimental setup. In total 4 drums were equipped with sensors.

The sensors inside the drum were mounted on a printed PLA structure (see Figure 6-5) to hold these vibrating strain gauges and temperature sensors one specifically chosen locations to maximize information gain. The temperature inside the isolated temperature chamber was controlled via an independent heating belt attached to the drum (see Figure 6-5).

Figure 6-5 Sensor placement inside the drum (left) and two drums in the temperature chamber (right).

The relative locations for each of the strain gauge/temperature sensors are identical for each drum and are provided in Figure 6-6. For additional clarity, the relative coordinates with respect to the bottom and center of the barrel are provided in Table 6-2. Note that Figure 6-6 shows X and Z. Dimension Y is identical (Y=0) for each sensor location.

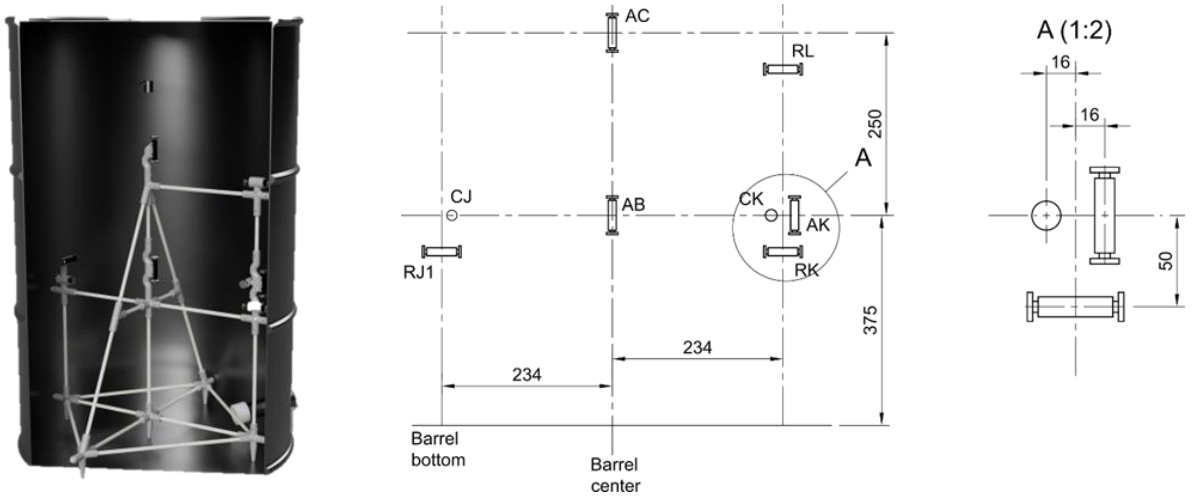

Figure 6-6 3D render of the PLA structure inside the drum (left) and the schematic concerning the relative positioning of each sensor (right).

Table 6-2 Sensor location per barrel relative to the bottom and center of the barrel.

Sensor identifier	X (mm)	Y (mm)	Z (mm)
CJ	-218	0	375
RJ	-234	0	325
AC	0	0	625
AB	0	0	375
RL	234	0	575
CK	218	0	375
AK	250	0	375

RK	234	0	325

6.6 Results

6.6.1 Laboratory scale

Figure 6-7 illustrates the progression of mass in the samples throughout the ASR experiments. In the initial stage, all three samples exhibited a rapid increase in mass within the first three months. This was subsequently followed by a gradual increase in mass. Notably, the RCA sample displayed the greatest mass increase, reaching up to 2.2% after being subjected to high humidity conditions at 38 ºC for 550 days. The addition of lithium resulted in a relative decrease in mass gain, suggesting the efficacy of mitigating ASR as the ASR gel absorbed a significant amount of water within its structure. Moreover, the increase in sample mass indicated continuous hydration of the mortar and water absorption by the aggregate, particularly in the case of recycled concrete aggregate which possesses a high-water absorption capacity of up to 12%.

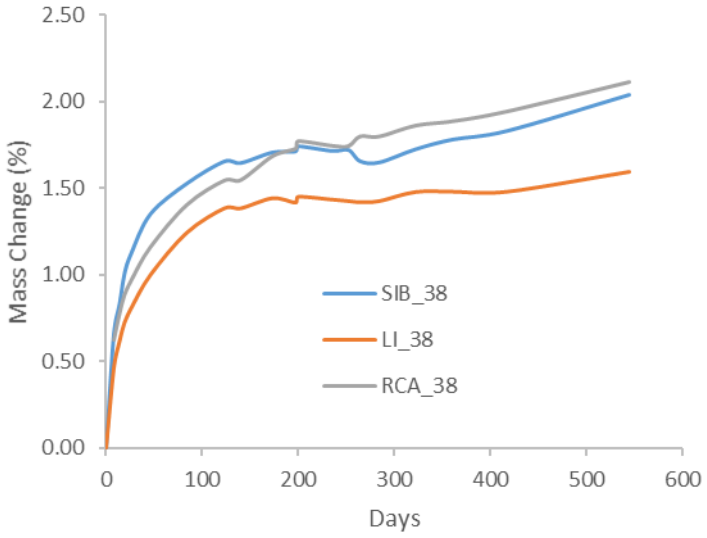

Figure 6-7 Mass evolution of samples in ASR experiments at 38 ºC.

Figure 6-8 illustrates the expansion of samples under accelerated ASR conditions at a temperature of 38 °C. The findings indicate that the RCA samples initially experienced shrinkage for a period of up to 3 months, followed by a substantial expansion phase. The expansion of RCA samples reached 0.22% over a duration of 550 days and has not yet stabilized. The inclusion of $LiNO_3$ resulted in a significant reduction in expansion by a factor of 5. In contrast, the SIB sample, classified as non-reactive, exhibited the least expansion, with only 0.03% (after 550 days of testing), which is well below the ASTM standard threshold of 0.1% for assessing susceptibility to ASR. Monitoring of the ongoing tests is still underway.

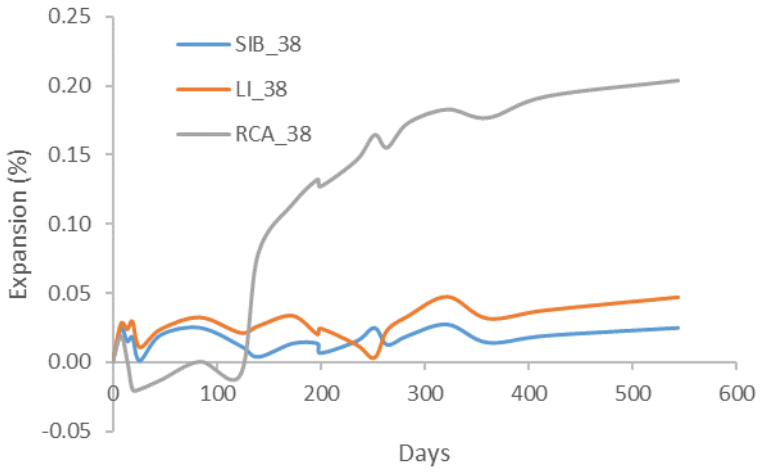

Figure 6-8 Expansion of samples in ASR experiments at 38 °C.

The ASR experimental results indicate a decrease in sample size during the initial stage. To validate this observation and gather information for modeling purposes (Chapter 6.7), autogenous shrinkage experiments were conducted. Figure 6-9 clearly illustrates that the RCA samples exhibited significant autogenous shrinkage during the first two weeks, followed by a period of gradual/stable shrinkage. The increase in temperature from 20 ºC to 38 ºC accelerates the shrinkage process, particularly in the first week. After four weeks, the autogenous shrinkage of the RCA sample reached 280 and 330 microstrains for temperatures of 20 and 38 ºC, respectively. The SIB sample displayed similar shrinkage characteristics, although with a much lower magnitude. The autogenous shrinkage of the SIB sample reached 57 and 150 microstrains for temperatures of 20 and 38 ºC, respectively. It is important to note that the temperature appears to have a substantial impact on the autogenous shrinkage of the SIB sample compared to the RCA sample.

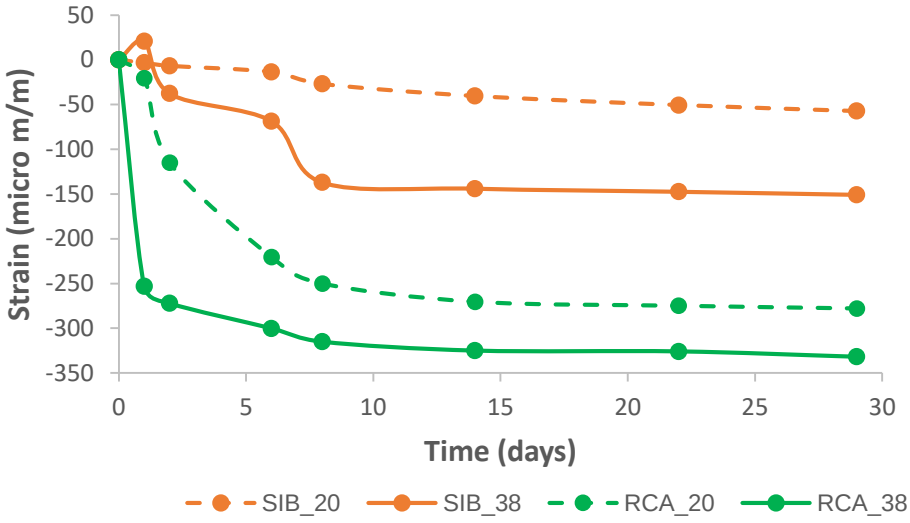

Figure 6-9 Autogenous shrinkage strain evolution for the RCA mix.

6.6.2 Drum scale

Figure 6-10 illustrates the temperature changes observed in drum scale experiments over a period of 1 year. Drums 2 and 4 were exposed to ambient conditions, causing the temperatures to fluctuate in accordance with seasonal variations. During winter, temperatures could drop as low as 10 ºC, while in summer, they reached highs of 23 ºC for the thermocouple installed in the lid of the drums.

The temperature inside the drum remained relatively consistent across different measurement points. However, there was a discrepancy of approximately 5 °C between the temperatures recorded at the lid and inside the cementitious matrix, which proved challenging to explain. This disparity could be attributed to the ongoing heat release from mortar hydration or simply the varying performance of the temperature sensors in air conditions versus the cementitious matrix.

Drums 1 and 3, on the other hand, were placed in a climate chamber with a controlled temperature of 38 °C, resulting in stable temperature levels. The temperatures measured at the lid aligned closely with the controlled temperatures. The temperature profiles of the cementitious matrix exhibited similar patterns to those observed in drums 1 and 3. Again, a 5 °C difference between the lid and matrix temperature was noted for drums 2 and 4. It should be noted that drum 1 experienced a temperature spike at 160 days due to inspection activities. In this instance, the drum was opened for a brief period of 15 minutes to assess the moisture state and surface cracking of the mortar. The impact of the temperature spikes can also be seen in strain measurements (Figure 6-11).

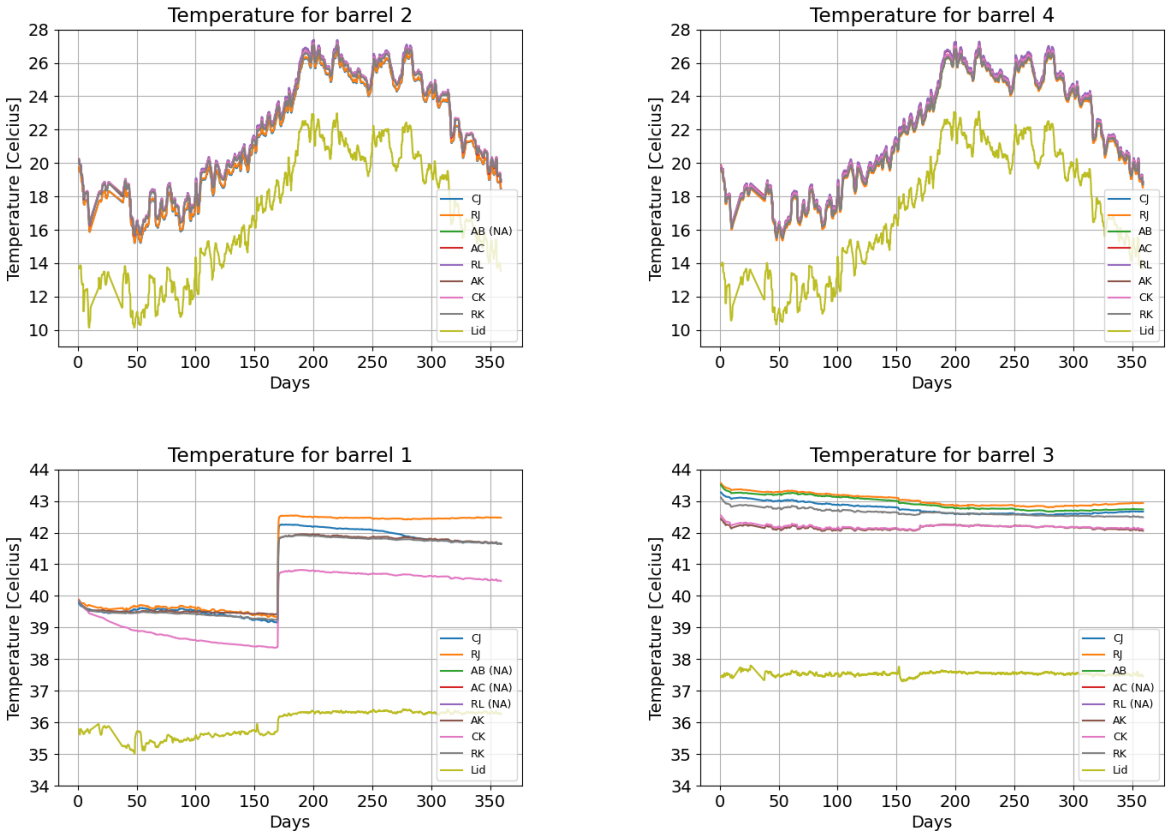

Figure 6-10 Temperature evolution in the drum scale experiments.

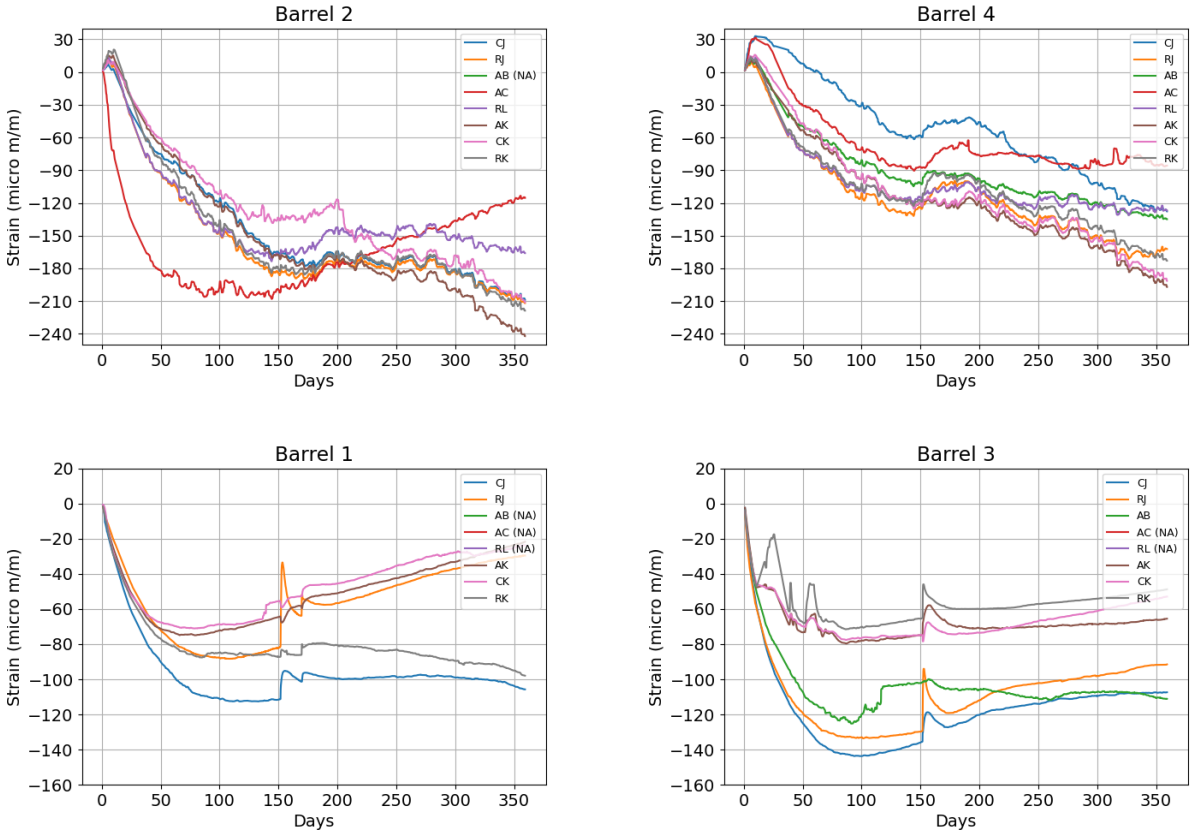

Figure 6-11 Temperature corrected strain evolution in the drum scale experiments.

Figure 6-11 shows the temperature corrected strain evolution at various sensor locations. Overall, the drums (2 and 3) that were exposed to ambient conditions show shrinkage. This implies that ASR effects have not yet been observed, which is expected given that these drums are not under accelerated conditions. However, the sensor AC in drum 2, i.e. at the core of the drum, showed reversal in strain evolution indicating a possible expansion mechanism, which is difficult to explain. Drum 1, which mainly contains non-reactive silica (SIB) and subjected to higher temperature surprisingly showed a shift towards expansion for some sensors. These are contrary to the lab scale experimental data that showed no appreciable ASR expansion for SIB material as seen in Figure 8-8, with a maximum of 0.025% reached after 500 days, in comparison to 0.2% reached by RCA. Only after post characterization of drum 1 can a justifiable explanation be provided.

ASR was expected to mainly happen in drum 3 as it is at higher temperature (38 °C) and with the most susceptible mix, i.e. RCA mix. However, drum 3 displayed predominantly shrinkage behavior, although there is a slow trend towards expansion after 150 days for some sensors. At this stage, it is hard to speculate to what extent ASR may have contributed to the shift towards expansion. It is postulated that the ASR process is delayed in drum 3 because of a lack of free water for ASR to manifest to its full potential. This is a plausible scenario as the dry RCA has the potential to also absorb water, which was seen in lab conditions. The absorption can be as high as 12% by weight. If this scenario exists in drum 3, it is possible that not enough water would be available for the ASR to develop or that it might take a significantly longer time for its effect to be seen. As it stands, the drum scale experiments are expected to continue until the end of 2024 allowing us to see the evolution of strains. Post characterization of drum 3 material will be carried out after dismantling, which might explain the observed behavior.

6.7 Thermo- hydro-mechanical model for ASR

From the laboratory experimental results, it is evident that RCA mixture is producing the maximum ASR induced expansion. Thus drum 3 would be the best choice to demonstrate the applicability of

the digital twin concept. Furthermore, from drum scale measurements, it is evident that temperature varies significantly during the first few days of hydration, following which a more or less steady state is attained and any fluctuations are attributed to the heater in the chamber. Secondly, as postulated in Chapter 6.6.2, the delay in ASR expansion in the drum may be attributed to a lack of moisture content to sustain ASR. Therefore, it is necessary to incorporate the effect of temperature and moisture field into the model. In this work, standard partial differential equations for heat transfer and moisture transfer are used. Whereas the mechanical model solves the standard momentum balance equation with linear elastic constitutive law as follows:

$$\nabla . \boldsymbol{\sigma} = \mathbf{b} \tag{6-1}$$

$$\boldsymbol{\sigma} = \mathbf{D} : (\boldsymbol{\varepsilon} - \boldsymbol{\varepsilon}_{\mathbf{ASR}} - \boldsymbol{\varepsilon}_{\mathbf{as}} - \boldsymbol{\varepsilon}_{\mathbf{t}}) \tag{6-2}$$

where $\boldsymbol{\varepsilon}_{\mathbf{ASR}}$ is the ASR expansion strain tensor, $\boldsymbol{\varepsilon}_{\mathbf{as}}$ is the autogenous shrinkage strain tensor and $\boldsymbol{\varepsilon}_{\mathbf{t}}$ is the thermal strain tensor, $\boldsymbol{\sigma}$ is the stress tensor and **b** is the body force vector. The ASR expansion strain relationship is based on Seignol et al. [39] and is fitted to the experimental data as described in Chapter 6.7.4. The autogenous shrinkage strain relationship is based on B4 model [40] and is fitted to the experimental data as described in Chapter 6.7.4. The thermal strain follows the standard linear relationship with change in temperature via the thermal expansion coefficient.

Moisture transport equation follows the approach given in [41]:

$$\frac{\partial w_e}{\partial h}\frac{\partial h}{\partial t} = \nabla \cdot D_m \frac{\partial w_e}{\partial h}\nabla h + k_c w_c \frac{d\alpha}{dt} \tag{6-3}$$

Where w_e is the evaporable water content, h is the relative humidity, k_c is a constant that refers to maximum water content that is consumed during hydration, w_c is the weight content of cement in the mortar and α is the degree of hydration, which follows the approach discussed in Phung et al. [42] and its parameters are fitted based on isothermal calorimetric experiments as shown in Table 6-2. D_m is based on Eq. (10) in [43] and detailed in

6.7.1 Parameter estimation

6.7.1.1 Inference of the AS model parameters using MCMC

A MCMC inversion of sample-scale autogenous shrinkage measurement data, $\eta_{meas,40}$ and $\eta_{meas,20}$ [µm/m], was performed to derive the α [-], β [-], τ_{40} [days] and τ_{20} [days] parameters of the following autogenous shrinkage analytical models

$$\eta_{sim,40} = \eta_\infty \left[1 + \left(\frac{\tau_{40}}{t}\right)^\alpha\right]^\beta \text{ and} \tag{6-5}$$

$$\eta_{sim,20} = \eta_\infty \left[1 + \left(\frac{\tau_{20}}{t}\right)^\alpha\right]^\beta$$

where t is measurement time in days since the start of the experiment, α and β are to be estimated jointly for the two measured time series and η_∞ is set to 492.3735 µm/m.

Here based on expert opinion the $\sigma_{e,i}$ in $\boldsymbol{\Sigma}_e$ (see equation (5-3)) were set to 15 µm/m for measurements taken after day 5 and to 30 µm/m for measurements taken after day 5. Figure 6-13 depicts the derived posterior parameter distribution while Figure 6-14 shows the associated predictions. It is seen that the α and β parameters are well resolved with approximately Gaussian marginal posterior distributions that show a relatively small spread. In contrast, the marginal posterior distributions of τ_{40} and τ_{20} are far from Gaussian-like and are much wider, with respect to their prior

distributions, than those of α and β. The marginal posterior uncertainty of τ_{20}, in particular, is basically as large as its prior uncertainty.

The derived maximum a posteriori solution (MAP) is then used to obtain the ASR measurement data used in the next chapter. In other words, the measurements obtained in the ASR tests are total strains, thus including autogenous shrinkage strains as well. But the autogenous shrinkage component must be removed to obtain purely ASR expansion data. Note that this approach had to be taken because autogenous shrinkage and ASR measurements were not carried out for equal durations and measurements were not taken with the same frequency so as to directly subtract measured AS strains from the total strains to obtain ASR strains.

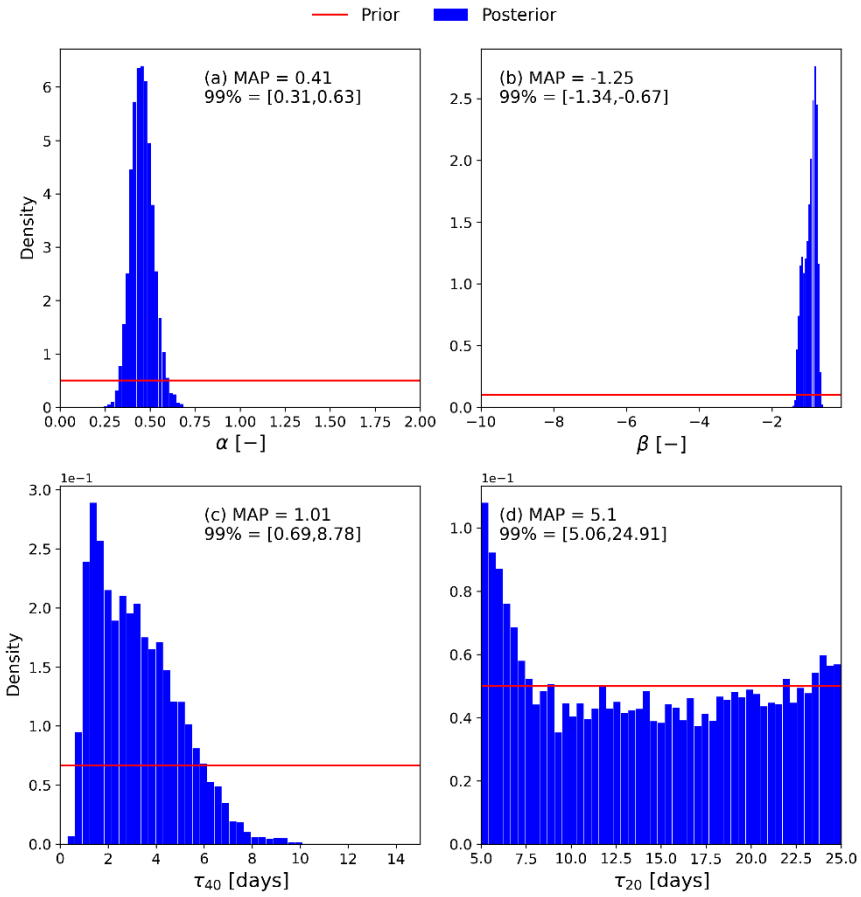

Figure 6-13: Marginal posterior distributions of the inferred autogenous shrinkage model parameters from sample-scale data. MAP denotes the maximum a posteriori solution, that is, the solution with maximum posterior density among the collected posterior parameter sets.

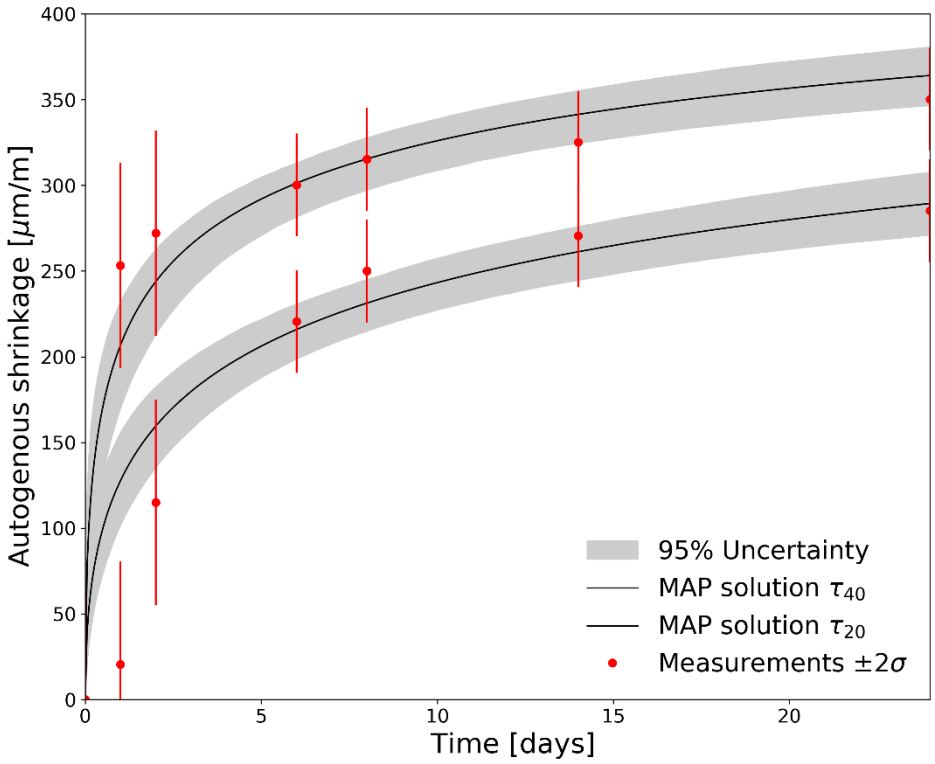

Figure 6-14: MAP predictions and 95% Posterior predictive uncertainty for the autogenous shrinkage model parameter inference.

6.7.1.2 Inference of the ASR model parameters using MCMC

The measurement errors associated with the sample-scale ASR measurement data, ε [-], are deemed to have a constant standard deviation, σ_{meas} of 0.01 [-]. For the MCMC inversion, the ASR analytical model parameters and constant standard deviation of the residual errors, σ_e are then jointly derived, fixing the lower bound of $p(\sigma_e)$ to σ_{meas}. The considered ASR analytical model is

$$\varepsilon_{sim} = \varepsilon_{\infty} \frac{1 - e^{-t/\tau_c}}{1 + e^{(-t+\tau_L)/\tau_c}} \frac{1-\phi}{\delta + t} \tag{6-6}$$

where t is measurement time in days since the start of the experiment, τ_C [days] and τ_L [days] are characteristic and delay times, respectively, δ and ϕ are empirical parameters and ε_{∞} is set to 0.2483 [-].

The τ_C, τ_L, δ, ϕ and σ_e parameters were inferred simultaneously, with the (required) additional constraint that $\delta > \phi$. Figure 6-15 presents the obtained marginal posterior distributions while Figure 6-16 depicts the resulting predictive uncertainty. It is observed that the δ and ϕ parameters are not well informed by the measurement data since their posterior uncertainty remains almost as large as their prior uncertainty (Figure 6-15). In contrast, the τ_C, τ_L and σ_e parameters are reasonably well resolved with a rather small posterior uncertainty compared to their prior uncertainty. Furthermore, the $\log_{10}(\sigma_e)$ marginal posterior distribution closely resembles a Gaussian distribution with a mean of -1.79 which corresponds to a value of 0.016 [-]. With respect to model predictions, the measured ASR data from day 15 on are overall well captured by the calibrated model (Figure 6-16).

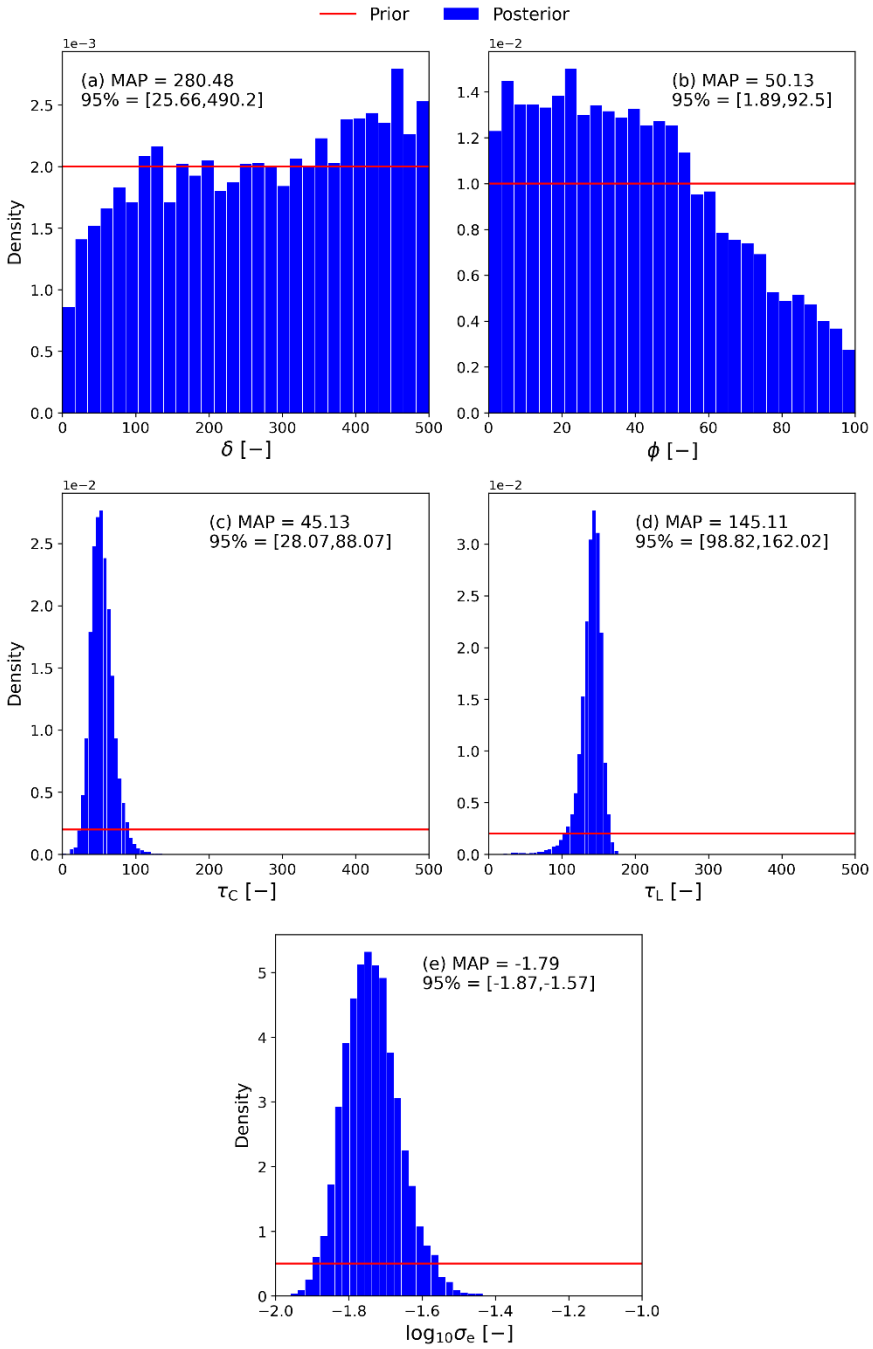

Figure 6-15: Marginal posterior distributions of the inferred ASR model parameters and standard deviation of the residual errors, derived from inversion of the sample-scale ASR measurement data.

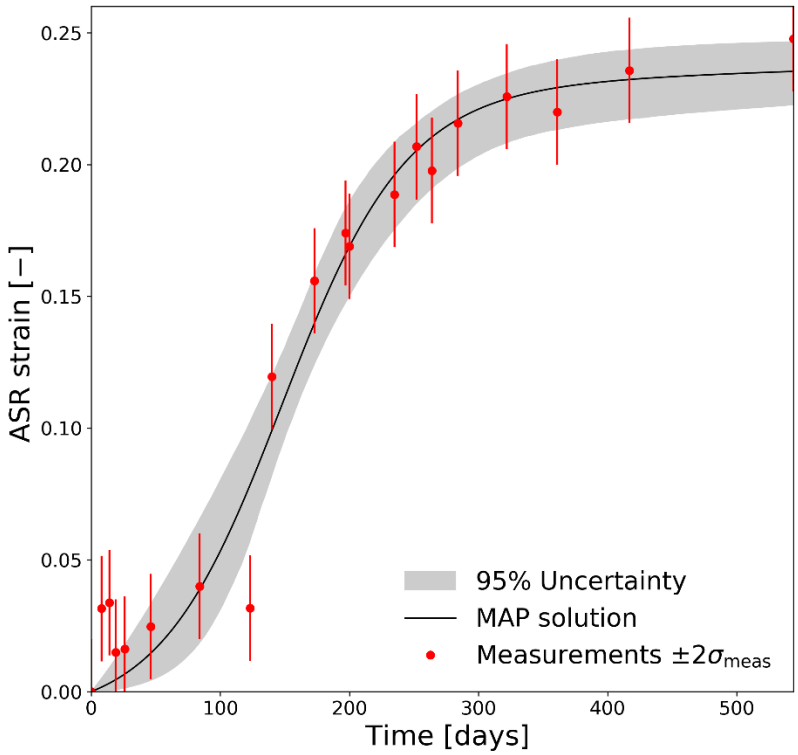

Figure 6-16: MAP predictions and 95% Posterior predictive uncertainty for the ASR model parameter inference.

6.7.1.3 Inference of the ASR model using variational Bayesian inference

The evolution of the chemical strain over the course of time is modelled through the following algebraic equation. This is a slight variant of Equation 5-5.

$$\varepsilon = \varepsilon_{\infty} \frac{1 - e^{-t/\tau_c}}{1 - e^{-(t-\tau_L)/\tau_c}} \tag{6-7}$$

with the model parameters τ_c and τ_L to be identified. t is time and ε is the chemical strain (expansion), which are measured in a lab-scale experiment. The goal is to infer the parameters mentioned above using the Bayes's theorem, which then enables us to predict the behaviour of ASR expansion in a probabilistic way, i.e. after obtaining posteriors of the parameters a predictive posterior for the strain can be computed. The idea is then to plug such a probabilistic model into a structural model (typically a finite element model) that is established to represent a drum-scale experiment.

In Figure 6-17, the prior/posteriors of the model parameters as well as the noise precision is depicted. Respective mean values and standard deviations are presented, as well. Note that the mean value of the inferred noise precision (1.89e4) corresponds to a standard deviation of 0.0073.

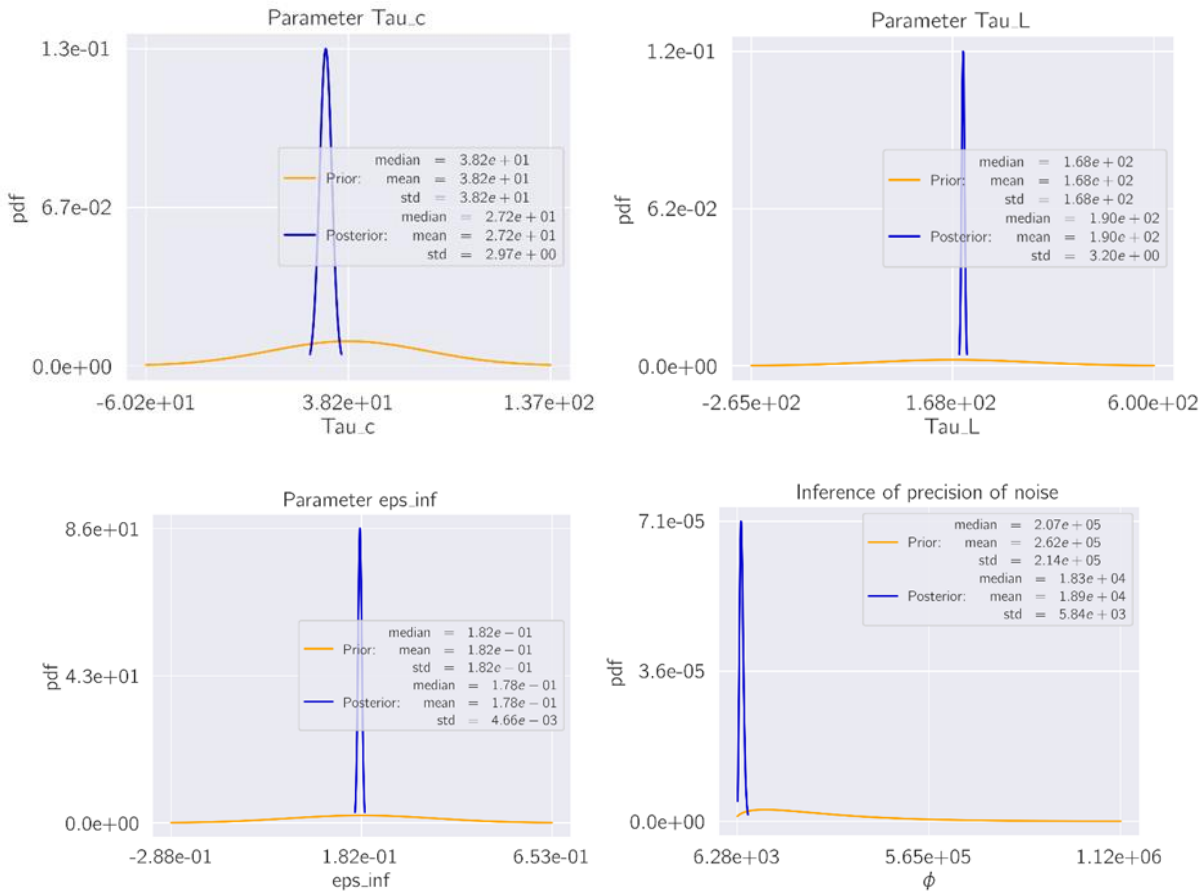

Figure 6-17 Prior/posteriors of the model parameters and the noise precision

Identifying model parameters in the form of probability distributions provides a probabilistic model, which can predict the behavior of the system in a probabilistic way. Figure 6-18 shows such a probabilistic predictive model response in comparison to the data. In addition, a deterministic identification has been performed and reported, which essentially is a least-square minimization of the model error (2) with respect to the model parameters. This is performed by means of the 'scipy.optimize' package in Python. Notice that, the identified parameters obtained from this deterministic method coincide the mean values of the posteriors from the VB.

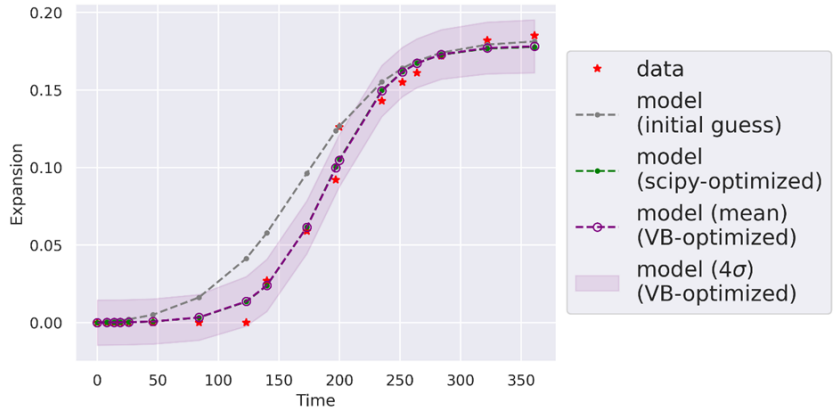

Figure 6-18 – Model response (predictive) versus data

We should recognize that a fundamental assumption of the presented Bayesian inference procedure is the additive noise model. This means, the error that we expect/formulate in the model response

does not depend on the magnitude of the model response itself. The dependency of the model error on the model response itself can be handled e.g. by a multiplicative noise model. This obviously has not been studied here, nevertheless, can be considered as a good continuation of this work for improving the accuracy and predictability of the calibrated model.

6.7.2 Summary of material parameters

Table 6-4 and

Table 6-5 provide parameters for the material models.

Table 6-4.

Heat transfer equation follow the approach given in [42]:

$$C_{ps}\rho_b \frac{\partial T}{\partial t} = \nabla \cdot \lambda \nabla \mathrm{T} + w_c Q_\infty \frac{d\alpha}{dt} \quad (6\text{-}4)$$

where T is the temperature, C_{ps} is the specific heat capacity, ρ_b is the bulk density, λ is the thermal conductivity, Q_∞ is the maximum heat of hydration.

6.7.3 Domain, initial and boundary conditions

All the four cylindrical drums are identical in dimensions and the mortar is filled up to 85% of the drum height. Typical dimensions of a drum are shown in Figure 6-12.

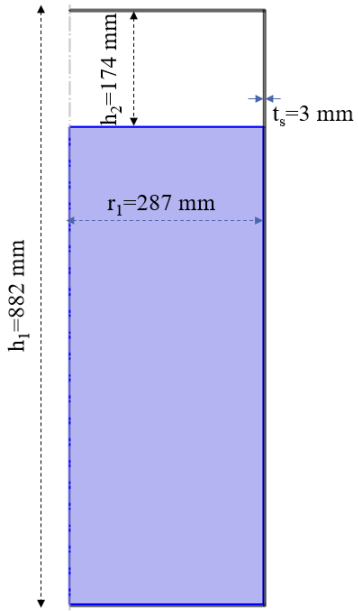

Figure 6-12 2D axisymmetric schematic of a typical drum.

The temperature boundary condition on all sides is as defined in Table 6-3:

Table 6-3 Temperature boundary condition.

Time (days)	Temperature (°C)
< 0.3 days	No heat loss
0.3	60
1	70
1.9	18
2	39

The initial relative humidity is taken as 0.77 based on hydration kinetics calculations. Relative humidity on the top surface of the mortar is fixed at 1 because of the presence of water filled tray to maintain saturated conditions.

As for the mechanical model, the bottom surface is vertically restrained, and the remaining faces are free to deform. The circumferential interface between the mortar and the steel drum is defined via a contact boundary with friction.

6.7.4 Parameter estimation

6.7.4.1 Inference of the AS model parameters using MCMC

A MCMC inversion of sample-scale autogenous shrinkage measurement data, $\eta_{meas,40}$ and $\eta_{meas,20}$ [µm/m], was performed to derive the α [-], β [-], τ_{40} [days] and τ_{20} [days] parameters of the following autogenous shrinkage analytical models

$$\eta_{sim,40} = \eta_\infty \left[1 + \left(\frac{\tau_{40}}{t}\right)^{\alpha}\right]^{\beta} \text{ and} \qquad (6\text{-}5)$$

$$\eta_{sim,20} = \eta_\infty \left[1 + \left(\frac{\tau_{20}}{t}\right)^{\alpha}\right]^{\beta}$$

where t is measurement time in days since the start of the experiment, α and β are to be estimated jointly for the two measured time series and η_∞ is set to 492.3735 µm/m.

Here based on expert opinion the $\sigma_{e,i}$ in $\mathbf{\Sigma}_e$ (see equation (5-3)) were set to 15 µm/m for measurements taken after day 5 and to 30 µm/m for measurements taken after day 5. Figure 6-13 depicts the derived posterior parameter distribution while Figure 6-14 shows the associated predictions. It is seen that the α and β parameters are well resolved with approximately Gaussian marginal posterior distributions that show a relatively small spread. In contrast, the marginal posterior distributions of τ_{40} and τ_{20} are far from Gaussian-like and are much wider, with respect to their prior distributions, than those of α and β. The marginal posterior uncertainty of τ_{20}, in particular, is basically as large as its prior uncertainty.

The derived maximum a posteriori solution (MAP) is then used to obtain the ASR measurement data used in the next chapter. In other words, the measurements obtained in the ASR tests are total strains, thus including autogenous shrinkage strains as well. But the autogenous shrinkage component must be removed to obtain purely ASR expansion data. Note that this approach had to be taken because autogenous shrinkage and ASR measurements were not carried out for equal durations and measurements were not taken with the same frequency so as to directly subtract measured AS strains from the total strains to obtain ASR strains.

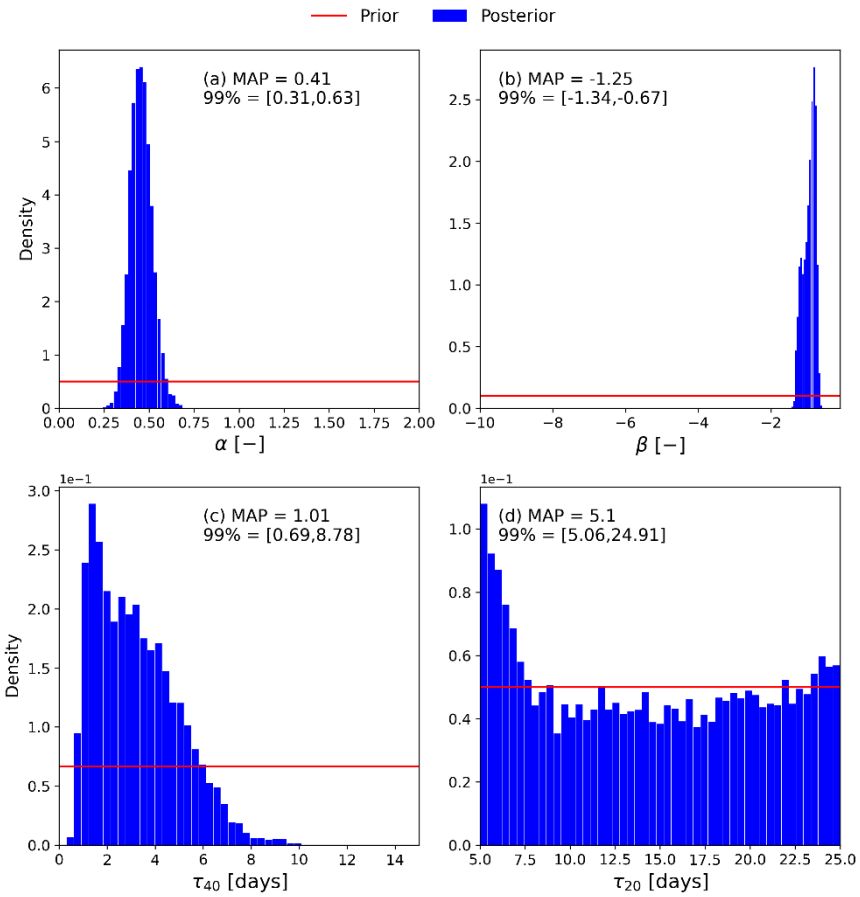

Figure 6-13: Marginal posterior distributions of the inferred autogenous shrinkage model parameters from sample-scale data. MAP denotes the maximum a posteriori solution, that is, the solution with maximum posterior density among the collected posterior parameter sets.

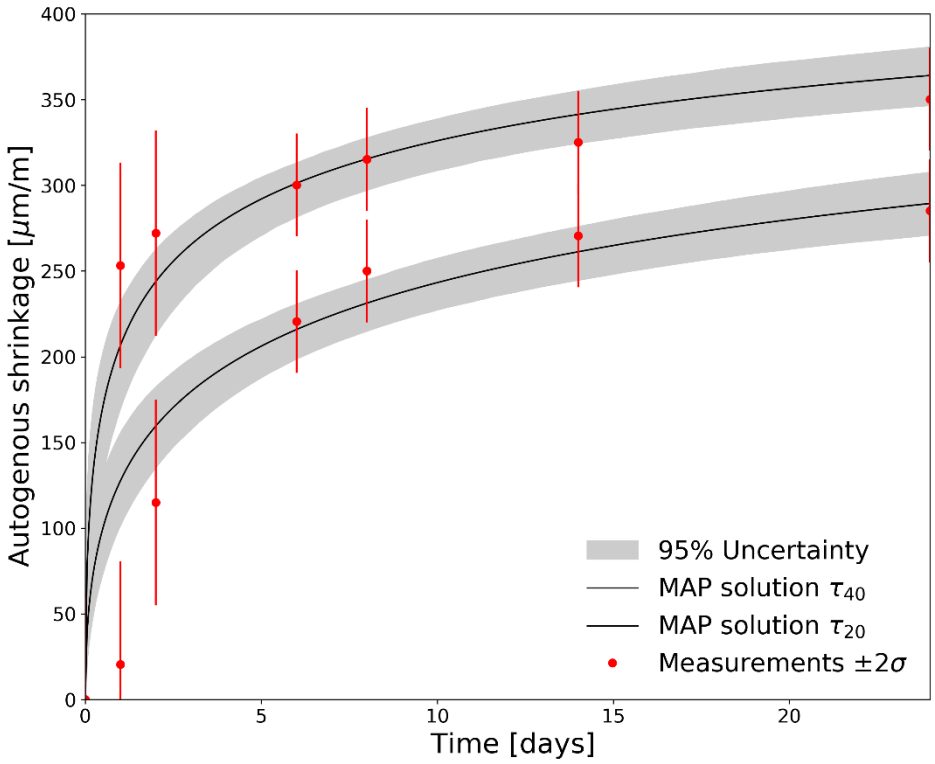

Figure 6-14: MAP predictions and 95% Posterior predictive uncertainty for the autogenous shrinkage model parameter inference.

6.7.4.2 Inference of the ASR model parameters using MCMC

The measurement errors associated with the sample-scale ASR measurement data, ε [-], are deemed to have a constant standard deviation, σ_{meas} of 0.01 [-]. For the MCMC inversion, the ASR analytical model parameters and constant standard deviation of the residual errors, σ_e are then jointly derived, fixing the lower bound of $p(\sigma_e)$ to σ_{meas}. The considered ASR analytical model is

$$\varepsilon_{sim} = \varepsilon_{\infty} \frac{1 - e^{-t/\tau_c}}{1 + e^{(-t+\tau_L)/\tau_c}} \frac{1-\phi}{\delta + t} \tag{6-6}$$

where t is measurement time in days since the start of the experiment, τ_C [days] and τ_L [days] are characteristic and delay times, respectively, δ and ϕ are empirical parameters and ε_{∞} is set to 0.2483 [-].

The τ_C, τ_L, δ, ϕ and σ_e parameters were inferred simultaneously, with the (required) additional constraint that $\delta > \phi$. Figure 6-15 presents the obtained marginal posterior distributions while Figure 6-16 depicts the resulting predictive uncertainty. It is observed that the δ and ϕ parameters are not well informed by the measurement data since their posterior uncertainty remains almost as large as their prior uncertainty (Figure 6-15). In contrast, the τ_C, τ_L and σ_e parameters are reasonably well resolved with a rather small posterior uncertainty compared to their prior uncertainty. Furthermore, the $\log_{10}(\sigma_e)$ marginal posterior distribution closely resembles a Gaussian distribution with a mean of -1.79 which corresponds to a value of 0.016 [-]. With respect to model predictions, the measured ASR data from day 15 on are overall well captured by the calibrated model (Figure 6-16).

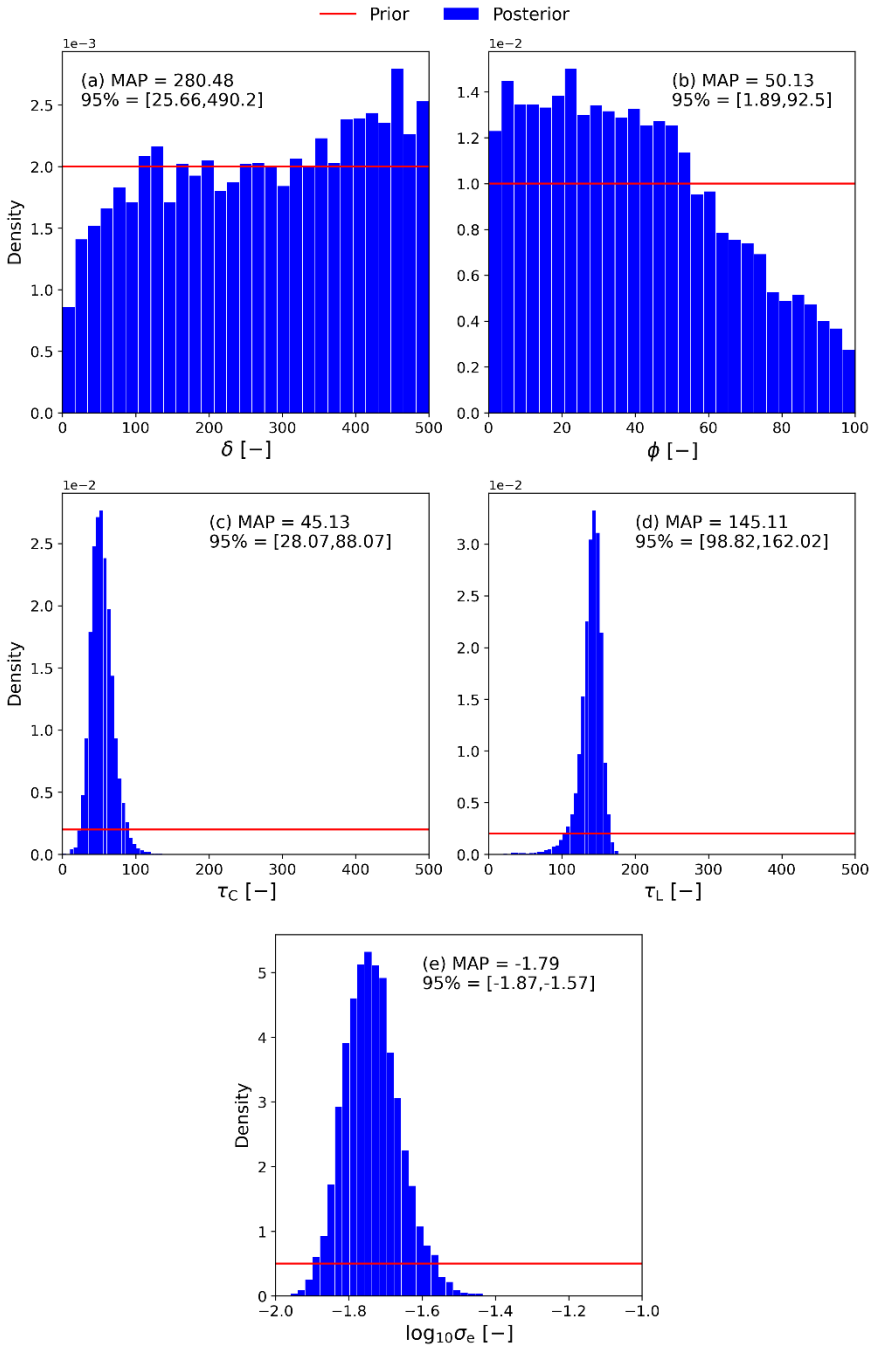

Figure 6-15: Marginal posterior distributions of the inferred ASR model parameters and standard deviation of the residual errors, derived from inversion of the sample-scale ASR measurement data.

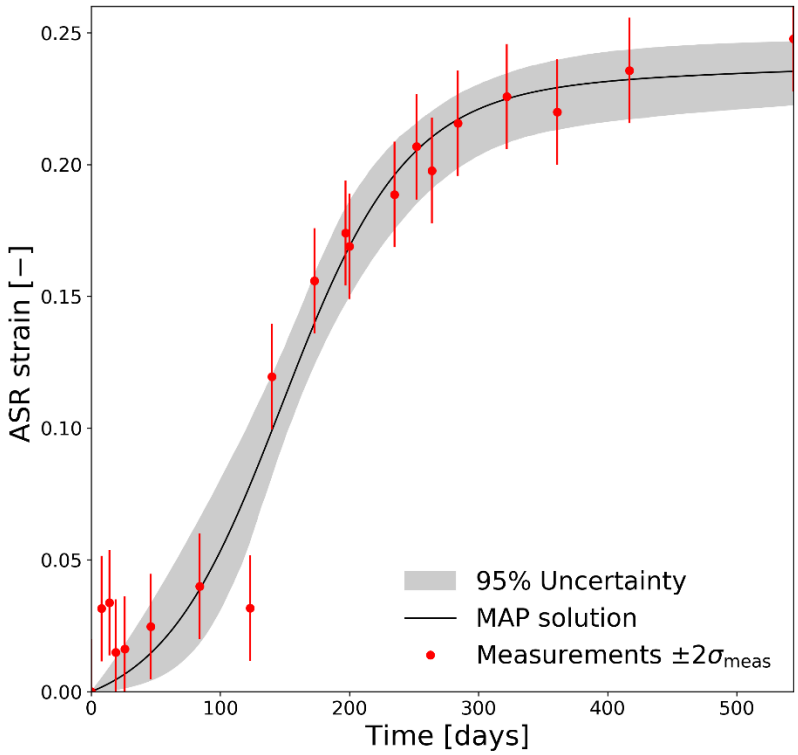

Figure 6-16: MAP predictions and 95% Posterior predictive uncertainty for the ASR model parameter inference.

6.7.4.3 Inference of the ASR model using variational Bayesian inference

The evolution of the chemical strain over the course of time is modelled through the following algebraic equation. This is a slight variant of Equation 5-5.

$$\varepsilon = \varepsilon_\infty \frac{1 - e^{-t/\tau_c}}{1 - e^{-(t-\tau_L)/\tau_c}} \tag{6-7}$$

with the model parameters τ_c and τ_L to be identified. t is time and ε is the chemical strain (expansion), which are measured in a lab-scale experiment. The goal is to infer the parameters mentioned above using the Bayes's theorem, which then enables us to predict the behaviour of ASR expansion in a probabilistic way, i.e. after obtaining posteriors of the parameters a predictive posterior for the strain can be computed. The idea is then to plug such a probabilistic model into a structural model (typically a finite element model) that is established to represent a drum-scale experiment.

In Figure 6-17, the prior/posteriors of the model parameters as well as the noise precision is depicted. Respective mean values and standard deviations are presented, as well. Note that the mean value of the inferred noise precision (1.89e4) corresponds to a standard deviation of 0.0073.

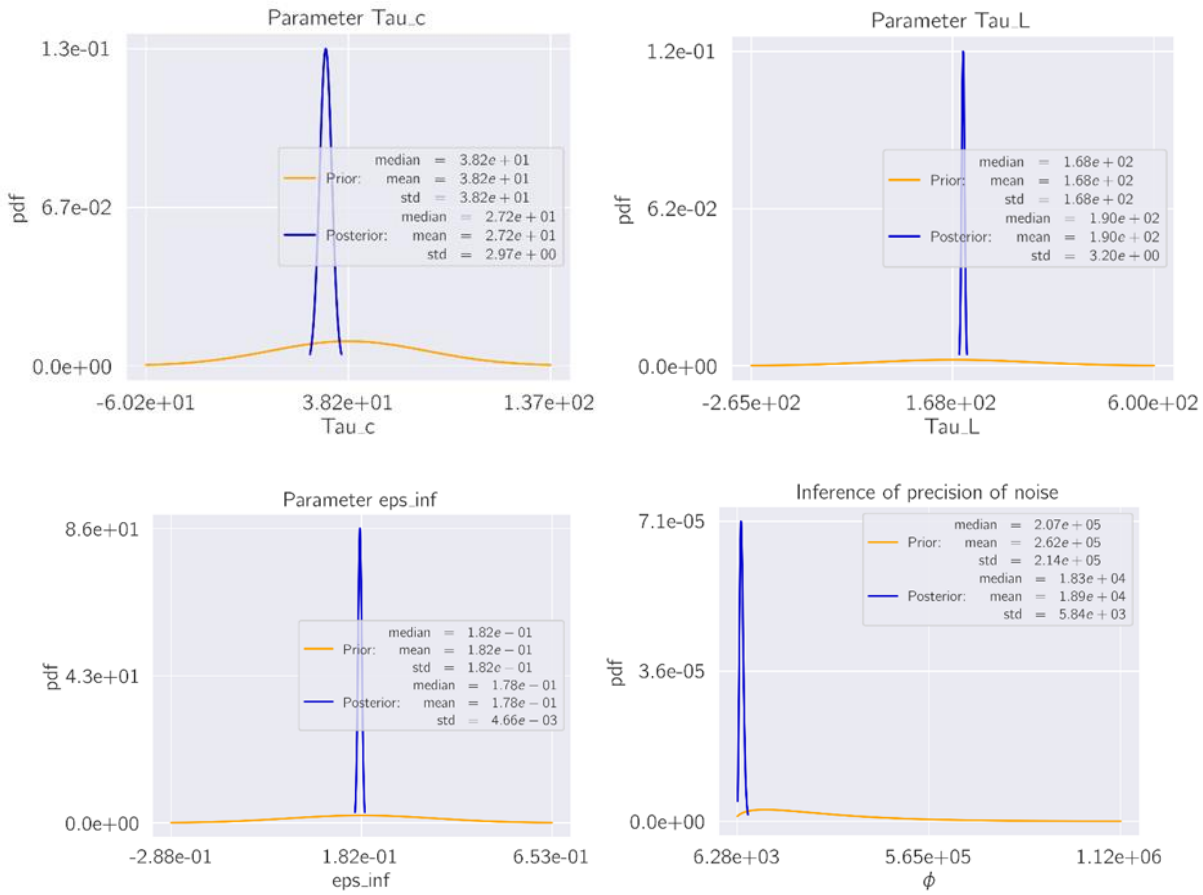

Figure 6-17 Prior/posteriors of the model parameters and the noise precision

Identifying model parameters in the form of probability distributions provides a probabilistic model, which can predict the behavior of the system in a probabilistic way. Figure 6-18 shows such a probabilistic predictive model response in comparison to the data. In addition, a deterministic identification has been performed and reported, which essentially is a least-square minimization of the model error (2) with respect to the model parameters. This is performed by means of the 'scipy.optimize' package in Python. Notice that, the identified parameters obtained from this deterministic method coincide the mean values of the posteriors from the VB.

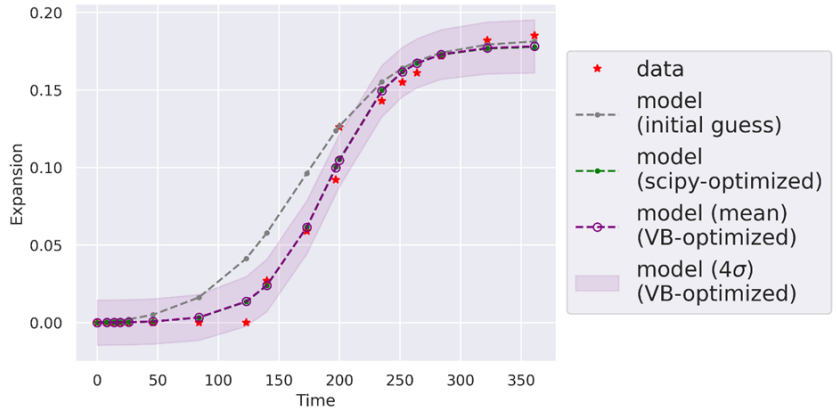

Figure 6-18 – Model response (predictive) versus data

We should recognize that a fundamental assumption of the presented Bayesian inference procedure is the additive noise model. This means, the error that we expect/formulate in the model response

does not depend on the magnitude of the model response itself. The dependency of the model error on the model response itself can be handled e.g. by a multiplicative noise model. This obviously has not been studied here, nevertheless, can be considered as a good continuation of this work for improving the accuracy and predictability of the calibrated model.

6.7.5 Summary of material parameters

Table 6-4 and

Table 6-5 provide parameters for the material models.

Table 6-4 Material parameters of RCA mortar.

Parameters	Values
Hydration parameters	
Q_∞	530 (J/g)
τ_c	0.3332 (d)
β_h	0.3189
w_c	604.6 (kg/m^3)
E_a/R	4570 (K)
Heat transfer model parameters	
ρ_b	2098.5 (kg/m^3)
C_{ps}	1100 (J/kg/K)
λ	0.6 (W/m/K) for t<0.5 (d), else 1.5 (W/m/K)
Moisture transfer model parameters	
$\frac{\partial w_e}{\partial h}$	Olsson et al. [43]
k_c	0.25 (kg/kg)
a_m	2.60E-13
b_m	9.48
D_{mth}	1.71E-07 (m^2/s)
h_{th}	0.64
v_s	4.95×10^{-2} (kg/m^3)
Linear elastic	
Young's modulus, *E*	29.6 (GPa)
Poisson's ratio, ν	0.22
Compressive strength, f_c	41 (MPa)
Tensile strength, f_t	4.1 (MPa)
Coefficient of thermal expansion, α_T	7×10^{-6} (1/K)
Autogenous shrinkage	
$\epsilon_{as\infty}$	492.37×10^{-6}
τ_{as}	35 (d)
α_{as}	0.4
β_{as}	-0.7
E_{as}/R	8937 (K)
ASR expansion parameters	
ε_∞	7.15×10^{-3}
τ_c	62.15 (d)
τ_L	127.4 (d)
ϕ	22.31
δ	167.4
m	8
β_c	2.0

Table 6-5 Steel properties.

	Values
E	193 (GPa)
ν	0.3
ρ_b	7840 (kg/m^3)
λ_T	45 (W/m/K)
C_{ps}	490 (J/kg/K)
α_T	11×10^{-7} (1/K)

6.7.6 Modelling results

The model performance is examined against the measured temperature and strains at various locations in drum 3 presented in Chapter 6.6. Figure 6-19 shows a comparison of simulated versus measured behavior of temperature. In general, the overall behavior of the model is reasonably well captured, in particular the peak temperature.

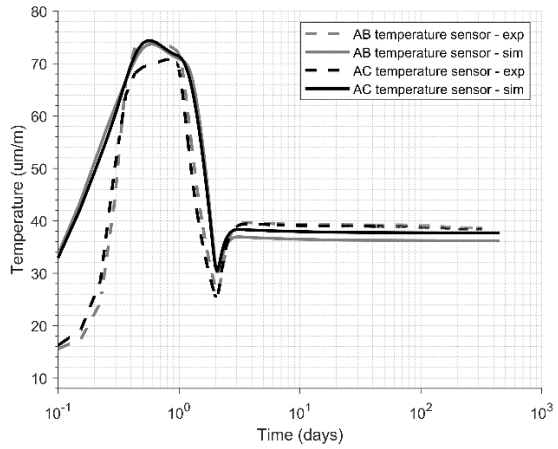

(a)

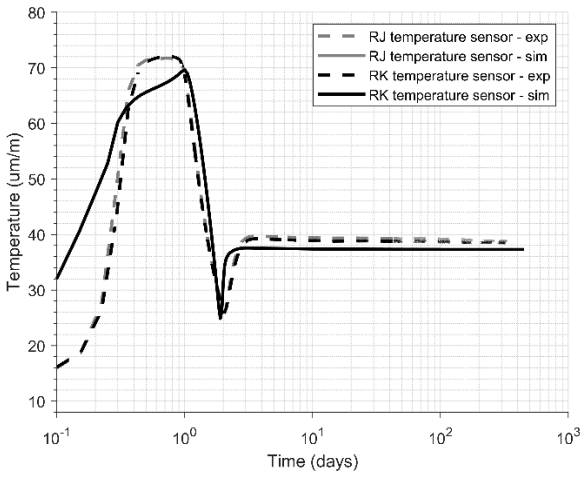

(b)

Figure 6-19 Temperature comparisons: (a) from axial strain sensors, (b) from radial strain sensors.

Figure 6-20 shows the simulated moisture evolution in terms of relative humidity. The moisture evolution from 0 to 28 days is imposed in the model based on hydration calculations. So prediction apples to > 28 days, where further consumption of water by hydration continues at all locations except at the sensor AC, which is close to the moisture boundary where the relative humidity is held constant at 1.0. It is not possible to validate the results obtained. However, it offers a qualitative understanding of evolution.

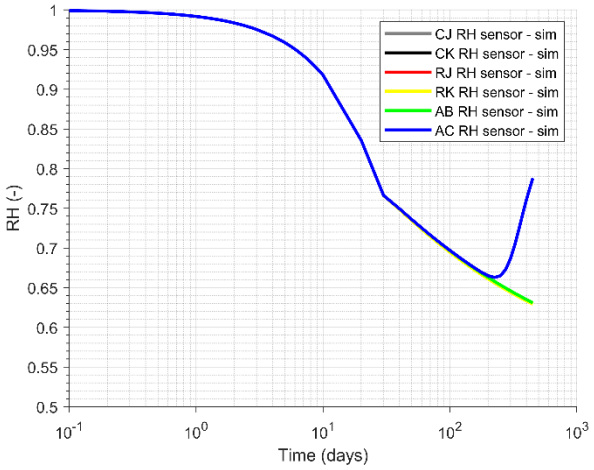

Figure 6-20 Simulated moisture evolution.

Figure 6-21 and Figure 6-22 present a comparison of simulated vs. measured strains in the axial and radial directions, respectively, at various locations in drum 3. In general, there is an overestimation of total strains in all directions during the peak of the hydration phase (t < 2 days). The mechanical behavior during this phase is difficult to capture because of the evolving system. Beyond 2 days, the comparisons are generally good, with the exception being the simulated axial strain behavior after 200 days for both AB and AC sensor locations. The simulated axial strain at AC shows a gradual shift to positive strains because of higher ASR strain kicking in. This is also the trend with AB but stabilizes after 300 days. These behaviors are consistent with the simulated relative humidity evolution at locations AB and AC (Figure 6-20) in the sense that an increase in the relative humidity results in an increase in the ASR expansion strain. Similarly, strains beyond 450 days at locations other than AB and AC shows a continued decrease (shrinkage), which are directly linked to the simulated relative humidity decrease owing to water consumption by residual hydration process and coupled with very low moisture diffusion from the top surface of the mortar. Whereas, experimentally, after 100 days, both radial and circumferential strains show a slight increase suggesting potential influence of ASR.

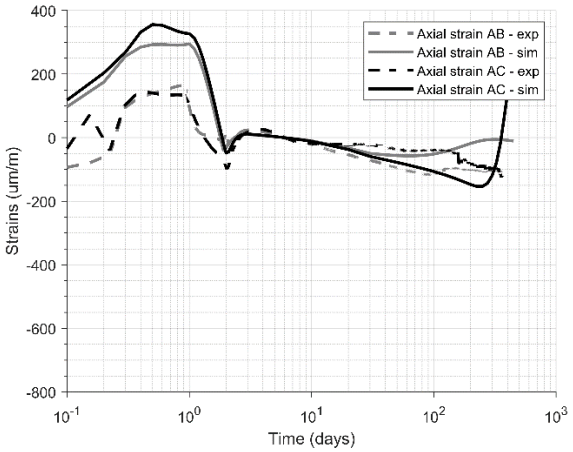

Figure 6-21 Axial strain comparison.

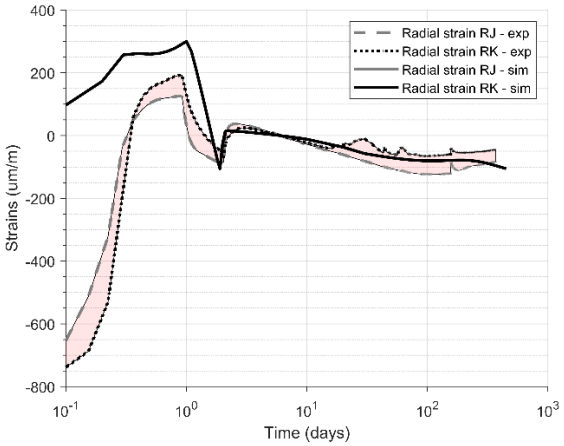

Figure 6-22 Radial strain comparison.

Given that no damage mechanics is considered in the coupled formulation, as a first approximation, the potential for damage is examined by checking if the simulated stresses in the domain exceed the tensile strength of the material. Figure 6-23 (left) confirms that axial stresses do not exceed the tensile strength anywhere in the domain. Whereas Figure 6-23 (right) shows two distinct regions where radial stresses exceed the tensile strength. However, the tensile radial stresses are mainly due to the autogenous shrinkage strain. It is thus concluded that the model do not suggest ASR related damage, at least for the simulated period.

A broader conclusion is that the adopted thermo-hydro-mechanical model does provide qualitatively good trends and forms a good candidate to develop a meta model.

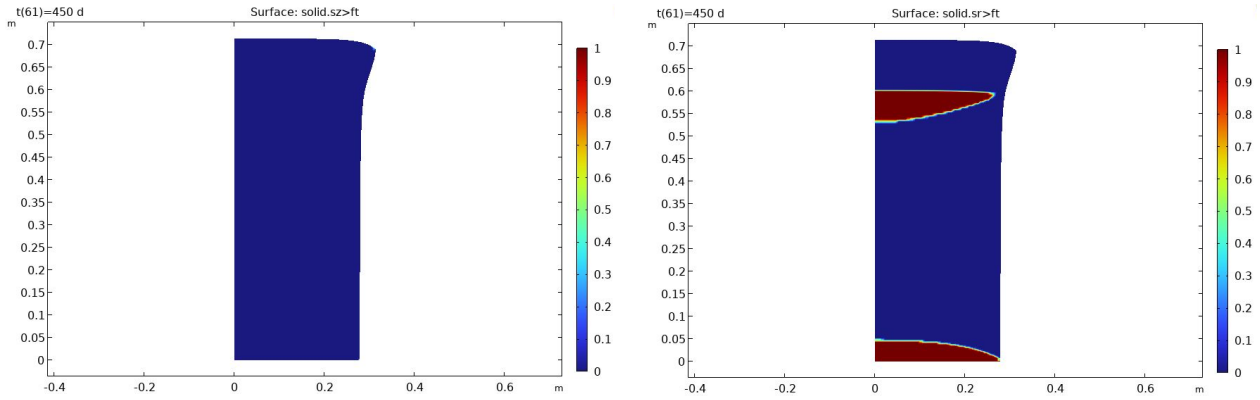

Figure 6-23 Simulated axial (left) and radial stress (right) distribution at 450 days exceeding tensile strength of the material (0 or blue: regions that do not exceed f_t; 1 or red: regions that exceed f_t).

6.8 Geochemical model for ASR

Chemical models of cementitious materials based on a thermodynamic approach can give estimations of whether e.g. alkali-silica reactions (ASR) are to be expected or not as a function of cement composition parameters.

The issue of ASR in cement-based materials has been studied for a long time. It is a deleterious reaction between the alkaline pore solution of concrete and various metastable forms of silica contained in many natural and synthetic aggregates, according to Rajabipour et al. [44]. Silica in these reactive aggregates can be dissolved in the high pH pore solution and then recombine with calcium and alkalis present in pore solution to form into silicate hydrates. These hydrates, which can be of variable stoichiometric composition, are the so-called ASR gel. This gel is typically hygroscopic in the sense that it tends to swell upon water absorption. If swelling is extensive, pores and microcracks can be filled by these gels and drive the formation of further microcracks near the gel sources and ultimately macrocracks, affecting the stability of the structural concrete.

ASR is a result of several concatenated reactions that involve (1) dissolution of metastable silica, (2) formation of nano-colloidal silica sol, (3) gelation of the sol, and (4) swelling of the gel [44]. Of these, dissolution of the silica is considered the rate limiting factor and therefore can be assumed to control the rate of ASR. Silica dissolution is faster the higher the pH and the larger the temperature, which are factors that are often considered in accelerated ASR tests. Swelling of the gel does not only depend on the chemical reactivity but also on the availability of moisture and therefore on the transport properties of concrete to allow a constant supply of moisture and reactants through its porous matrix.

Given the complexity of the coupled THCM processes at play in ASR, it is not surprising that predictive modelling of this durability issue is still a matter of intense research. Rajabipour et al. [44] reviewed the state of the art in ASR modeling and described different categories based on the method, which can be numerical or analytical (empirical models are the most widespread for engineering applications), but also analyze structural or material levels, and considering some or all of the physical processes at play.

In the past, thermodynamic modelling has been used in an attempt to predict favorable chemical conditions for ASR development in concrete. Kim and Olek (2014) [45] estimated solubilities for two hypothetical ASR products ($K_2Ca_4Si_6O_{17}\cdot 10.5H_2O$ and $Na_2Ca_4Si_6O_{17}\cdot 10.5H_2O$) and used them to predict the sequence of ASR. Guthrie and Carey (2015) [46] considered available thermodynamic data for proxy minerals of ASR products (magadiite, i.e., NaSi7O14·4.5H2O for an alkali-silicate ASR product, and okenite, i.e. $CaSi_2O_5\cdot 2H_2O$, for a high calcium silicate ASR product). In both studies, the lack of experimental solubility measurements and derived solubility products prevented

a more reliable prediction. More recently, substantial efforts have been reported for the determination of thermodynamic data for different types of ASR products. Shi and Lothenbach [47] reported thermodynamic data for K-shlykovite, Na-shlykovite and ASR-P1, or $K_{0.52}Ca_{1.16}Si_4O_8(OH)_{2.84}\cdot 1.5H_2O$). They used that data to predict the effect of Ca/Si on the formation of ASR products. They showed, using experiments and thermodynamic modelling, that a K or Na alkalis are essential to initiate ASR, within an optimum range. For low alkali concentrations, C-S-H forms instead of ASR products, while for too high concentrations, C-S-H is also formed. Only for concentrations within a certain range do ASR products form (between 0.2 and 0.5 M and with Ca/Si between 0.1 and 0.4), always in the presence of calcium [48]. These ASR products have an average atomic ratio of Ca/Si and (Na + K)/Si of 0.21–0.23 and 0.21–0.34, respectively, and this is regardless of their amorphous or crystalline nature [49]. Jin et al. (2023) [50] further studied these ASR products and estimated the temperature-dependent thermodynamic properties of Na- or K-shlykovite phases.

Despite the significant advances in the determination of solubility constants for thermodynamic modelling of ASR in cement-based materials, one of the remaining difficulties lies in the complexity of the transport of substances (alkalis, calcium, moisture, silica) within the microstructure. This makes the use of macroscopic thermodynamic models more difficult, since the limited availability of one of these ingredients due to transport restrictions between the aggregate microstructure (which is usually where cracks filled with ASR form) and the cementitious matrix.

Recently, Qiu et al. [51] developed a 3D reactive-transport lattice model of ASR in the early stage at micro-scale, with a model domain of 100 × 100 × 100 μm^3. This domain included an interface between cement paste and a reactive aggregate and considered explicitly the cement hydrated distribution in the cement paste fraction. They used a combination of thermodynamic equilibrium and kinetically controlled reactions to simulate the dissolution of silica in the aggregate, dissolution of portlandite and C-S-H in the cement paste and finally the formation of ASR products. They considered mainly K-shlykovite ($KCaSi_4O8(OH)_3 \cdot 2.9H_2O$, KSH) and tobermorite as reaction products. For K-shlykovite, the equilibrium constant was obtained through sensitivity analysis instead of the values derived in Shi and Lothenbach [48]. For the rest of reactions, they used Cemdata18. They found that the silica dissolution rate is one of the key controlling factors, as suggested before by other authors and that the three necessary conditions for ASR are extra Ca2+ buffered by CH or C-S-H in the cement paste, a high concentration of dissolved silica, and a threshold alkali concentration. They confirmed the prominent role of calcium, without which ASR would stop very soon. However, at high Ca concentrations, they reported that a ‘pozzolanic effect’ would cause that most of the dissolved silica is consumed by tobermorite formation. Even at the micro-scale, some of the key features of ASR could not be considered in Qiu et al. (2022) [51], such as the important role of microcracks within the aggregates in the formation of ASR products.

From this review, it may be concluded that reactive transport modelling or thermodynamic modelling of ASR in concrete at macroscopic scale is not yet available in the literature, not only due to the lack in thermodynamic data of all phases involved in the degradation sequence, but also due to the multi-scale nature of the process.

Despite these limitations, thermodynamic modelling of ASR can still be used to provide insight into the potential of ASR development in different cement mixes, and this will improve with more thermodynamic data becoming available in the future. Even though prediction of the progress of ASR reactions is not just dependent on chemical equilibrium conditions alone, thermodynamic modelling can still be used to give an indication of whether the ASR process is likely to occur in cement material with a certain composition.

To illustrate this, we have constructed a thermodynamic model based on recent literature on cement chemistry and ASR thermodynamic data [50-52]. This model contains the set of chemical reactions from the Cemdata18 database in combination with the Na-shlykovite and K-shlykovite thermodynamic data with adapted temperature dependency of the reaction constants as described by Jin et al. [50].

The model was set up in the ORCHESTRA framework and requires as input the bulk composition of a cementitious material in terms of total reactive amounts of CaO, SiO_2, Al_2O_3, NaO, KO, S, and C (Figure 6-24).

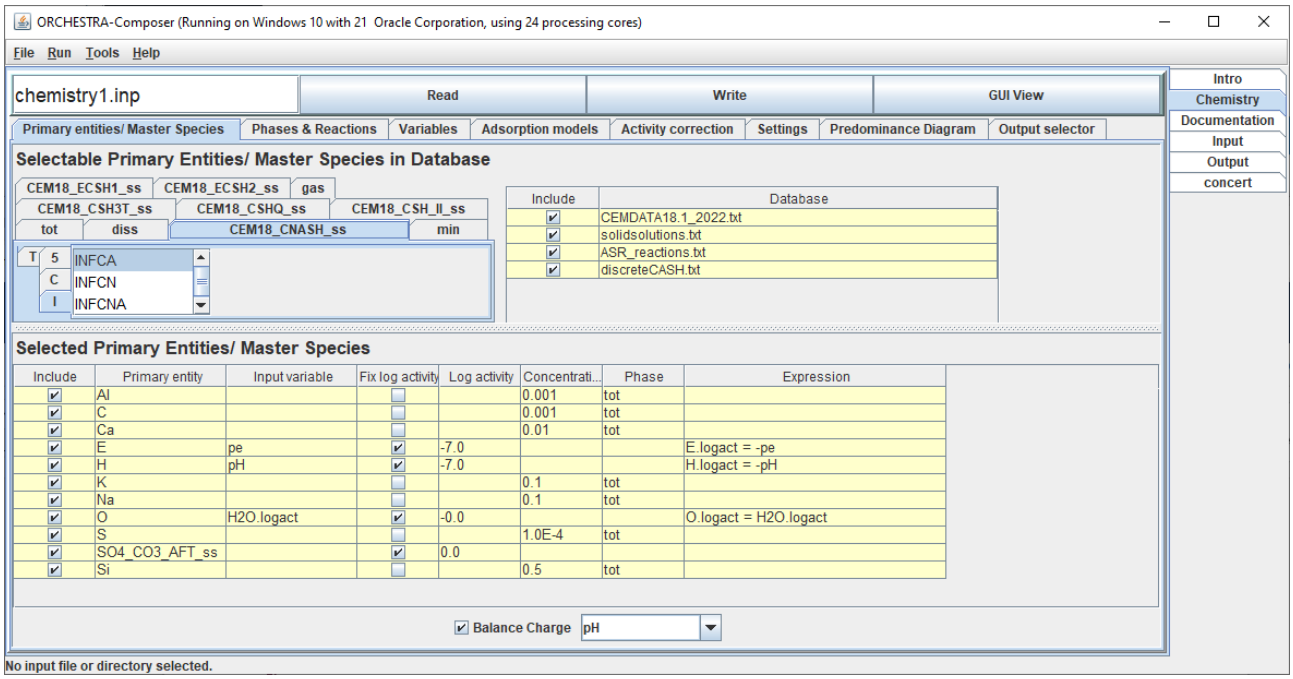

Figure 6-24 Example of selected input substances and parameters

With the input information the model calculates the distribution of elements, or master species over all possible chemical forms (e.g. aqueous species, precipitated phases, solid solutions, adsorbed species, gaseous species, etc.) under chemical equilibrium conditions. This includes the amounts of solid phases that are involved in ASR reactions. The calculated presence of such ASR phases at equilibrium, as a function of the input chemical conditions, can be used as an indicator for the possible occurrence of ASR reactions in the long term.

The figures below (Figure 6-25, Figure 6-26) show an example of model output for the calculated formation of ASR phases (indicated in light green) as a function of a range of matrix composition in terms of Ca, Si, Na, K concentrations.

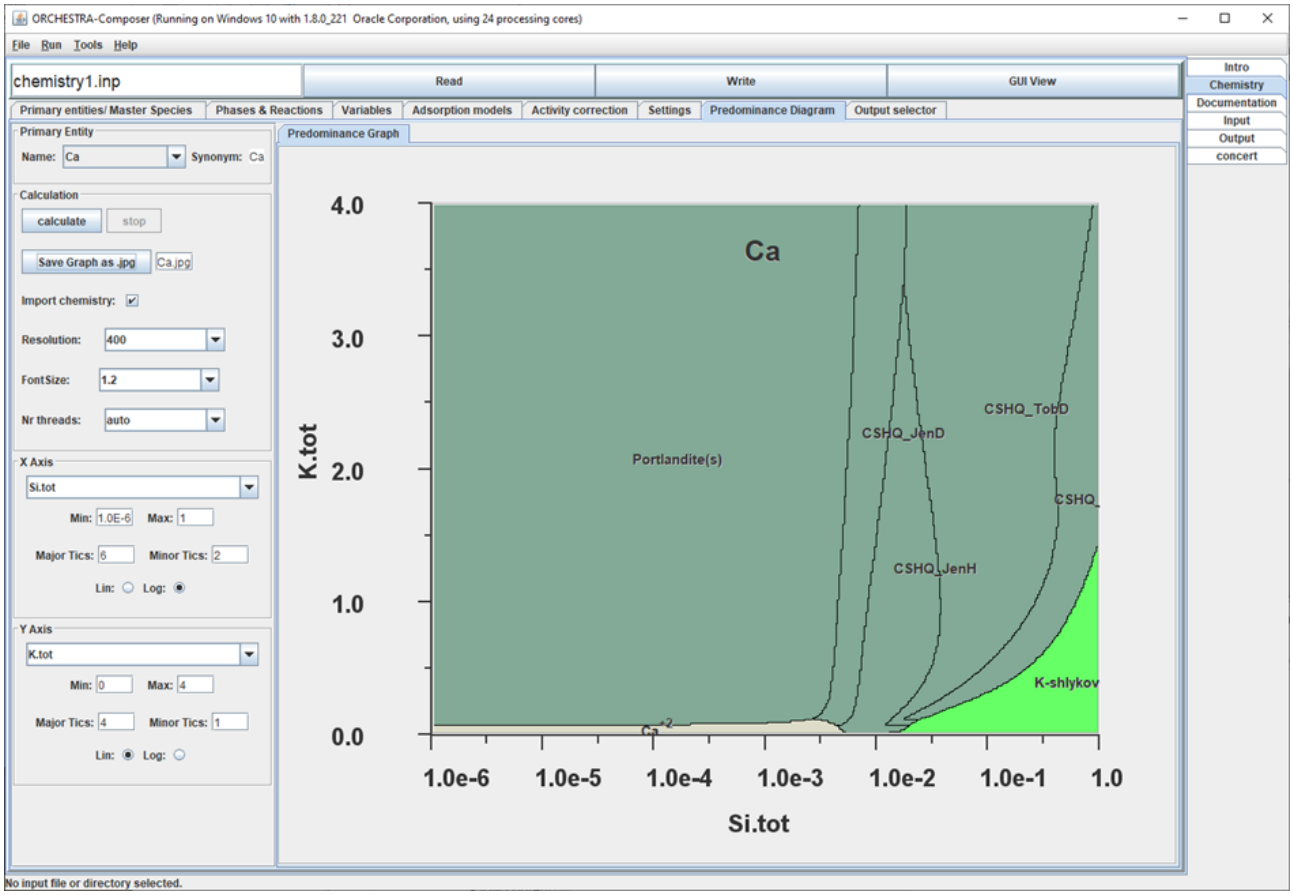

Figure 6-25 Calculated distribution of Ca over different solid phases as a function of total K and total Si present in the system. The formation of ASR phase K-shlykovite is indicated in light green.

As described above, the occurrence of the separate ASR phases does not simply increase with the amounts of K or Na present, because of competition with Na and K-containing C-S-H phases.

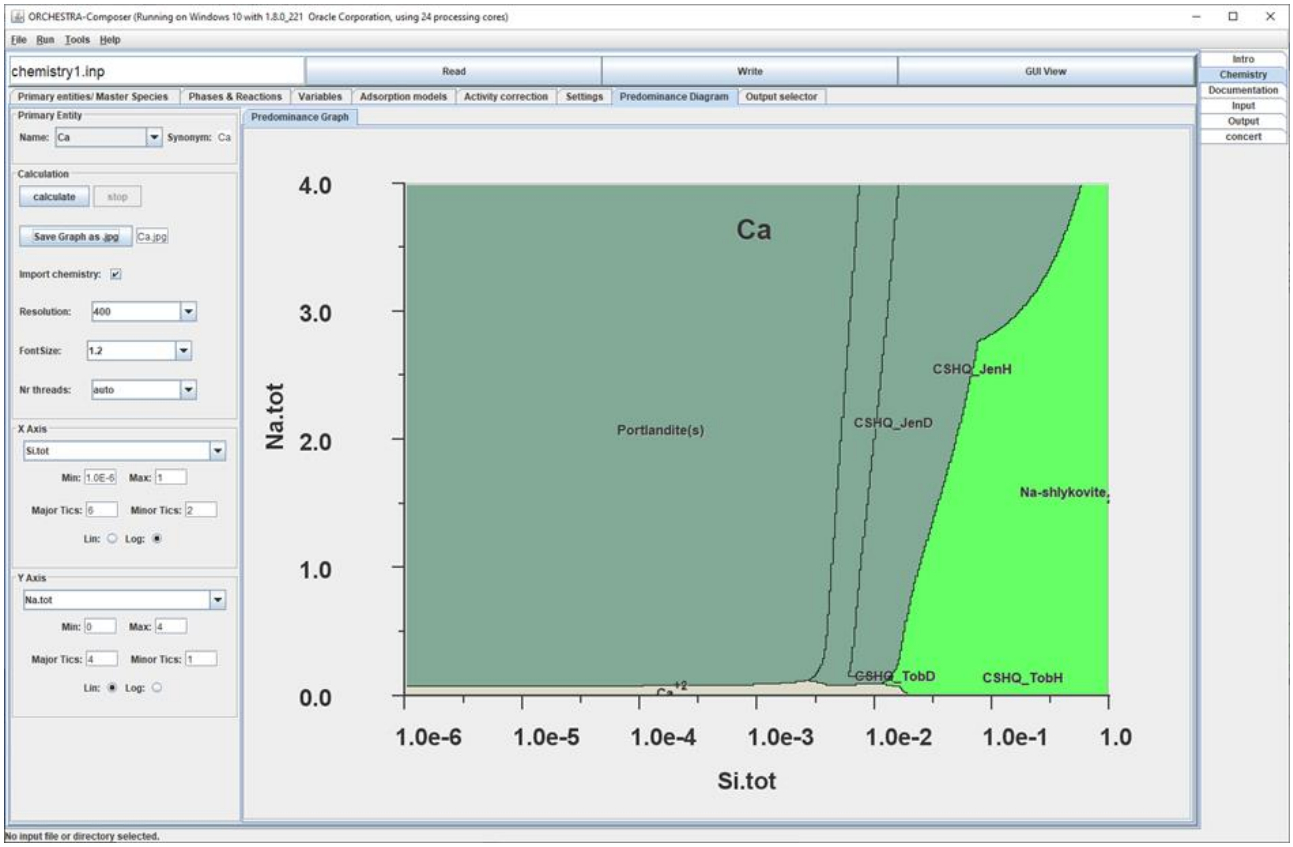

Figure 6-26 Calculated distribution of Ca over different solid phases as a function of total Na and total Si present in the system. The formation of ASR phase Na-shlykovite is indicated in light green.

The thermodynamic model can be used to predict/estimate the formation of ASR phases as a function of the bulk composition in terms of Ca, Si and alkali content of the cementitious material used in the experiments. From the results shown in Figure 6-27 follows that the stability of the ASR phases (indicated in orange) strongly depends on the ration between reactive Ca and Si in the system. For Si the reactive amount is only a small fraction of the total amount present which has to be estimated as it cannot be determined directly. The calculated results are quite sensitive for this estimation. For Ca generally the total amount present in the cement fraction is assumed to be reactive. (maximum concentration in figure n). In practice this reactivity could be less, or reduce over time by formation of calcite in contact with air.

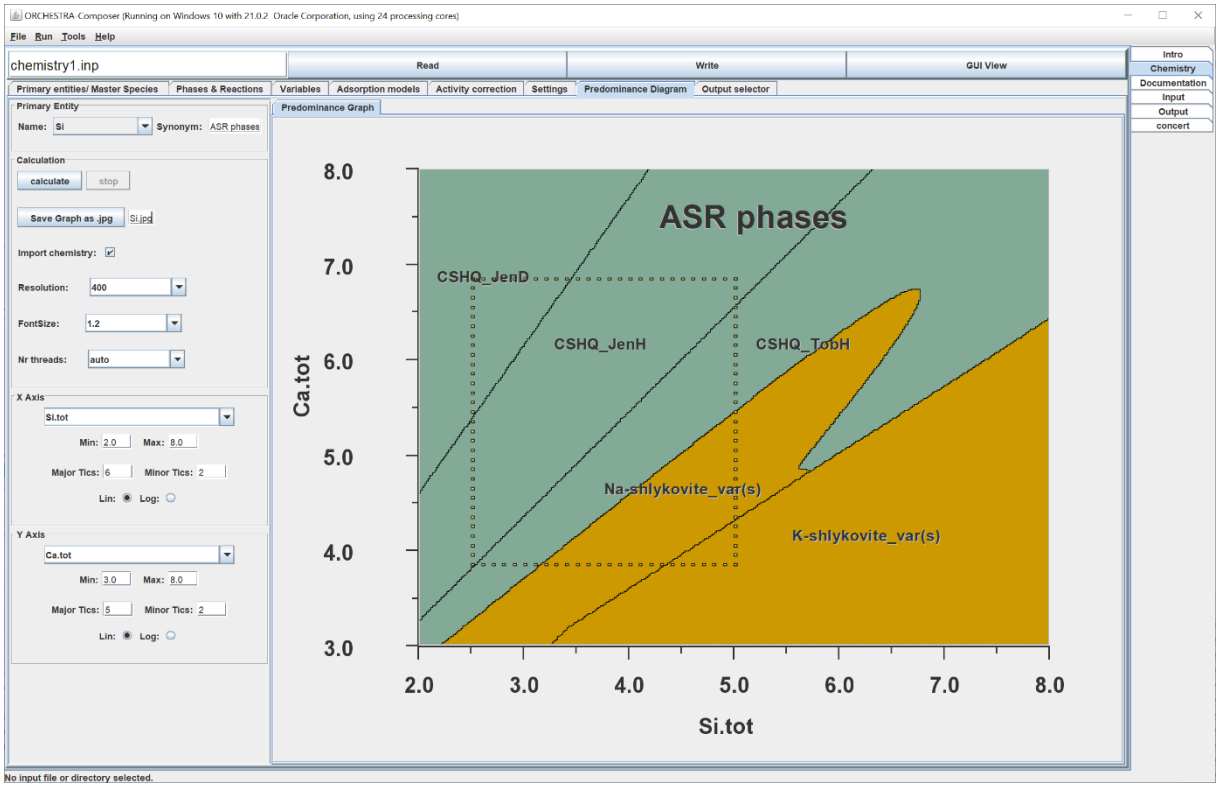

Figure 6-27 Calculated stability of ASR phases as a function of total reactive concentrations (mol/m^3) Ca and Si. Orange areas indicate conditions where ASR phases are predicted to be stable. The dashed box indicates the estimated combined ranges of reactive concentrations of Ca and Si for cement, RCA and sand fractions in the drum scale experiments.

7 Summary and challenges

7.1 Contributions

This report presents the efforts of WP 7.4 consortium towards developing a proof of concept of certain aspects of digital twin technology for the predisposal management of radioactive waste, especially for low and intermediate level waste packages. It was rather clear from the start that the exact definition of DT principally depended on project strategy and specific applications, for example, the type of waste and/or degradation mechanism. The fundamental tenet is that the DT requires a dual representation of the real world, although not mandatory that they coexist at the same time. In particular, an intelligent digital twin can provide information about the real assets from the past, identify the current state and even predict future performance.

General contributions to the PREDIS project are summarized below:

a) One possible representation of DT in the context of waste package deterioration mechanisms has been identified.
b) A proof of concept of a DT approach for the evolution of waste package is exemplified via a prototype DT dash board that runs on a *geoml* platform.
c) Implementation of two key processes viz., cement hydration and carbonation of cemented waste packages have been successfully demonstrated via a DT dashboard. In particular, the idea of *waste integrity parameter* as a measure has been proposed, which can be extended to other processes.
d) Recourse to meta models become inevitable from DT perspective. A neural network based surrogate model to address organic degradation and metallic corrosion has been presented. Training a NN model from a complex geochemical model GEM-SELEKTOR has been detailed. In particular, the power of NN model to run 1 million cases for global sensitivity analysis in under 2 seconds is highlighted.
e) A key element in any DT framework is parameter estimation technique in order to improve the overall reliability of a given model. Theoretical background on parameter estimation and recommendations for the use of Bayesian inference approach in the DT framework is discussed, with a special focus on MCMC and variational inference Bayesian techniques.

Whilst the above contributions catered to various aspects of DT work flow, a specific objective of task 7.4 was to explore a real life example of DT for waste package application. For this, ASR pathology was chosen as a candidate. The following summarizes specific conclusions related to DT for ASR pathology.

a) An integrated experimental-numerical programme for ASR pathology has been successfully implemented.
b) Experimental work covered both laboratory experiments on ASR expansion and autogenous shrinkage and four drum scale experiments on various cement recipes to simulate ASR process under both natural and accelerated conditions. Accelerated conditions were necessary in order to realize results within the time frame of PREDIS project.
c) For both the lab- and drum-scale experiments a variety of sensors were used, and interfaced through different data acquisition systems to a local server that, depending on the experiment, communicated the data to the cloud for the purpose of data storage, data analysis, dashboard and automated alerting.
d) Laboratory scale experiments clearly demonstrated that a specific cement formulation based on recycled concrete aggregate has the highest potential for forming ASR.
e) However, even after a year, the drum scale experiments for all recipes still predominantly show autogenous shrinkage. This does not imply that ASR expansion is not occurring, but this could be because of a rather slow ASR kinetics. It is postulated that RCA, which can potentially absorb water available for hydration, might have caused depletion of free water, resulting in slow ASR kinetics. The drum scale experiments are planned to continue beyond the life of PREDIS project.

f) A coupled thermo-hydro-mechanical model for ASR process based on existing approaches has been successful implemented. Though a simple high fidelity model, the number of parameters of the coupled model is significant, requiring us to focus on a very few parameters for parameter estimation using Bayesian inference.
g) The model is capable of simulating reasonable qualitative/quantitative trends for temperature and strains. Although, it is very difficult to capture the behavior accurately during the hydration phase when the cemented system is rapidly evolving. Both the drum scale experiments and associated numerical predictions are captured on PREDIS DT dashboard.
h) One forward run of the high fidelity model takes approximately 45 minutes. This however is not a problem from DT point of view because processes such as ASR are long term and computational burden will not be a limiting factor. However, currently progress is being made with the development of meta model using MCMC framework.

7.2 Challenges

Several challenges were encountered during the execution of the project: monitoring process on long time scales, transferring models from lab to waste package scale, combining different models and feedback between complex processes into a Digital Twin. More specifically,

a) Preliminary results from ASR experiments indicate that laboratory scale models are difficult to extrapolate to the drum scale – small scale experiments showed expansion of the cement matrix after a short period of time, whereas drum scale experiments showed shrinkage only so far. Such is the complexity even with a simple system such as cement mortars. Thus, the complexity to be confronted in the case of real cemented waste forms would be formidable. Furthermore, there are not well validated yet simple phenomenological models even for a single system as cement mortar with RCA. Therefore, one can expect challenges in developing models for real waste forms and then to progress into developing meta models that can be integrated into a digital twin concept.
b) Complex geochemical and mechanical processes may occur in the heterogeneous cementitious waste drums. A surrogate model based on machine-learning algorithms is developed to predict geochemical interactions in waste degradation processes over a century, simplifying full-scale geochemical models, which were used to generate learning and testing input/output samples for the ML surrogate model. The model assesses the sensitivity of reaction rates for different materials (organic materials, iron (Fe), aluminum (Al), zinc (Zn), and brass) within cementitious waste packages, taking into account several waste degradation mechanisms. Validation of complex models is difficult with such a sparse experimental database.
c) From sensor's performance point of view, there are no experimental validations to confirm that the strain measurements are reliable. For example, can the sensors lose contact with the cemented waste during shrinking or expansion process? After pouring the concrete, the sensors will remain in the same location as originally intended, even though the sensors are mounted on rigid fixtures. It is unclear yet if the sensor data is reliable under extreme conditions such as high hydration temperature and high relative humidity, typically expected under realistic conditions.
d) To validate any model, a comprehensive experimental campaign has to be undertaken with at least simulated waste form, including quantifying uncertainties. They should include enough experiments to cater to both calibration and validation.

REFERENCES

[1] Uras, S., Zovini, C., Paratore A., et al. (2021) State of the Art in packaging, storage, and monitoring of cemented wastes. PREDIS Deliverable 7.1.

[2] Parrot, L.J., Killoh, D.C. 1984. Prediction of cement hydration. British Ceramic Proceedings 35, 41–53.

[3] Kulik, D.A., Wagner, T., Dmytrieva, S.V., Kosakowski, G., Hingerl, F.F., Chudnenko, K.V., Berner, U.R. 2013. GEM-Selektor geochemical modeling package: Revised algorithm and GEMS3K numerical kernel for coupled simulation codes. Computational Geosciences 17, 1–24. https://doi.org/10.1007/s10596-012-9310-6

[4] Meeussen, J.C.L. 2003. ORCHESTRA: An Object-Oriented Framework for Implementing Chemical Equilibrium Models. Environmental Science & Technology 37 (6), 1175-1182.

[5] Laloy, E., Jacques, D. 2019. Emulation of CPU-demanding reactive transport models: a comparison of Gaussian processes, polynomial chaos expansion, and deep neural networks, Comput. Geosci. 23, 1193–1215.

[6] Lothenbach B, Scrivener K, Hooton R D, 2011. Supplementary cementitious materials. Cement and Concrete Research 41, 1244–1256.

[7] Lothenbach B, Damidot D, Matschei T, Marchand J, 2010a. Thermodynamic modelling: state of knowledge and challenges. Advances in Cement Research 22, 211–223.

[8] Damidot D, Lothenbach B, Herfort D, Glasser F P, 2011. Thermodynamics and cement science. Cement and Concrete Research 41, 679–695.

[9] Lothenbach, B., Matschei, T., Möschner, G., & Glasser, F. P. (2008). Thermodynamic modelling of the effect of temperature on the hydration and porosity of Portland cement. Cement and Concrete Research, 38(1), 1–18. https://doi.org/10.1016/j.cemconres.2007.08.017

[10] Lothenbach B, Bary B, Le Bescop P, Schmidt T, Leterrier N, 2010b. Sulfate ingress in Portland cement. Cement and Concrete Research 40, 1211–1225.

[11] Idiart A, Laviña M, Coene E, 2019. Modelling of concrete degradation – Hydro-chemo-mechanical processes. Report for the safety evaluation SE-SFL. SKB R-19-12, Svensk Kärnbränslehantering AB.

[12] Hu, G. & Pfingsten, W. (2023). Machine learning-assisted heat transport modelling for full-scale emplacement experiment at Mont Terri underground laboratory. International Journal of Heat and Mass Transfer. 213 124290.

[13] Wieland, E., Kosakowski, G., Lothenbach, B., Kulik, D.A. (2020). Geochemical modelling of the effect of waste degradation processes on the long-term performance of waste forms. Appl. Geochemistry. 115 104539.

[14] Hu, G., Miron, G.D., Pfingsten W., Dähn, R. (2024). Digital twin and surrogate model for long term geochemical processes in nuclear waste management. Proceedings of the 2024 31st International Conference on Nuclear Engineering ICONE31 August 4-8, 2024, Prague, Czech Republic.

[15] Huang, Y., Shao, H., Wieland, E., Kolditz, O., & Kosakowski, G. (2021). Two-phase transport in a cemented waste package considering spatio-temporal evolution of chemical conditions. Npj Materials Degradation, 5(1), 4.

[16] Wieland, E. (2019). Geochemical Modelling of the Temporal Evolution of L/ILW Waste Sorts with Siliceous and Calcareous Aggegates. PSI Technical Report TM-44-19-08. Paul Scherrer Institut, Villigen PSI, Switzerland.

[17] Miguel A Aguilo, Laura P Swiler, and Angel Urbina. “An overview of inverse material identification within the frameworks of deterministic and stochastic parameter estimation”. In: International Journal for Uncertainty Quantification 3.4 (2013).

[18] Emilio Turco. “Tools for the numerical solution of inverse problems in structural mechanics: review and research perspectives”. In: European Journal of Environmental and Civil Engineering 21.5 (2017), pp. 509–554.

[19] Smith, T., Marshall, L., Sharma, A. (2015). Modeling residual hydrologic errors with Bayesian inference. J. Hydrol, 528, 29–37.

[20] Gelman, A., Carlin J.B., Stern H.S., Dunson, D.B., Vehtari, A., Rubin, D.B. (2013). Bayesian Data Analysis, Third Edition. Chapman & Hall/CRC Texts in Statistical Science.

[21] Hoffman, M. D., & Gelman, A. (2014). The No-U-Turn sampler: Adaptively setting path lengths in Hamiltonian Monte Carlo. Journal of Machine Learning Research, 15(1), 1593–1623.

[22] Bingham, E., Chen, J. P., Jankowiak, M., Obermeyer, F., Pradhan, N., Karaletsos, T., Singh, R., Szerlip, P., Horsfall, P., and Goodman, N.D. (2019). Pyro: Deep universal probabilistic programming,” The Journal of Machine Learning Research, vol. 20, no. 1, pp. 973–978.

[23] Vrugt, J. A., ter Braak, C., Diks, C., Robinson, B. A., Hyman, J. M., & Higdon, D. (2009). Accelerating Markov chain Monte Carlo simulation by differential evolution with self-adaptive randomized subspace sampling. International Journal of Nonlinear Sciences and Numerical Simulation, 10(3), 273–290.

[24] Laloy, E., & Vrugt, J. A. (2012). High-dimensional posterior exploration of hydrologic models using multiple-try DREAMzs and high performance computing. Water Resources Research, 48, W01526. https://doi.org/10.1029/2011WR010608

[25] Laloy, E., Rogiers, B., Vrugt, J. A., Mallants, D., & Jacques, D. (2013). Efficient posterior exploration of a high-dimensional groundwater model from two-stage Markov Chain Monte Carlo simulation and polynomial chaos expansion. Water Resources Research, 49, 2664–2682. https://doi.org/10.1002/wrcr.20226

[26] Laloy, E., Linde, N., Jacques, D., & Vrugt, J. A. (2015). Probabilistic inference of multi-Gaussian fields from indirect hydrological data using circulant embedding and dimensionality reduction. Water Resources Research, 51, 4224–4243. https://doi.org/10.1002/2014WR016395

[27] Laloy, E., Linde, N., & Vrugt, J. A. (2012). Mass conservative three-dimensional water tracer distribution from Markov chain Monte Carlo inversion of time-lapse ground-penetrating radar data. Water Resources Research, 48, W07510. https://doi.org/10.1029/2011WR011238

[28] Hunziker, J., Laloy, E., & Linde, N. (2017). Inference of multi-Gaussian relative permittivity fields by probabilistic inversion of crosshole ground-penetrating radar data. Geophysics, 82(5), H25–H40. https://doi.org/10.1190/geo2016-0347.1.

[29] Hunziker, J., Laloy, E., & Linde, N. (2019). Bayesian full-waveform tomography with application to crosshole ground penetrating radar data. Geophysical Journal International, 218(2), 913–931.

[30] Gelman A., Vehtari A., Simpson D., Margossian C.C., Carpenter B., Yao Y., Kennedy L., Gabry J., Bürkner P-C., Modrák M. (2020). Bayesian Workflow, v1 arXiv:2011.01808

[31] Rue, H., Martino, S., and Chopin, N. (2009). Approximate Bayesian inference for latent Gaussianmodels using integrated nested Laplace approximations (with discussion). Journal of the Royal Statistical Society, Series B, 71(2):319–392.

[32] Salimans, T., Kingma, D., Welling, M. Markov chain monte carlo and variational inference: Bridging the gap, in: International Conference on Machine Learning, 2015, pp. 1218–1226.

[33] Marc C Kennedy and Anthony O’Hagan. “Bayesian calibration of computer models”. In: Journal of the Royal Statistical Society: Series B (Statistical Methodology) 63.3 (2001), pp. 425–464.

[34] Michael A. Chappell et al. “Variational Bayesian inference for a nonlinear forward model”. In: IEEE Trans-974 actions on Signal Processing 57 (1 2009). issn: 1053587X. doi: 10.1109/TSP.2008.2005752.

[35] ASTM C. Standard test method for potential alkali reactivity of aggregates (mortar-bar method). 2007.

[36] Ekolu S, Rakgosi G, Hooton D. Long-term mitigating effect of lithium nitrate on delayed ettringite formation and ASR in concrete – Microscopic analysis. Materials Characterization. 2017;133:165-75.

[37] Venkatanarayanan HK, Rangaraju PR. Effectiveness of Lithium Nitrate in Mitigating Alkali-Silica Reaction in the Presence of Fly Ashes of Varying Chemical Compositions. J Mater Civil Eng. 2014;26(7).

[38] ASTM. Standard test method for determination of length change of concrete due to alkali-silica reaction. ASTM International; 2008.

[39] Seignol J-F, Baghdadi N, Toutlemonde F. A macroscopic chemo-mechanical model aimed at re-assessment of delayed ettringite formation affected concrete structures. 1st international conference on computational technologies in concrete structures CTCS2009.

[40] Hubler MH, Wendner R, Bažant ZP. Statistical justification of Model B4 for drying and autogenous shrinkage of concrete and comparisons to other models. Mater Struct. 2015;48:797-814.

[41] Nilsson L-O. HYGROSCOPIC MOISTURE INCONCRETE-DRYING, MEASUREMENTS &. RELATED MATERIAL PROPERTIES. 1980.

[42] Phung QT, Ferreira E, Seetharam S, Nguyen VT, Govaerts J, Valcke E. Understanding hydration heat of mortars containing supplementary cementitious materials with potential to immobilize heavy metal containing waste. Cement and Concrete Composites. 2021;115:103859.

[43] N. Olsson, L.-O. Nilsson, M. Åhs, V. Baroghel-Bouny, Moisture transport and sorption in cement based materials containing slag or silica fume, Cement and Concrete Research 106 (2018) 23-32.

[44] F. Rajabipour, E. Giannini, C. F. Dunant, J. H. Ideker, and M. D. A. Thomas. Alkali-silica reaction: Current understanding of the reaction mechanisms and the knowledge gaps. Cement and Concrete Research, 76:130–146, 2015.

[45] T. Kim, J. Olek, Chemical sequence and kinetics of alkali–silica reaction part II. A thermodynamic model, J. Am. Ceram. Soc. 97 (2014) 2204–2212.

[46] G.D. Guthrie, J.W. Carey, A thermodynamic and kinetic model for paste–aggregate interactions and the alkali–silica reaction, Cem. Concr. Res. 76 (2015) 107–120.

[47] Shi, Z., Lothenbach, B., 2019. The role of calcium on the formation of alkali-silica reaction products. Cement and Concrete Research 126, 105898.

[48] Shi, Z., Lothenbach, B., 2020. The combined effect of potassium, sodium and calcium on the formation of alkali-silica reaction products. Cement and Concrete Research 127, 105914.

[49] A. Leemann, Z. Shi, J. Lindgård, Characterization of amorphous and crystalline ASR products formed in concrete aggregates, Cem. Concr. Res. 137 (2020), 106190, https://doi.org/10.1016/j.cemconres.2020.106190.

[50] Jin, H., Ghazizadeh, S., Provis, J.L., 2023. Assessment of the thermodynamics of Na,K-shlykovite as potential alkali-silica reaction products in the (Na,K)2O-CaO–SiO2-H2O system. Cement and Concrete Research 172 (2023) 107253.

[51] Qiu, X., Chen, J. Ye, G., De Schutter, G. 2022. Insights in the chemical fundamentals of ASR and the role of calcium in the early stage based on a 3D reactive transport model. Cement and Concrete Research 157, 106778

[52] B. Lothenbach, D.A. Kulik, T. Matschei, M. Balonis, L. Baquerizo, B. Dilnesa, G. D. Miron, R.J. Myers, Cemdata18: a chemical thermodynamic database for hydrated Portland cements and alkali-activated materials, Cem. Concr. Res. 115 (2019) 472–506.